UDK 621.3:(53+54+621+66)(05)(497.1)=00 ISSN 0352-9045

INFORMACIJE MIDEM 2·2007

Strokovno društvo za mikroelektroniko elektronske sestavne dele in materiale

Strokovna revija za mikroelektroniko, elektronske sestavne dele in materiale
Journal of Microelectronics, Electronic Components and Materials

INFORMACIJE MIDEM, LETNIK 37, ŠT. 2(122), LJUBLJANA, junij 2007

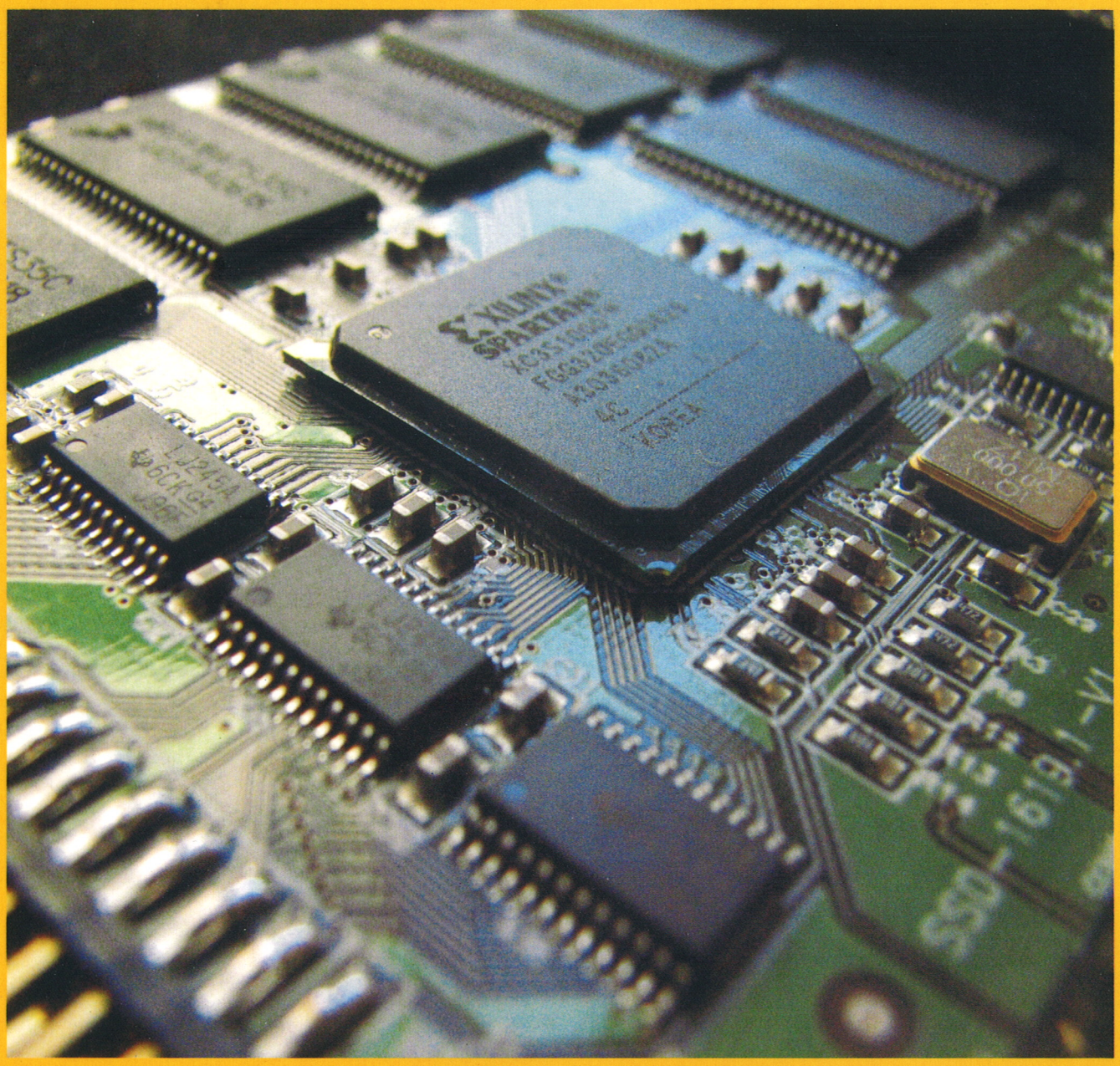

UDK 621.3:(53+54+621+66)(05)(497.1)=00 ISSN 0352-9045

INFORMACIJE MIDEM 2 ○ 2007

INFORMACIJE MIDEM LETNIK 37, ŠT. 2(122), LJUBLJANA, JUNIJ 2007
INFORMACIJE MIDEM VOLUME 37, NO. 2(122), LJUBLJANA, JUNE 2007

Revija izhaja trimesečno (marec, junij, september, december). Izdaja strokovno društvo za mikroelektroniko, elektronske sestavne dele in materiale - MIDEM.
Published quarterly (march, june, september, december) by Society for Microelectronics, Electronic Components and Materials - MIDEM.

Naslov uredništva
Headquarters
Uredništvo Informacije MIDEM
MIDEM pri MIKROIKS
Stegne 11, 1521 Ljubljana, Slovenija
tel.: + 386 (0)1 51 33 768
faks: + 386 (0)1 51 33 771
e-pošta: Iztok.Sorli@guest.arnes.si
http://www.midem-drustvo.si/

Letna naročnina je 100 EUR, cena posamezne številke pa 25 EUR. Člani in sponzorji MIDEM prejemajo Informacije MIDEM brezplačno.
Annual subscription rate is EUR 100, separate issue is EUR 25. MIDEM members and Society sponsors receive Informacije MIDEM for free.

Znanstveni svet za tehnične vede je podal pozitivno mnenje o reviji kot znanstveno-strokovni reviji za mikroelektroniko, elektronske sestavne dele in materiale. Izdajo revije sofinancirajo ARRS in sponzorji društva.
Scientific Council for Technical Sciences of Slovene Research Agency has recognized Informacije MIDEM as scientific Journal for microelectronics, electronic components and materials.
Publishing of the Journal is financed by Slovene Research Agency and by Society sponsors.

Znanstveno-strokovne prispevke objavljene v Informacijah MIDEM zajemamo v podatkovne baze COBISS in INSPEC.

Prispevke iz revije zajema ISI® v naslednje svoje produkte: Sci Search®, Research Alert® in Materials Science Citation Index™

Scientific and professional papers published in Informacije MIDEM are assessed into COBISS and INSPEC databases.

The Journal is indexed by ISI® for Sci Search®, Research Alert® and Material Science Citation Index™

Po mnenju Ministrstva za informiranje št.23/300-92 šteje glasilo Informacije MIDEM med proizvode informativnega značaja.

Grafična priprava in tisk
Printed by
BIRO M, Ljubljana

Naklada
Circulation
1000 izvodov
1000 issues

Poštnina plačana pri pošti 1102 Ljubljana
Slovenia Taxe Percue

UDK621.3:(53+54+621+66), ISSN0352-9045 Informacije MIDEM 37(2007)2, Ljubljana

VSEBINA CONTENT

Obnovitev članstva v strokovnem društvu MIDEM in iz tega izhajajoče ugodnosti in obveznosti

Spoštovani,

V svojem več desetletij dolgem obstoju in delovanju smo si prizadevali narediti društvo privlačno in koristno vsem članom.Z delovanjem društva ste se srečali tudi vi in se odločili, da se v društvo včlanite. Življenske poti, zaposlitev in strokovno zanimanje pa se z leti spreminjajo, najrazličnejši dogodki, izzivi in odločitve so vas morda usmerili v povsem druga področja in vaš interes za delovanje ali članstvo v društvu se je z leti močno spremenil, morda izginil. Morda pa vas aktivnosti društva kljub temu še vedno zanimajo, če ne drugače, kot spomin na prijetne čase, ki smo jih skupaj preživeli. Spremenili so se tudi naslovi in način komuniciranja.

Ker je seznam članstva postal dolg, očitno pa je, da mnogi nekdanji člani nimajo več interesa za sodelovanje v društvu, se je Izvršilni odbor društva odločil, da stanje članstva uredi in **vas zato prosi, da izpolnite in nam pošljete obrazec priložen na koncu revije.**

Naj vas ponovno spomnimo na ugodnosti, ki izhajajo iz vašega članstva. Kot član strokovnega društva prejemate revijo »Informacije MIDEM«, povabljeni ste na strokovne konference, kjer lahko predstavite svoje raziskovalne in razvojne dosežke ali srečate stare znance in nove, povabljene predavatelje s področja, ki vas zanima. O svojih dosežkih in problemih lahko poročate v strokovni reviji, ki ima ugleden IMPACT faktor. S svojimi predlogi lahko usmerjate delovanje društva.

Vaša obveza je plačilo članarine 25 EUR na leto. Članarino lahko plačate na transakcijski račun društva pri A-banki: 051008010631192. Pri nakazilu ne pozabite navesti svojega imena!

Upamo, da vas delovanje društva še vedno zanima in da boste članstvo obnovili. Žal pa bomo morali dosedanje člane, ki članstva ne boste obnovili do konca leta 2007, brisati iz seznama članstva.

Prijavnice pošljite na naslov:

MIDEM pri MIKROIKS

Stegne 11

1521 Ljubljana

Ljubljana, junij 2007

Izvršilni odbor društva

SPICE-aided Modelling of SiC MESFETs

Janusz Zarębski, Damian Bisewski

Gdynia Maritime University, Department of Marine Electronics, Poland

Key words: SiC MESFETs, modelling, SPICE.

Abstract: In the paper the d.c. characteristics of the SiC MESFET operating in the wide temperature range are investigated. The transistor CRF24010 offered by Cree Inc. is considered. The characteristics obtained from measurements and SPICE simulations performed with the use of Raytheon-Statz model are compared.

Modeliranje SiC MESFET transistorjev s programom SPICE

Kjučne besede: SiC MESFET tranzistorji, modeliranje, SPICE

Izvleček: V prispevku raziščemo d.c. karakteristike SiC MESFET tranzistorja v širokem območju temperatur. Merili smo tranzistor CRF 24010 firme Cree Inc. in primerjali izmerjene vrednosti s tistimi, ki smo jih dobili s simulacijami s programom SPICE in Raytheon-Statz modelom.

1. Introduction

MESFETs are very popular high frequency devices (RF transistors) which have found applications in radiocommunication circuits, as: amplifiers, mixers, oscillators, etc. Commonly used MESFETs made of gallium arsenide (GaAs) are known since 1968. In 1998 the first MESFET made of silicon carbide (SiC MESFET) was worked out in Cree Labs., whereas since 2002 such devices have been commercially available /1/.

Computer-aided design of the circuits mentioned above, requires the credible, experimentally verified models of the considered devices, acceptable by proper computer tools, as e.g. SPICE /2/. The built-in SPICE models of a MESFET have been worked out for GaAs devices.

In the paper the usefulness of the built-in Raytheon-Statz model for describing SiC MESFETs is investigated. The estimation of accuracy of this model is performed by the comparison of the measured and simulated device characteristics. The transistor CRF24010 offered by Cree Inc. /3/ was chosen for investigations. In the Raytheon-Statz based simulations the values of the model parameters were obtained from measurements.

2. The Raytheon-Statz model

The network form of the Raytheon-Statz model is presented in Fig. 1 /2/.

The main device current i_D is of the form /2/:

- in the cut-off region (u_{GS}-VTO<0):

$$\mathrm{Idrain} = 0 \tag{1}$$

- in the linear and the saturation regions (u_{GS}-VTO≥0):

$$\mathrm{Idrain} = \mathrm{BETA} \cdot \left(1 + \mathrm{LAMBDA} \cdot u_{DS}\right) \cdot \mathrm{A} \tag{2}$$

where: u_{GS} - the gate-source voltage, u_{DS} - the drain-source voltage, VTO - the pinchoff voltage, BETA - the transconductance coefficient, LAMBDA - the channel-length modulation coefficient, whereas the parameter A is given by /2/:

$$\mathrm{A} = \left(u_{GS} - \mathrm{VTO}\right)^2 \cdot \frac{K_t}{1 + \mathrm{B} \cdot \left(u_{GS} - \mathrm{VTO}\right)} \tag{3}$$

where: B - the doping tail extending parameter. In turn, the parameter K_t is given by the formula /2/:

- in the linear region:

$$0 < u_{DS} < \frac{3}{\mathrm{ALPHA}} \tag{4}$$

$$K_t = 1 - \left(1 - u_{DS} \cdot \frac{\mathrm{ALPHA}}{3}\right)^3 \tag{5}$$

- in the saturation region:

$$u_{DS} \geq \frac{3}{\mathrm{ALPHA}} \tag{6}$$

$$K_t = 1 \tag{7}$$

where: *ALPHA* - the saturation voltage parameter.

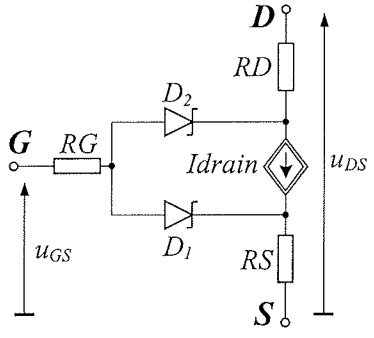

Fig. 1. The network form of the Raytheon-Statz model

The currents of the Schottky diodes (D_1 and D_2 in Fig. 1) are described by the ideal components only, expressed as follows /2/:

$$i_{GS} = IS \cdot \left[\exp\left(\frac{u_{GS}}{N \cdot Vt} \right) - 1 \right] \quad (8)$$

$$i_{GD} = IS \cdot \left[\exp\left(\frac{u_{GD}}{N \cdot Vt} \right) - 1 \right] \quad (9)$$

where: IS - the saturation current, N - the emission coefficient, Vt - the thermal potential.

In the model, the parameters: BETA, IS and VTO are dependent on the temperature T. The thermal dependence of BETA(T) and VTO(T) are given by /2/:

$$BETA(T) = BETA \cdot 1{,}01^{BETATCE \cdot (T - Tnom)} \quad (10)$$

$$VTO(T) = VTO + VTOTC \cdot (T - Tnom) \quad (11)$$

where: Tnom - the nominal temperature, VTOTC - the pinchoff voltage temperature coefficient, BETATCE - the transconductance exponential coefficient.

The thermal dependence of the saturation current IS(T) is given by /2/:

$$IS(T) = IS \cdot \exp\left[\frac{\left(\frac{T}{TNOM} - 1 \right) \cdot EG(T)}{N \cdot Vt} \right] \cdot \left(\frac{T}{TNOM} \right)^{\frac{XTI}{N}} \quad (12)$$

where: XTI - the temperature exponent. The temperature dependence of the band-gap voltage (barrier height) is written in the formula /2/:

$$EG(T) = 1{,}16 - \frac{0{,}000702 \cdot T^2}{T + 1108} \quad (13)$$

As it is seen, in the model under consideration, the temperature dependence of the band-gap energy Eq (13) is given just for the silicon (Si), therefore in the case of modelling transistors made of other semiconductors, e.g. gallium arsenide (GaAs), silicon carbide (SiC), Eq (13) is inaccurate.

3. The investigation results

To verify the Raytheon-Statz model, the current-voltage characteristics of CRF24010-101 SiC transistor in the wide temperature range were measured. The catalog admissible values of the parameters of the investigated device are given in Table 1 /3/.

TABLE 1. The catalog parameter values of CRF24010-101 transistor

Parameter	Catalog value
$U_{DS\ max}$	120 VDC
$U_{GS\ max}$	-20, +3 VDC
P_{max}	10W
f_{max}	2,7 GHz
$T_{j\ max}$	250 °C

The measured and simulated characteristics are shown in Figs. 2 - 7, where the points joined by the broken lines and the solid lines denote the measured and calculated results, respectively. The values of the model parameters are given in Table 2.

TABLE 2. The Raytheon-Statz model parameter values of CRF24010-101 transistor

Parameter	Value
VTO	-9,42 V
BETA	0,0136 A/V^2
LAMBDA	6,53 V^{-1}
ALPHA	0,136 V^{-1}
B	0,034 V^{-1}
VTOTC	-1,16mV/ °C
BETATCE	0,02 %/ °C
IS	7E-14 A
N	1,25

In Fig. 2 and 3 the transfer characteristics at U_{DS}=5V in the temperature range 295÷433K (Fig. 2) as well as at T=295K for two values of the drain-source voltage (Fig. 3) are presented. As seen, the value of the threshold voltage decreases with the increase of the temperature and the drain-source voltage. For u_{GS}<VTO the main current of the MESFET is of a relatively high value due to the current flowing through the Schottky diodes.

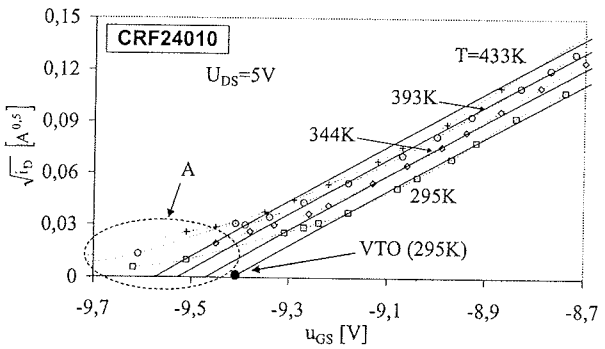

Fig. 2. The transfer characteristics at U_{DS}=5V

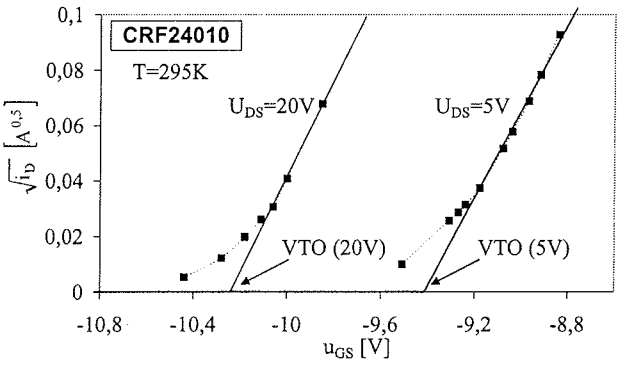

Fig. 3. The transfer characteristics at T=295K

The temperature dependence of the threshold voltage $V_{TO}(T)$ at two values of the drain-source voltage is presented in Fig. 4. As seen, these characteristics are quasi-linear and the temperature coefficients of changing V_{TO} are: VTOTC=-1,16mV/K at U_{DS}=5V and VTOTC=-0,68mV/K at U_{DS}=20V.

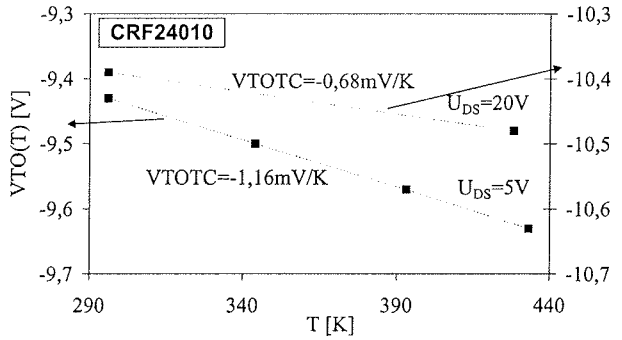

Fig. 4. The temperature dependence of the threshold voltage VTO(T)

In Fig. 5 the output characteristics in the range of the drain-source voltage up to 45V at the ambient temperature T=295K for two gate-source voltage values U_{GS}: -9V and -11V are shown. It is visible, that the acceptable agreement between simulation and measured results is observed at U_{GS}=-9V only. The value of the drain current corresponding to the characteristic measured at U_{GS}=-11V increases strongly, what probably results from influence of the drain-source voltage on the transistor threshold voltage (see Fig. 3).

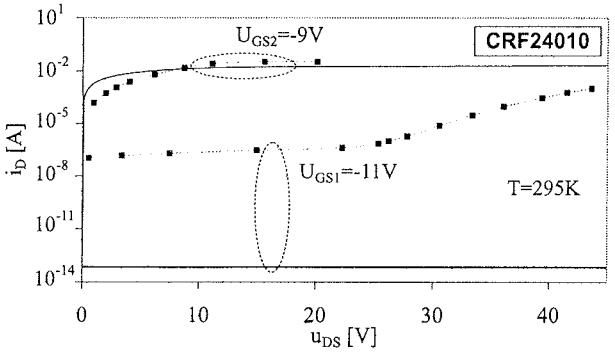

Fig. 5. The output characteristics at U_{GS}: -9V and -11V

In turn, in Fig. 6 the qualitative discrepancy between measurements and simulations in the avalanche range of the investigated device are observed. It should be noted, that at the point B (U_{DS}=110V) the transistor was damaged, in spite of that its operation point was inside SOA.

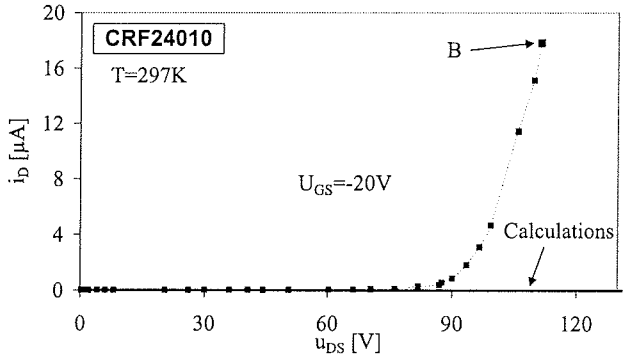

Fig. 6. The output characteristics at T=297K

In Fig. 7 the current-voltage characteristics of the Schottky diode (D_1) operating at the forward bias (Fig. 7a) and at the reverse bias (Fig. 7b), corresponding to five temperature values are presented.

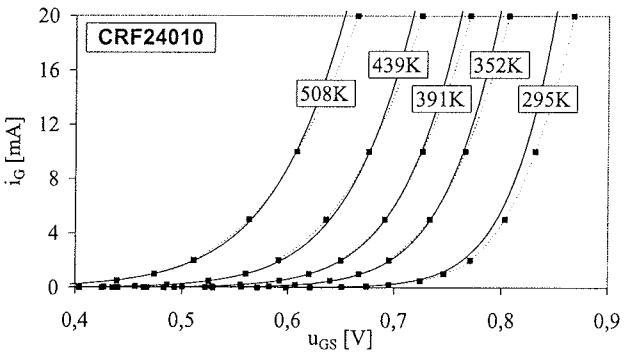

a)

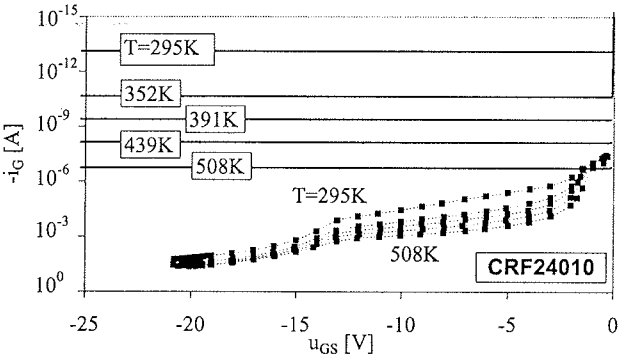

b)

Fig. 7. The characteristics of the Schottky diode D_1

As seen, the model fits well to measurements at the forward bias of the diode, whereas unacceptable discrepancies between theoretical and experimental results (differences higher then even 12 orders) occur at the reverse bias of the diode.

4. Conclusion

In the paper the usefulness of the Raytheon-Statz model for describing the SiC MESFET was estimated for the first time. The estimation of accuracy of the Raytheon-Statz model of the SiC MESFET (Cree Inc.) was performed by comparison of the measured and simulated characteristics in the wide range of the temperature.

The considered model takes into account the thermal dependences of: the pinchoff voltage, the saturation current and the band-gap energy. On the other hand, as seen from the investigation results (Figs. 2-7) to get the better agreement between measured and calculated characteristics, the dependencies: $V_{TO}(U_{DS})$, $U_{BR}(U_{GS},T)$ as well as the Schottky barrier lowering effect existing in the reverse biased diodes should be included in the considered model, which afterward could be implemented to SPICE as a subcircuit.

References

/1/ Östling M., "Silicon Carbide Devices for High Frequency and High Power - A State of the Art View", RadioVetenskap och Kommu-nikation RVK, Linköping, 2005.

/2/ "PSPICE A/D Reference Guide Version 10.0", Cadence Design Systems Inc., June 2003.

/3/ http://www.cree.com/products/pdf/crf24010.pdf.

Prof. Janusz Zarębski
Gdynia Maritime University
Department of Marine Electronics
Morska 83, 81-225 Gdynia, POLAND,
Tel. ++48 58 6901599, fax ++48 58 6217353
E-mail: zarebski@am.gdynia.pl

Prispelo (Arrived): 11.12.2006 *Sprejeto (Accepted):* 15.06.2007

A NEW MODEL FOR SIX TERMINAL HALL ELEMENT

Aleksander Sešek, Janez Trontelj

Faculty of Electrical Engineering, Ljubljana, Slovenia

Key words: six terminal Hall element model, integrated coil, coil heating modeling, offset voltage modeling

Abstract: A new model for integrated six terminal Hall element is presented in the paper. The model is based on six terminal Hall element patented in 1995. All magnetic field contributions are considered, external magnetic field and inducted field with integrated coil. A new model was developed to improve the offset modeling and to understand the influence of the integrated coil heating on the Hall element output signal.

Nov model Hallovega elementa s šestimi priključki

Kjučne besede: Hallov element s šestimi priključki, integrirana tuljavica, vpliv segrevanja integrirane tuljavice, vpliv napetosti ničenja

Izvleček: V članku je predstavljen nov model Hallovega elemeta s šestimi priključki. Temelji na Hallovem elementu s šestimi priključki, ki je bil patentiran leta 1995. V model so vključeni vsi prispevki magnetnih polj, ki vplivajo na odziv elementa. To sta zunanje magnetno polje in notranje magnetno polje, generirano z integrirano tuljavico. Nov model optimizira simulacije vpliva ničelne napetosti in vpliva segrevanja integrirane tuljavice na izhodni signal Hallovega elementa.

1 Introduction

Back in 1995 six terminal Hall element was patented /1/. In the same time simple Hall model with coil was introduced. Basic model consists of fundamental elements. Four resistors were introduced in the model as replacement for n-well silicon resistance. As seen from the Figure 1, each resistor corresponds to one of branches in the layout picture, using the clover leave shape of the Hall element.

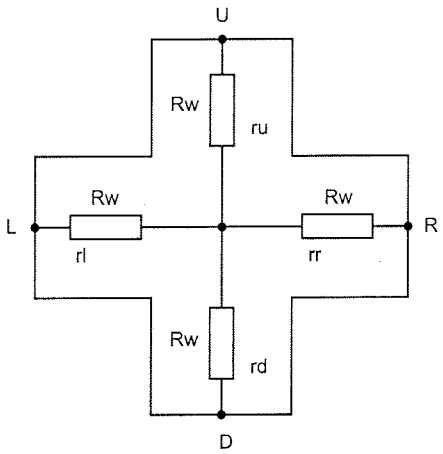

Fig. 1: Basic elements in Hall model

The contact terminals of Hall element are labeled as their orientation; U - Up, R - Right, D - Down and L as Left.

Next parameter which is implemented in basic model and the most important one is the Hall voltage. For the Hall voltage calculation the bias current needs to be measured which is flowing trough the element. Because we can spin the Hall element, the current must be measured in both possible directions, U - D and R - L. Then the current controlled voltage source is used to simulate Hall voltage on the opposite terminals. Finally the contribution to consider is the magnetic field, generated by the integrated coil. The solution is presented in Figure 2, which also presents the basic model for Hall element, introduced in 1995.

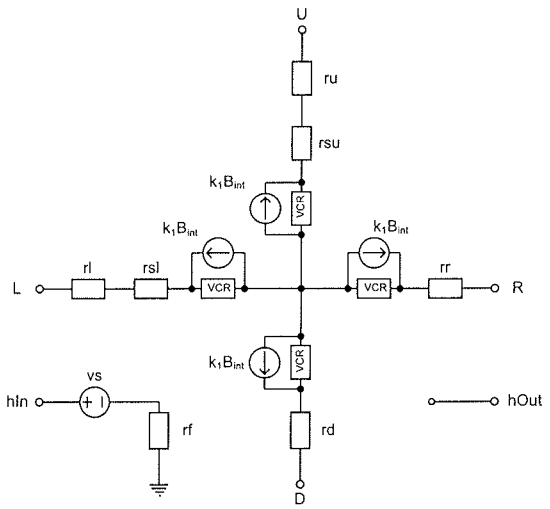

Fig. 2: Basic model of six terminal Hall element

In this figure we can see four basic well resistors ru, rr, rd and rl. Resistors rsl and rsu are the resistors for bias current sensing. Voltage drop on those resistors in mV is directly current value in mA if resistance is set to 1Ω. In each branch there is one closed loop which consists of VCR element (Voltage Controlled Resistor) and CCCS element (Current Controlled Current Source). VCR's are gu, gr, gd and gl elements in SPICE model and are controlled by the voltage on the current sensing resistor corresponding to which branch they are positioned. In the model the integrated coil resistance is replaced by resistor rf. Current trough the coil is in linear relation with magnetic field. With DC voltage source vs, this current is measured and it con-

trols all CCCS elements. The pair of VCR and CCCS needs to be positioned in each branch because VCR element returns 0 for negative voltage, as the Hall element can be spinned this voltage can be negative as well, so the second pair of VCR and CCCS takes over for Hall voltage calculation.

Sensitivity of Hall element /3/ and resistance of n-well silicon varies with technologies. We can adjust the variations for each technology by changing of the coefficients in VCR and CCCS relations and with changing the values of well resistors.

At the simulations where offset influence is investigated, an external resistor between two terminals is used, i.e. if the current flows from U - D an external resistor between U and L or U and R is connected. The offset voltage is mainly caused with the process, nonidealities due to the tolerances in dimensions, etching, etc. Using the method of changing resistance between terminals, the offset voltage appears at the output, but from this approach we can not see clearly how big the actual variation of well resistance is. Second difficulty in simulations with external offset resistor is long settling time. Resistors values in the range 100 times larger then the resistance of the Hall element branch need to be used, to achieve correct offset levels. The settling constant is far too long, to simulate the spinning of the Hall element, where frequencies around 500kHz are used.

In the simple model, there is no external magnetic field influence element. Simulations with basic Hall model are done only with the internal coil. We need to add the external field and the internal generated field on the same terminal to observe the influence on the output. This approach does not give as clear separate contributions of each part of the magnetic field.

Influence of the coil heating is also not included in the basic model. Current flowing trough the coil causes coil heating which directly affect the Hall element output voltage.

2 New Hall model

In this section all problems mentioned above are solved by proposing one compact model of the Hall element. All parameters are characterized to reach the output response as close as possible to match the real measurement results.

Distribution of resistances in the basic model, are done as in the layout topology, in four separate branches. For the offset voltage simulation, this is not appropriate. A better solution is the bridge connection of four resistors, as shown in Figure 3.

In this case the offset voltage can be easily modeled by resistor value variations, according to the parameters derived from silicon foundry matching data. Relation between resistance variations and output offset voltage is linear and

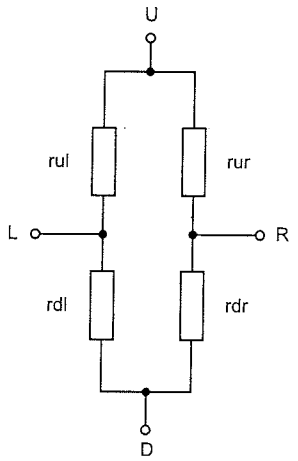

Fig. 3: Resistors bridge connection

clear. Small change in resistance can cause a large output offset voltage, but it does not influence the settling constant. The resistances in the branches are now different than in the previous model. Total Hall element resistance is the same and output signal as well. In the Table 1, the offset voltage Voff simulation results are listed, were Δrur is resistance step value.

Table 1: Offset simulation results

ΔRur[Ω]	Voff[mV]
0	0
1	-0,259
2	-0,517
5	-1,292
10	-2,582
20	-5,159
50	-12,859
-1	0,257
-2	0,516
-5	1,292
-10	2,587
-20	5,180
-50	12,990

On Figure 4 graphical result of the offset voltage is shown.

On the figure 5a the modeling of Hall voltage is added to the bridge model of Hall element. Two separate voltage sources are included for external and internal field contributions in each of bridge branches. Each voltage source consists of VCR and CCCS as in the basic model. For current sensing, two resistors are added in the common Up and Right branch, ru and rr. Outside of the bridge, two sub circuits are added. The first one represents the coil, its resistance r_{coil} and voltage source vs as current sensing element. The second one replaces the external magnetic field with a voltage source vm and resistor r_m = 1Ω to provide the current used in CCCS element.

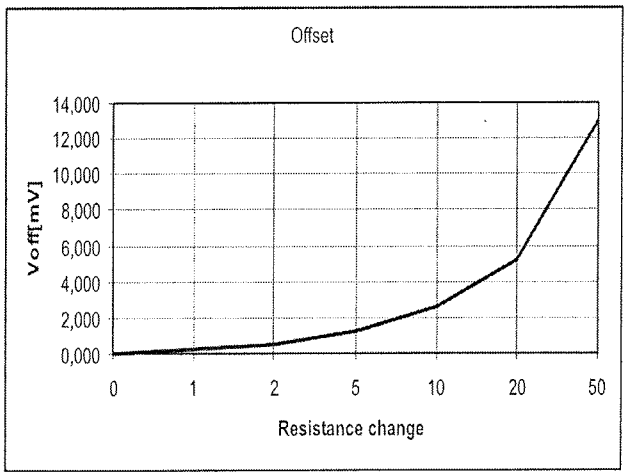

Fig. 4: Offset vs. Δrur

Relation for internal magnetic field B_{int} is given by the equation k_1B_{int}. Constant k_1 is multiplying factor for coil generated magnetic field, which contains all parameters defined by the process. This constant is basically the sensitivity of Hall element for internal field and the constant k_2 is the sensitivity of the element for external magnetic field.

Heating of the integrated coil around the Hall element due to the current flowing trough, causes signal distortion of Hall element output signal /4/. The detailed analysis of the output signal provided the parameters for modeling this phenomenon. It has been determined that relevant distortion harmonic component is the second, due to of relation between current and heating, which is quadratic (Joule losses).

In Figure 5b, the full Hall model is presented, including the heating influence generators. They are positioned in left and bottom part, to meet the modeling requirements for the design and layout. Two sub-circuits were used, to provide correct function in both positive and negative coil current. This is necessary as the negative coil current returns a zero for VRC in SPICE simulator.

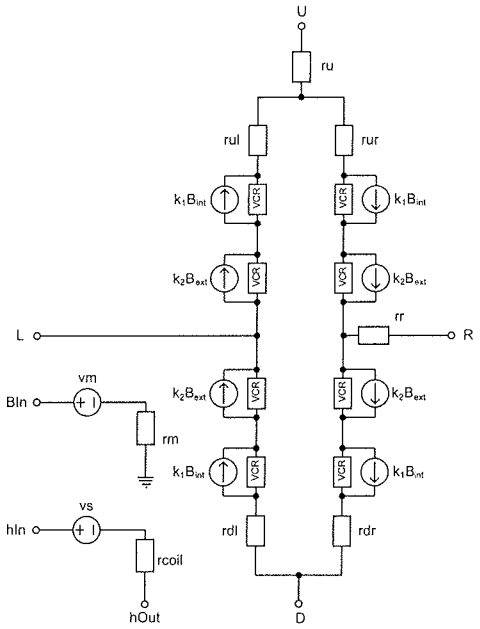

Fig. 5a: Simplified model of Hall element

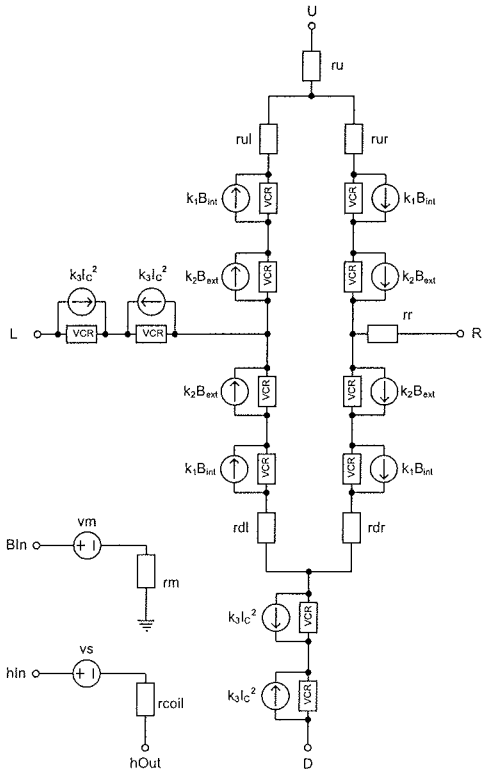

Fig. 5b: Full model of Hall element

In the time diagram (Figure 6), simulation of Hall element model is shown. All simulations are done with 0.6um CMOS technology parameters. In the upper trace the input coil current hln is presented. The middle trace shows the output signals, in this case R and L, and the bottom trace is the difference between them. In our simulation we have 10mA of coil current and the Hall element bias current 1mA.

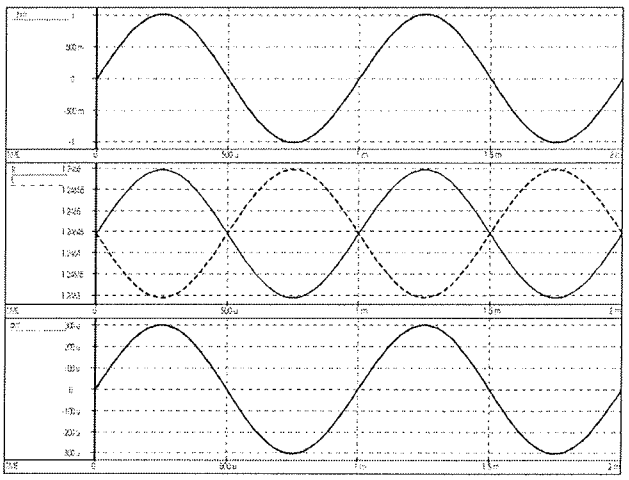

Fig. 6: Simulation result for internally generated magnetic field by integrated coil current

In figure 7 the simulation results of external magnetic field are shown. The upper trace is input Bin voltage representing external field, as voltage.1V level corresponds to 10mT of external field. As in diagram shown in fig. 7 the traces in the middle are the Hall element outputs R and L, and bottom trace is the difference between both outputs.

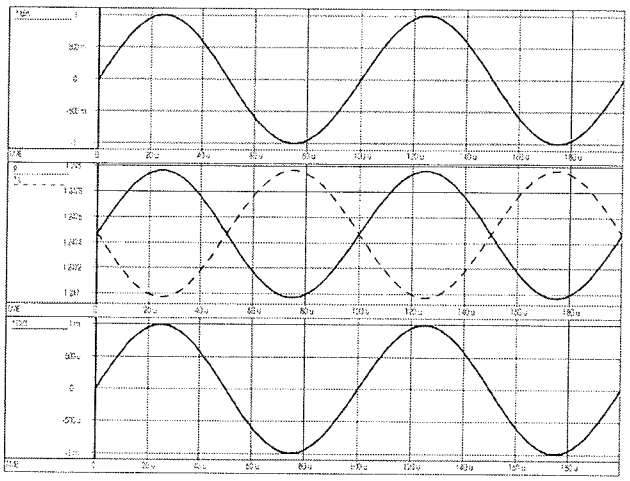

Fig. 7: Simulation results for external magnetic field

Heating effect, which is modeled by generators, is described with k_3Ic^2 function. Constant k_3 presents the heating factor and I_C is the current flowing trough the coil. Factor k_3 is a function of coil geometry and resistance. Simulation for thermal influence on the output was done with internal magnetic field. As shown there are distortions at peak values of each output in the middle trace on figure 8.

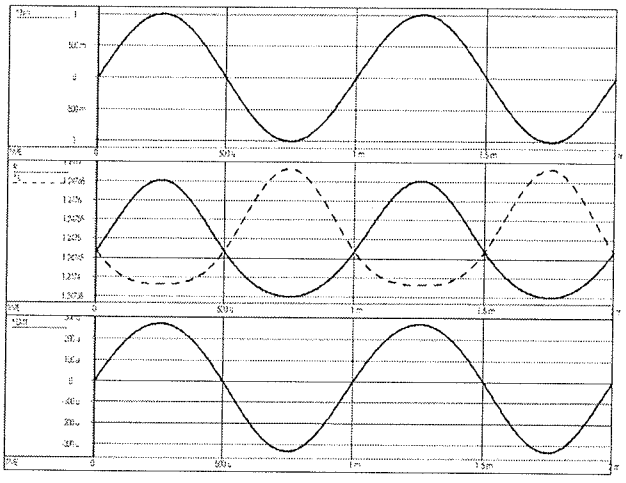

Fig. 8: Thermal effect of coil current

Differential output signal is shown on the bottom trace of figure 9. Exact mechanism of distortion effect is caused by the temperature gradient trough the element. Positive peaks are flattened and negative are sharpened, because of the second harmonic component added.

For offset voltage modeling a proposal model does not offer an user friendly simulation approach so we decided to modify the model with the offset voltage as parameter which

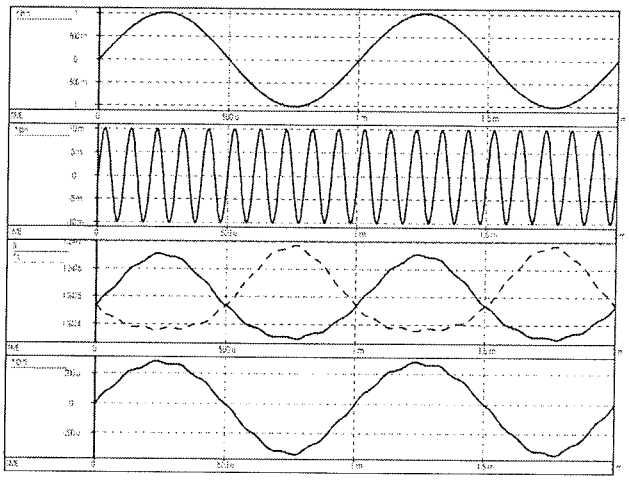

Fig. 9: Differential output signal as result of internal and external generated magnetic field

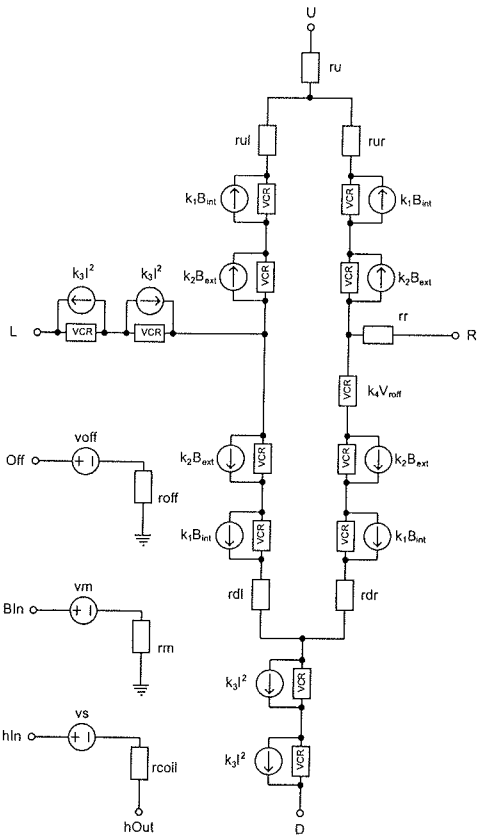

Fig. 10: Final Hall element model

can be derived from matching characteristics of process. The modified model is shown in figure 10.

We have added a VCR element, controlled by voltage on roff resistor. Additional pin was added in the model labeled as Off. A voltage source voff was included in the offset branch for supervising the current flowing trough roff resistor. Resistor roff is n-well type to take into account the temperature variations of the offset. Voltage equation k_4V_{roff} describe the offset voltage dependence on voltage on resistor Vroff. The constant k_4 is the sum of all process parameters influencing the offset voltage /2/ and is set to

achieve a maximal possible offset ~ 10mV at 1V on Off pin. As the resistor roff is a n-well resistor, we can simulate temperature dependence of the offset trough voltage. The simulation shows 0.66%/K temperature coefficient of the offset voltage around room temperature, and up to 0.9%/K TC of the offset voltage in the range from -40°C to 140°C.

3 Measurement results

Measurements were done to verify the model coil heating influence on the output signal. The output voltage of Hall element was amplified with gain of 94,72.

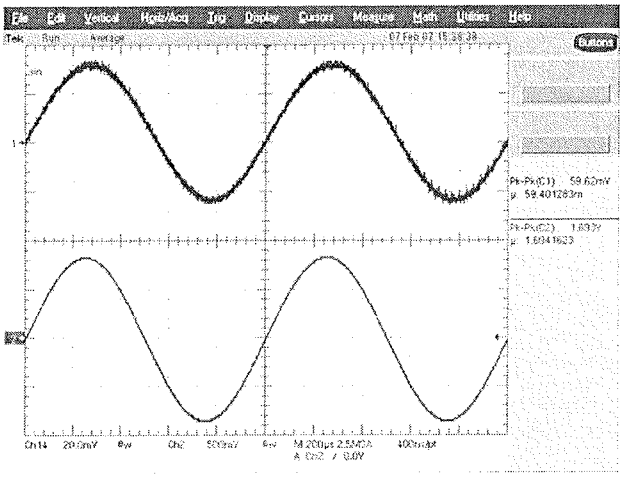

Fig. 11a: Oscilloscope picture at I_C = 5mA

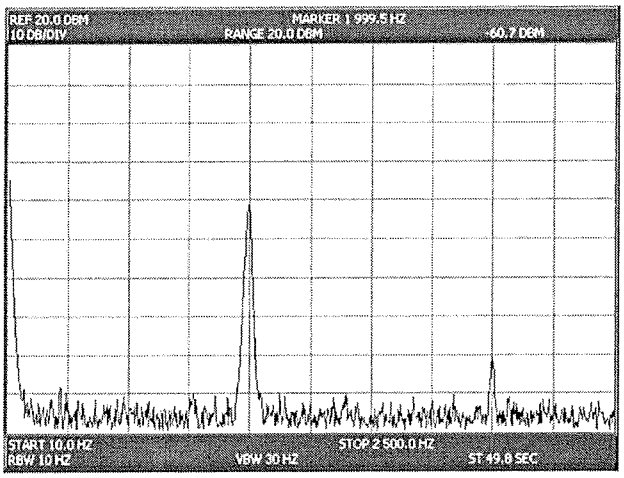

Fig. 11b: Spectral components at I_C = 5mA

Figure 11a is oscilloscope picture of the output signal shown on upper trace for coil current I_C = 5mA. For such current the distortion is not clearly visible, but it is seen in figure 11b, where the spectrum of the output already shows a second harmonic component at -38dB, compared to the first harmonic component.

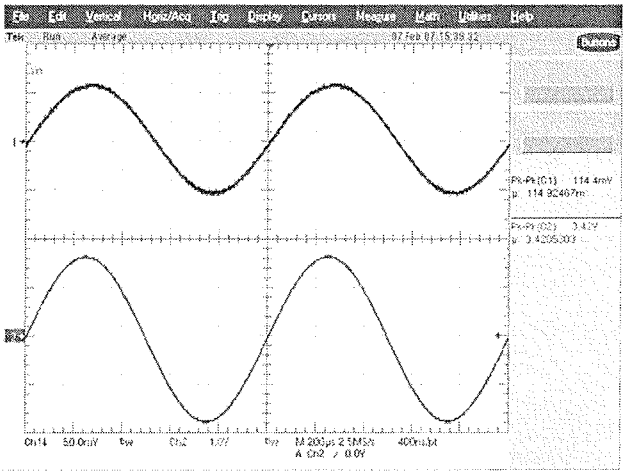

Fig. 12a: Oscilloscope picture at I_C = 10mA

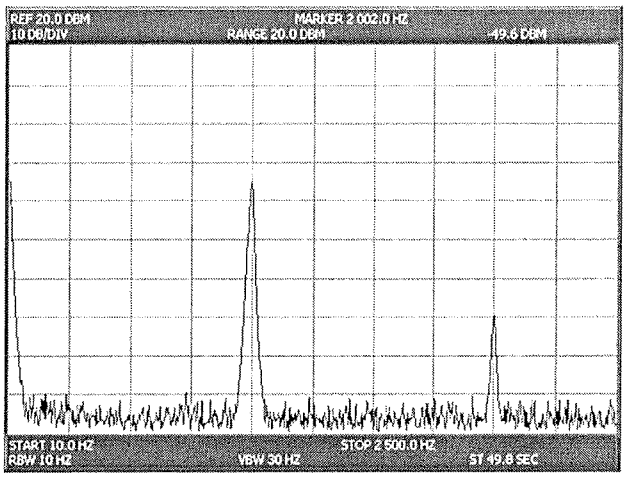

Fig. 12b: Spectral components at I_C = 10mA

By increasing the coil current to 10mA (figure 12a), the second harmonic is increased for 12dB (figure 12b), which is in good accordance to the simulation model.

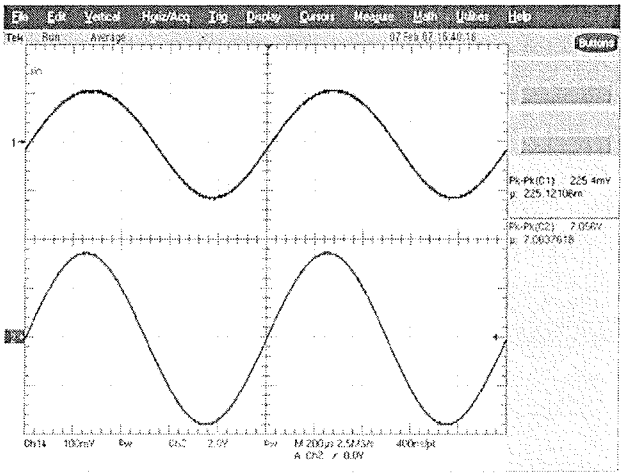

Fig. 13a: Oscilloscope picture at I_C = 20mA

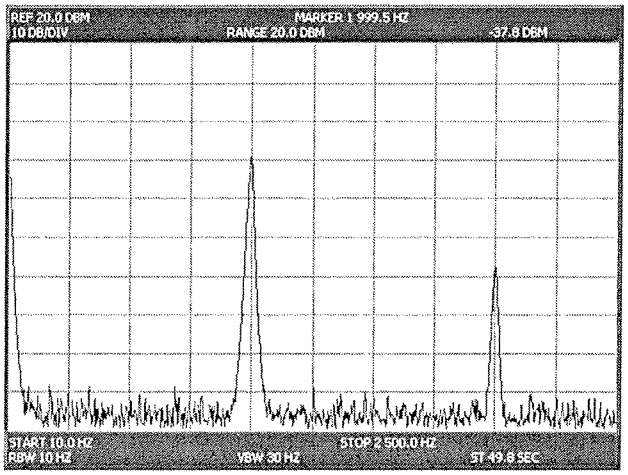

Fig. 13b:Spectral components at I_C = 20mA

Further increase of the coil current to 20mA (figure 13a) increases the second harmonic component for additional 12dB (figure 13b), as expected.

4 Conclusions

New six terminal Hall element model was developed and described in the paper. In presented model all magnetic contributions were taken into account including internal magnetic field, external magnetic field, Hall element offset voltage and its temperature dependence. In addition a distortion of the output signal due to the integrated coil heating was included in model. A measurement on Hall integrated element with coil showed a good compliance with the proposed model.

5 References

/1/ Trontelj Janez, Opara Roman, Pleteršek Anton: *Integrirano vezje z magnetnim senzorjem : patent št. 9300622 : patent je podeljen z odločbo št. 304-60/93-622-MT-5 z dne 24.07.1995.* Ljubljana: Urad RS za intelektualno lastnino, 1995. [COBISS.SI-ID 5196077]

/2/ Trontelj Janez: *Smart integrated magnetic sensor cell, Inf. MIDEM*, 1999, let. 29, št. 3, str. 126-128, graf. prikazi, sheme. [COBISS.SI-ID 1725524]

/3/ Trontelj Janez: *Optimization of integrated magnetic sensor by mixed signal processing.* V: PIURI, Vincenzo (ur.), SAVINO, Mario (ur.). *IMTC/99: proceedings of the 16th IEEE Instrumentation and Measurement Technology Conference, Venice, Italy - May 24-26, 1999*, (Conference proceedings - IEEE Instrumentation/Measurement Technology Conference). Piscataway: IEEE Service Center, 1999, vol. 1, str. 299-302, ilustr. [COBISS.SI-ID 1490772]

/4/ Trontelj Janez: *Integrirano vezje z magnetnimi senzorji, obdanimi s testnimi tuljavicami : številka patenta SI 20294 A : datum objave 31.12.2000*. Ljubljana: Urad RS za intelektualno lastnino, 2000. [COBISS.SI-ID 3537748]

univ.dipl.ing.el. Aleksander Sešek
University of Ljubljana
Faculty of Electrical Engineering
Tržaška cesta 25, SI-1000 Ljubljana, Slovenija
E-mail:aleksander.sesek@gmail.com
Tel:+386 1 4768 727, Fax: +386 1 4264 644

prof.dr.Janez Trontelj
University of Ljubljana
Faculty of Electrical Engineering
Tržaška cesta 25, SI-1000 Ljubljana, Slovenija
E-mail: janez.trontelj1@guest.arnes.si
Tel:+386 1 4768 333, Fax: +386 1 4264 644

Prispelo (Arrived): 01.03.2006 *Sprejeto (Accepted):* 15.06.2007

INERTIAL AND MAGNETIC SENSORS: THE CALIBRATION ASPECT

David Jurman, Marko Jankovec, Roman Kamnik, Marko Topič

Faculty of Electrical Engineering, University of Ljubljana, Ljubljana, Slovenia

Key words: inertial measurement unit, accelerometer, gyro, magnetic sensor, calibration

Abstract: A powerful procedure to calibrate and align the Micro Electro-Mechanical System inertial sensors and the Anisotropic-MagnetoResistive magnetic field sensors is presented. The suggested method is cost effective and suitable for the in-field calibration because it is based on techniques that do not need any complex mechanical platforms for the sensor manipulation.

To evaluate the calibration procedure, a modular Magnetic and Inertial Measurement Unit - consisting of three inertial sensor units, a magnetic sensor unit and a control unit - has been developed and calibrated according to the proposed method. The obtained results demonstrate accuracy and stability of the described calibration procedure.

Inercialni in magnetni senzorji: kalibracijski vidik

Kjučne besede: inercialna merilna enota, pospeškometer, žiroskop, elektronski kompas, kalibracija senzorjev

Izvleček: V prispevku je predstavljena kakovostna metoda za kalibracijo in poravnavo inercialnih MEMS (Mikro Elektro-Mehanski Sistem) in magnetnih AMR (Anizotropni MagnetoRezistivni) senzorjev. Predstavljena metoda je sestavljena iz kalibracijskih tehnik, ki so primerne za terensko uporabo, saj ne potrebujejo nikakršnih zapletenih mehanskih naprav za manipulacijo senzorjev.

Z namenom ovrednotenja kalibracijske metode je bila zgrajena modularna magnetna in inercialna merilna enota (MIMU), ki je sestavljena iz treh inercialnih senzorskih enot, ene magnetne senzorske enote ter centralne kontrolne enote. MIMU je bil uspešno kalibriran na podlagi predstavljene metode. Rezultati kalibracije pri sobni temperaturi pa izkazujejo natančnost in stabilnost kalibracijskega postopka.

1. Introduction

Several Integrated Circuit (IC) manufacturers (Analog Devices /1/, Freescale /2/, Honeywell /3/, etc.) are producing low-cost Micro Electro-Mechanical System (MEMS) inertial sensors and Anisotropic-MagnetoResistive (AMR) magnetic sensors that have allowed the full swing of the Inertial Measurement Unit (IMU) and the electronic compass systems. Low-cost miniature IMUs and electronic compasses are found in various applications like unmanned vehicles /4/, navigation devices /5/, human motion tracking /6/, virtual reality gadgets /7/ and many more.

However, the MEMS and the AMR sensors have one significant drawback. The electrical parameters of such sensors are not well defined and usually scatter for as much as 10%. Additional error sources are caused by the alignment problems during the IMU and electronic compass assembly. Therefore, each manufactured device using such sensors must be calibrated prior to the use or even recalibrated several times during the lifetime.

There are quite a few possible methods to calibrate the IMU and the electronic compass, but the majority of them involve complex mechanical platforms for the device manipulation or even the optical tracking systems /8/. These procedures are appropriate for the laboratory operation, but are completely unsuitable for the in-field calibration.

In this paper a new calibration procedure, which is based on the local Earth's gravitational and magnetic field, is presented. The procedure is a combination of calibration techniques which are simple to perform; they do not need any extra instruments and are convenient for the in-field use. Above all, the absence of any additional instrumentation leads to the reduction of the production costs and the final product price. For this reason, a miniature Magnetic and Inertial Measurement Unit (MIMU) has been developed /9/ to test and evaluate these calibration procedures.

2. Magnetic and inertial measurement unit

In order to study different degrees of sensor misalignment we have developed a modular system, where several detachable sensor units are connected to a central control unit. The MIMU consists of three inertial sensor units (ISU), one magnetic sensor unit (MSU) and a control unit (CU) (see Figure 1) which are enclosed in a cubic plexiglas casing /9/.

Each ISU contains two MEMS sensors: a single-axis angular rate gyroscope (ADXRS150, full-scale range of ±150 °/s) and a two-axis accelerometer (ADXL203, full-scale range of ±1.7 g), both made by Analog Devices. With the orthogonal positioning of three ISUs a complete six degrees-of-freedom (6 DOF) inertial measurement system was obtained.

MSU comprises two AMR sensors: a single-axis HMC1001 and a dual-axis HMC1002 (produced by Honeywell) with

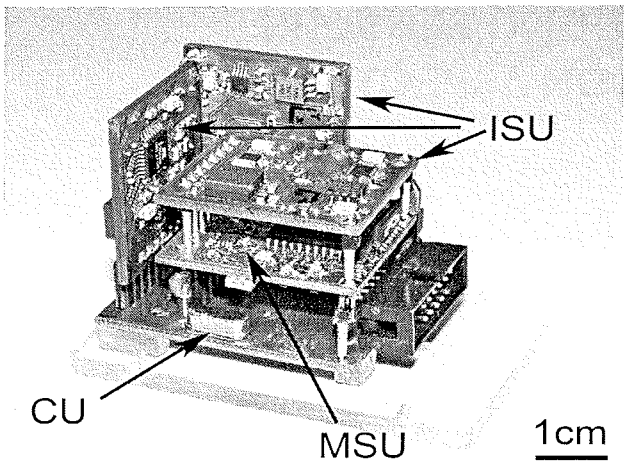

Fig. 1: Realized MIMU.

the full-scale range of $\pm 2 \cdot 10^{-4} \cdot T$, forming a complete three-dimensional electronic compass. MSU also contains a high current flipping circuit for inverting the sensor's transfer function, which reduces the cross-axis effects and temperature drift.

During the development process, special attention was paid to the printed circuit board layout and analogue signal processing, to prevent coupling of additional noise and interferences to the sensor's output signals.

3. Sensor model

Prior to the calibration, the sensor model of accelerometer, gyro or magnetic field sensors must be known and the model parameters should be identified. The sensor model parameters can be divided in two groups: the electrical parameters and the mechanical parameters.

Each sensor's electrical characteristic is specified in its datasheet. Besides the sensor's sensitivity to the input physical quantity and the sensor's bias, there are also other unwanted effects specified, like the transfer function's nonlinearity and cross-axis sensitivity. However, these effects can be easily neglected, since they are suppressed by means of the system design. Thus it is adequate to determine only the sensitivities and the biases during the calibration procedure.

The other group members, i.e. the mechanical parameters, result from the fact that usually the three-dimensional IMU consists of several sensors with one or two sensitivity axes. These sensitivity axes should be perpendicular to each other in order to form the orthogonal sensor triplet. To achieve adequate sensor orthogonality advanced precise assembly procedures must be employed /10/, but these procedures are time consuming and above all present considerable augmentation in production costs. The next error source is the misalignment of the sensor triplet to the sensor system casing and the mutual misalignment of various sensor triplets, which are also critical because they cause system errors. These two subjects - the orthogonalization and the misalignment - are also considered in the sensor model with the intention to be compensated in the software.

According to the previous sections, we can put down the sensor model as:

$$\vec{y}_k = S_k \cdot T_k \cdot R_k \cdot \vec{u}_k + \vec{b}_k \; ; \quad k = sensor \;\; type \;\; (g,a,m), \quad (1)$$

where the index k represents the type of the sensor triplet (g, a or m ; gyro, accelerometer or magnetic field sensor, respectively). The measured physical quantity $\vec{u}_k$, the sensor triplet bias $\vec{b}_k$ and the sensor triplet output voltage $\vec{y}_k$ are arranged in the vectors:

$$\vec{u}_k = \begin{bmatrix} u_{kx} \\ u_{ky} \\ u_{kz} \end{bmatrix}, \quad \vec{y}_k = \begin{bmatrix} y_{kx} \\ y_{ky} \\ y_{kz} \end{bmatrix}, \quad \vec{b}_k = \begin{bmatrix} b_{kx} \\ b_{ky} \\ b_{kz} \end{bmatrix}.$$

On the other hand, the sensors' sensitivities S_k and the mechanical parameters - the orthogonalization T_k and the misalignment R_k - are incorporated in the matrices:

$$S_k = \begin{bmatrix} s_{kx} & 0 & 0 \\ 0 & s_{ky} & 0 \\ 0 & 0 & s_{kz} \end{bmatrix}, \qquad T_k = \begin{bmatrix} 1 & 0 & 0 \\ \cos\alpha_k & 1 & 0 \\ \cos\beta_k & \cos\gamma_k & 1 \end{bmatrix},$$

$$R_k = \begin{bmatrix} r_{k,11} & r_{k,12} & r_{k,13} \\ r_{k,21} & r_{k,22} & r_{k,23} \\ r_{k,31} & r_{k,32} & r_{k,33} \end{bmatrix}.$$

Orthogonalization matrix T_k transforms the vector expressed in the orthogonal sensor reference frame *ko* into the vector expressed in the non-orthogonal sensor reference frame *k* (see Figure 2).

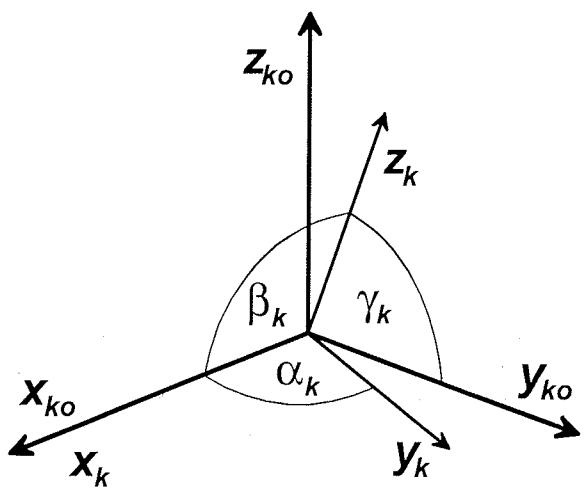

Fig. 2: Orthogonalization of the sensor triplet frame k.

The matrix T_k is constructed using the Gram-Schmidt orthogonalization process /11/. The Gram-Schmidt algorithm takes a finite, linearly independent set of vectors and generates an orthogonal set that spans the same subspace. If the angles α_k, β_k and γ_k are close to 90° (which is usually the case in such systems) some approximations may be made without any significant loss of the accuracy:

$$T_k = \begin{bmatrix} 1 & 0 & 0 \\ \cos\alpha_k & \sin\alpha_k & 0 \\ \cos\beta_k & \cos\gamma_k & \sqrt{1-\cos^2\beta_k-\cos^2\gamma_k} \end{bmatrix}\Bigg|_{\alpha_k,\beta_k,\gamma_k\approx 90°} \approx \begin{bmatrix} 1 & 0 & 0 \\ \cos\alpha_k & 1 & 0 \\ \cos\beta_k & \cos\gamma_k & 1 \end{bmatrix} \quad (2)$$

Misalignment matrix R_k is an Euler angles parameterized rotation matrix, which rotates (aligns) the platform reference frame *p* to the orthogonal sensor reference frame *ko* (see Figure 3):

$$R_k = \begin{bmatrix} 1 & 0 & 0 \\ 0 & \cos\phi_k & \sin\phi_k \\ 0 & -\sin\phi_k & \cos\phi_k \end{bmatrix} \cdot \begin{bmatrix} \cos\vartheta_k & 0 & -\sin\vartheta_k \\ 0 & 1 & 0 \\ \sin\vartheta_k & 0 & \cos\vartheta_k \end{bmatrix} \cdot \begin{bmatrix} \cos\psi_k & \sin\psi_k & 0 \\ -\sin\psi_k & \cos\psi_k & 0 \\ 0 & 0 & 1 \end{bmatrix} \quad (3)$$

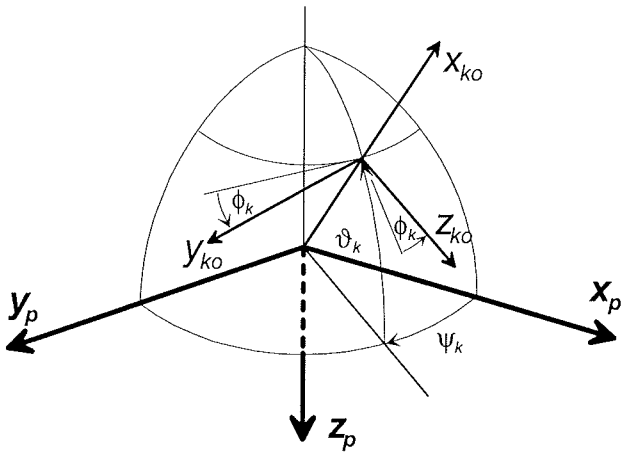

Fig. 3: Misalignment of the sensor triplet frame ko.

This sensor model is used for all sensor triplets used in the MIMU irrespective of the sensor type. When all the 12 parameters (s_{kx}, s_{ky}, s_{kz}; b_{kx}, b_{ky}, b_{kz}; α_k, β_k, γ_k; ψ_k, ϑ_k, ϕ_k) for the each triplet are known, then the estimate $\hat{\vec{u}}_k$ for the observed physical quantity $\vec{u}_k$ is:

$$\hat{\vec{u}}_k = R_k^{-1} \cdot T_k^{-1} \cdot S_k^{-1} \cdot (\vec{y}_k - \vec{b}_k). \quad (4)$$

Mechanical parameters (orthogonalization and misalignment parameters) are assumed to be independent of the temperature and the time during the normal operation (without any excessive shocks and stresses present). Therefore they need to be determined only once, e.g. at the end of their production phase. Electrical parameters, on the other hand, must be reestablished from time to time because they drift with time. The gyro bias has been identified to be the most critical parameter from this point of view and it must be measured at every start up (the maximum drift is ±12% - over the entire operating temperature range). For the outdoor operation, the electrical parameters need to be determined as a function of the temperature.

4. Accelerometer and magnetic sensor calibration

For the calibration of the accelerometer triplet and the magnetic sensor triplet, the scalar field calibration method is applied /12, 13/. This calibration method is based on the local Earth's gravity and the local Earth's magnetic field. It derives benefit from the fact that the magnitude of the measured Earth's gravity acceleration and magnetic field is independent of the measurement system's orientation; the MIMU in our case. The only disadvantage of this method is that the misalignment parameters cannot be estimated as they form the rotation matrix with norm +1, which does not affect the vector magnitude.

The parameters which can be determined with the scalar field calibration are grouped in the calibration parameter vector $\vec{p}_{k\_cal}$:

$$\vec{p}_{k\_cal} = [s_{kx} \quad s_{ky} \quad s_{kz} \quad b_{kx} \quad b_{ky} \quad b_{kz} \quad \alpha_k \quad \beta_k \quad \gamma_k]^T. \quad (5)$$

The parameter vector $\vec{p}_{k\_cal}$ is established by the minimization of the objective function $O(\vec{p})$. The objective function is defined as the mean square error between the reference value u_{ref} and the corresponding data vector $u_n(\vec{p})$:

$$O(\vec{p}) = \frac{1}{N}\sum_{n=1}^{N}\left(u_{ref} - u_n(\vec{p})\right)^2, \quad (6)$$

where *N* is the number of measured values in the data vector. The reference value is the normalized value of the local gravity acceleration or the Earth's magnetic field ($u_{ref} = 1$ in both cases), and it is compared to the gravity norm estimate ($u_n(\vec{p}) = \|\hat{\vec{a}}_n\|$) or the magnetic field norm estimate ($u_n(\vec{p}) = \|\hat{\vec{m}}_n\|$) for the accelerometer or the magnetic sensor, respectively.

The MIMU must be exposed to at least nine different orientations since nine parameters (Eq. 5) need to be determined and several data points should be acquired at each orientation. The precise knowledge of the orientation is not needed; however it is important that the MIMU is stand-

still during the data acquisition to minimize the noise in the sensors' outputs. The objective function can be minimized with one of the optimization methods, after the data set has been acquired. In our case the constrained Newton optimization method is applied. The initial values of the parameters and the constraints are set according to the typical values quoted in the sensors' datasheets.

The remaining three parameters, the misalignment angles (Eq. 7) of the accelerometer triplet and electronic compass, are obtained following the approach presented in /14/.

$$\vec{p}_{k\_align} = [\psi_k \quad \vartheta_k \quad \phi_k]^T \tag{7}$$

If the ideally aligned MIMU rotates about the one of its sensitivity axes, then the data of the corresponding accelerometer and magnetic sensor triplet sensitivity axis should remain constant. But the data are deviated due to the sensor triplet misalignment. The aim of the alignment procedure is to minimize these deviations.

The alignment procedure has two steps. The first step assumes two rotations, one about the roll axis (x-axis) proceeding with the second rotation about the yaw axis (z-axis). In the data processing step the deviation of x-axis data is first minimized by optimizing the heading and elevation misalignment angle (ψ_k, ϑ_k). With these two parameters defined, the z-axis data can be partially aligned. The complete alignment is achieved by the minimization of the partially aligned z-axis data deviation, where the bank misalignment angle (ϕ_k) is optimized. The data deviation is expressed as the mean square error between the acquired data vectors ($u_n(\vec{p}) = \hat{a}_{i,n}$ for the accelerometer triplet or $u_n(\vec{p}) = \hat{m}_{i,n}$ for the magnetic sensor triplet) and their mean values ($u_{ref} = \bar{\hat{a}}_i$ or $u_{ref} = \bar{\hat{m}}_i$, where *i* stands for the sensitivity axis of interest).

The rotation about the desired axis is performed by putting the MIMU on the flat surface in the way that the axis of interest is normal to the surface. The surface should be placed perpendicularly to the excitation vector (the gravity or the Earth's magnetic field), for the best alignment results. In such position the current sensitivity axis is maximally excited in the cross-axis direction and the acquired data are maximally deviated. Then one revolution about the surface's normal is accomplished and the gravity acceleration and the Earth's magnetic field are acquired in several steady-state points.

5. Rate gyro calibration

The scalar field calibration is inconvenient for the rate gyro triplet calibration, since a rotational platform with known and stable angular rate is required. For this reason the method based on /15/ was developed. The original method was upgraded and modified in such manner that it incorporates the orthogonalization effects as well.

First of all, the gyro triplet bias vector $\vec{b}_g$ is measured. The MIMU is kept in standstill and the bias vector is determined as the mean value of the gyros' data during the data acquisition period.

In order to determine the remaining nine parameters (s_{gx}, s_{gy}, s_{gz}; $\alpha_g, \beta_g, \gamma_g$; $\psi_g, \vartheta_g, \phi_g$) another three measurements must be carried out. Let us assume that we have a rotational platform with known constant angular rate. We carry out three rotations, each about the individual sensitivity axis. The data captured during the rotations are organized in the matrices: the applied angular rates are arranged on the diagonal of the matrix W_g and the bias corrected angular rate estimates $\vec{y}_g - \vec{b}_g$ (Eq. 1) from the gyro triplet are arranged in the matrix v_g, where the element $r_{g,ij}$ represents the *i*-th gyro's output when the rotation about the *j*-th axis is accomplished.

$$v_g = S_g \cdot T_g \cdot R_g \cdot W_g \tag{8}$$

$$v_g = \begin{bmatrix} r_{g,xx} & r_{g,xy} & r_{g,xz} \\ r_{g,yx} & r_{g,yy} & r_{g,yz} \\ r_{g,zx} & r_{g,zy} & r_{g,zz} \end{bmatrix}, \quad W_g = \begin{bmatrix} \omega_x & 0 & 0 \\ 0 & \omega_y & 0 \\ 0 & 0 & \omega_z \end{bmatrix}.$$

The necessity for the rotational platform can be suppressed regarding the fact that the Eq. (8) is linear (the matrices S_g, T_g and R_g are constant). If the Eq. (8) is integrated over the observed period of time then the angular rate matrix W_g is transformed into the angle matrix A_g and the matrix v_g with the bias corrected angular rate estimates is transformed into the angles estimate matrix Y_g.

$$Y_g = S_g \cdot T_g \cdot R_g \cdot A_g \tag{9}$$

As the result of the integration in the time domain all the operations are made in the angles domain, from now on. Instead of the angular velocity, the angle of rotation must be accurately defined. Indeed, the measurement of the rotation angle is much simpler than the measurement of the angular rate.

The calibration procedure for the rate gyro is therefore as follows. The MIMU is placed on the flat surface and a full revolution about the surface normal axis is made. Then two successive rotations about the remaining axes are completed. The applied angles of rotation are written in the matrix A_g and the angle estimates obtained from the gyro triplet measurements are inserted in the matrix Y_g.

The matrices A_g and Y_g are composed of the measured values, while the matrices S_g, T_g, R_g are determined following the Eq. (10) to Eq. (15), where special facts about the matrices were relevant: (i) the sensitivity matrix S_g is a diagonal matrix (it can be also treated as an upper triangu-

lar matrix), (ii) the orthogonalization matrix T_g is a unit lower triangular matrix, and (iii) the misalignment matrix R_g is an orthonormal matrix.

The matrices with the known (measured) data are arranged on the left side meanwhile the matrices composed of the unknown gyro triplet calibration parameters are on the right side of the Eq. (10):

$$Y_g \cdot A_g^{-1} = S_g \cdot T_g \cdot R_g \tag{10}$$

The symmetrical matrix is constructed by right multiplying each side of the Eq. (10) with its transpose:

$$(Y_g \cdot A_g^{-1})(Y_g \cdot A_g^{-1})^T = (S_g \cdot T_g \cdot R_g)(S_g \cdot T_g \cdot R_g)^T; \tag{11}$$

then the misalignment matrix R_g is abridged, because of its orthonormality:

$$(Y_g \cdot A_g^{-1})(Y_g \cdot A_g^{-1})^T = (S_g \cdot T_g)(S_g \cdot T_g)^T. \tag{12}$$

The symmetric positive-definite matrix $(Y_g \cdot A_g^{-1})(Y_g \cdot A_g^{-1})^T$ is decomposed by the Cholesky decomposition into a lower triangular matrix $S_g \cdot T_g$ and its transpose:

$$S_g \cdot T_g = chol\left[(Y_g \cdot A_g^{-1})(Y_g \cdot A_g^{-1})^T \right]^T. \tag{13}$$

The sensitivity and the orthogonalization matrices are retrieved by the LU decomposition of the matrix $S_g \cdot T_g$, where the T_g is a lower and the S_g is an upper triangular matrix:

$$[T_g, S_g] = LU(S_g \cdot T_g). \tag{14}$$

Finally, the misalignment matrix R_g is obtained by the following matrix manipulation:

$$R_g = T_g^{-1} \cdot S_g^{-1} \cdot Y_g \cdot A_g^{-1}. \tag{15}$$

6. Calibration results

The MIMU was calibrated and aligned at the room temperature according to the presented procedure. The data acquisition was done using the LabVIEW, the optimization algorithm and the matrix calculations are on the other hand performed using the Matlab programming package. The results of the series of five calibration sequences are presented in the Figures 4-6. The y-axis span of the electrical parameters' bar charts corresponds to the parameter span specified in the sensors' datasheets. From the charts it is seen that all determined parameters are within the specified range. The mechanical parameters are also close to the ideal values: 90° for the orthogonalization and 0° for the alignment. The time stability and accuracy of the calibration method was demonstrated by performing several calibration series during a few months period, where all the calibration results manifested minimum scattering of the obtained calibration parameters. The parameters scattering is a consequence of the sensor noise as well as the noise introduced by the analogue to digital conversion.

The calibration was performed at the room temperature; however if the sensors are used in the temperature variable environment, then we would require temperature dependent calibration of the sensors' parameters.

The magnetic sensor triplet calibration should be performed in magnetically clean environment where Earth's magnetic field is undisturbed by the various large scale magnetic disturbances, e.g. major power supply wires, larger electric equipment, etc. However the high frequency magnetic disturbances and noise is effectively rejected by the analogue and digital filtering.

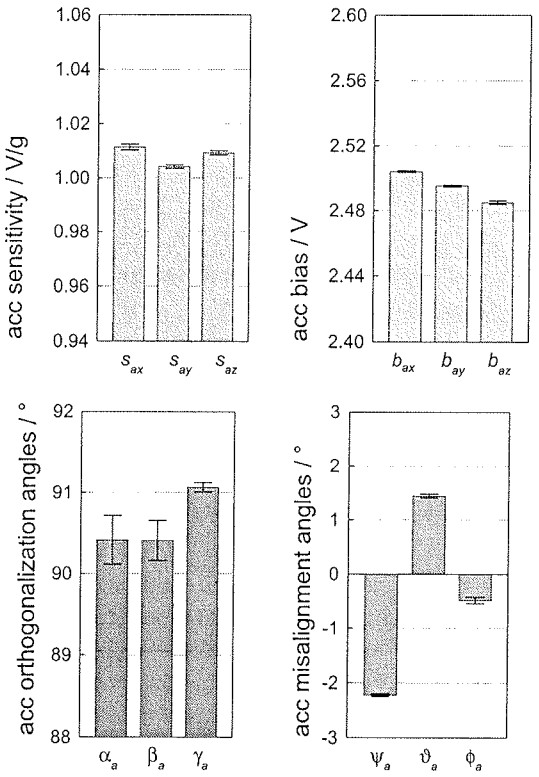

Fig. 4: Determined calibration parameters of the accelerometer triplet.

7. Conclusion

Complete procedure for the in-field calibration and alignment of the accelerometers, magnetic sensors and gyros was developed and successfully applied to the developed modular 6 DOF MIMU. With a view to simplify the sensor description an unified sensor model was used to describe the accelerometer, gyro and magnetic sensors triplets. The model considers the sensors' electrical characteristics as well as the mechanical effects of assembling the sensors into sensor triplets and enclosing them into the MIMU casing. Several calibration series were done at the room tem-

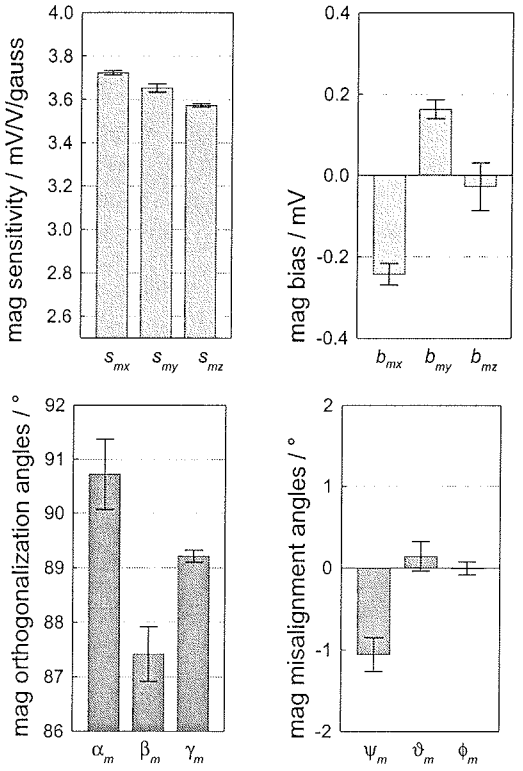

Fig. 5: Determined calibration parameters of the magnetic sensor triplet.

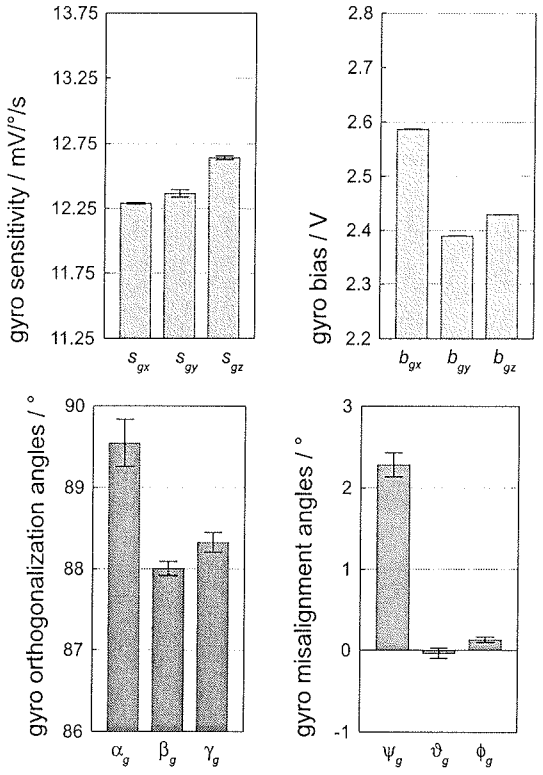

Fig. 6: Determined calibration parameters of the gyro triplet.

perature and they demonstrate the accuracy and stability of the calibration procedure.

8. Acknowledgement

The authors wish to thank Damir Franetič for helpful discussions.

9. References

/1/ http://www.analog.com

/2/ http://www.freescale.com

/3/ http://www.magneticsensors.com

/4/ S. K. Hong, Fuzzy logic based closed-loop strapdown attitude system for unmanned aerial vehicle (UAV), Sens. Actuat. A, 107 (2003) 109-118.

/5/ J. Wendel, et. al., An integrated GPS/MEMS-IMU navigation system for an autonomous helicopter, Aerospace Science and Technology, 10 (2006) 527-533

/6/ H. J. Luinge, P. H. Veltink, Inclination Measurement of Human Movement Using a 3-D Accelerometer With Autocalibration, IEEE Trans. neural syst. rehabil. eng., 12 (2004) 112-121

/7/ M. Zaoui, et. al., A 6 D.O.F. Opto-Inertial Tracker for Virtual Reality Experiments in Microgravity, Acta Astronautica, 49 (2001) 451-462

/8/ R. Kamnik, S. Stegel, M. Munih, Design and Calibration of Three-Axial Inertial Motion Sensor, Proc. of 12th International Power Electronics and Motion Control Conference, Portorož, Slovenia, Aug. 30 - Sep. 1, 2006, pp. 2031-2036

/9/ D. Jurman, M. Jankovec, B. Glažar, M. Topič, Development of modular inertial measurement unit, Proc. of 41st International Conference on Microelectronics, Devices and Materials and the Workshop on Green electronics, Ribno, Slovenia, Sep. 14-16, 2005, pp. 139-144

/10/ R. Zhu, Z. Zhou, Calibration of three-dimensional integrated sensors for improved system accuracy, Sens. Actuat. A, 127 (2006) 340-344

/11/ G. Tomšič, Osnovni pojmi funkcionalne analize, Fakulteta za elektrotehniko in računalništvo, Ljubljana, 2003, pp. 66-67

/12/ I. Skog, P. Händel, Calibration of a Mems Inertial Measurement Unit, Proc. of XVIII IMEKO World Congress, Metrology for a Sustainable Development, Rio de Janeiro, Brazil, Sep. 17-22, 2006

/13/ N. Olsen, et. al., Calibration of the Oersted vector magnetometer, Earth Planets Space, 55 (2003) 11-18

/14/ J. Včelak, P. Ripka, J. Kubik, A. Platil, P. Kašpar, AMR navigation systems and methods of their calibrations, Sens. Actuat. A, 123-124 (2005) 122-128

/15/ F. Ferraris, U. Grimaldi, M.Parvis, Procedure for Effortless In-Field Calibration of Three-Axis Rate Gyros and Accelerometers, Sens. Mater., 7 (1995) 311330

David Jurman, univ. dipl. ing. el.
Dr. Marko Jankovec, univ. dipl. ing. el.
Asst. Prof. Dr. Roman Kamnik, univ. dipl. ing. el.
Prof. Dr. Marko Topič, univ. dipl. ing. el.

University of Ljubljana,
Faculty of Electrical Engineering
Laboratory of Photovoltaics and Optoelectronics
Laboratory of Robotics and Biomedical Engineering
Tržaška cesta 25, SI-1000 Ljubljana, Slovenia
Tel.: +386 (0)1 4768 321; Fax: +386 (0)1 4264 630
E-mail: david.jurman@fe.uni-lj.si

Prispelo (Arrived): 23.03.2007 *Sprejeto (Accepted):* 15.06.2007

MERILNIK DIFUZNEGA SEVANJA SONCA

Ž. Gorup, N. Basarič

Univerza v Ljubljani, Fakulteta za elektrotehniko, Ljubljana, Slovenia

Kjučne besede: difuzno sevanje sonca, merjenje sončnega sevanja, sistemi za sledenje sonca, sistemi za zajemanje podatkov, senzorji svetlobe.

Izvleček: V pričujočem delu je opisana naprava za merjenje difuznega sevanja sonca, ki ima nekatere pomembne dopolnitve obstoječih merilnikov. Zgrajena je iz standardnih mehanskih, elektronskih in programskih komponent, kar bistveno znižuje ceno naprave, obenem pa povečuje njeno fleksibilnost in uporabnost. Merilna naprava obsega lokalno enoto in nadzorni računalnik. Lokalna enota ima mehansko konstrukcijo za sledenje sonca, piranometer in kontrolni modul za lokalni nadzor delovanja, ter omogoča upravljanje pretoka podatkov in komuniciranje z nadzornim računalnikom. Difuzno sevanje sonca meri piranometer, katerega senzor se stalno nahaja v dinamični senci senčne krogle. V senčni krogli je tudi senzor direktnega vpada sončnih žarkov. Ta senzor ima dve funkciji: preverjanje vpada direktnih žarkov in meritev trajanja oblačnosti. Za izboljšanje točnosti meritve je bilo dodano začetno pozicioniranje merilne naprave z elektronskim kompasom. Nadzor delovanja lokalne enote izvaja mikropretvornik, ki deluje obenem kot sistem za zajemanje podatkov. Poleg analogno-digitalne (A/D) pretvorbe senzorskih signalov predprocesira podatke in jih nato posreduje nadzornemu računalniku. Virtualni instrument (VI) na nadzornem računalniku omogoča procesiranje, prikaz, shranjevanje in prenos podatkov. Na modularno organiziranem VI izberemo parametre prikaza meritev: vzorčevalni čas, začetni čas, končni čas, filterske funkcije (nizko ali pasovno sito). Poleg formatov in urejanja podatkov lahko v VI izbiramo matematične transformacije in statistične izračune: kumulativno sevanje v določenem časovnem obdobju (integral), minimum in maksimum sevanja za podano časovno obdobje, histogram sevanja in statistične parametre. VI ponuja izbiro dveh oblik grafičnih prikazov: tračni časovni diagram in graf. Za prenos podatkov med lokalno enoto in nadzornim računalnikom služi standardna serijska komunikacije (RS-232) po žičnem ali brezžičnem mediju.

Diffuse solar radiation measuring instrument

Key words: diffuse solar radiation, solar radiation measurements, solar tracking systems, data acquisition systems, solar sensors.

Abstract: Measurements of diffuse solar radiation are normally done by pyranometer with a shadowing element to cover the direct solar beam. The present paper describes an apparatus with some important improvements to existing ones: a shadowing ball (sphere) with a direct beam detector, automatic positioning with electronic compass, local data acquisition system with microconverter, and virtual instrumentation. The measuring system is composed of a local unit and a supervisory computer. The local unit contains a mechanical construction of a solar tracking system, a measuring pyranometer and a control unit with a microconverter. It performs control, data management and data communication with a supervisory system. The modification from the conventional shadowing pyranometer comprises three steps: firstly, the shadowing ball combined with direct solar beam sensor is designed. The usual shadow-band elevation mode pyranometer is replaced with an azimuth-elevation tracking mode instrument. A microconverter acts as standard microcontroller and a data acquisition system simultaneously. Secondly, an automatic positioning system to align the system to the direction north-south is used. This facilitates and accelerates the mounting procedure and also increases the measuring precision. Thirdly, a virtual instrument (VI) is built in the main control computer system. It acts as a control software for data acquisition, data processing, presentation and storage. The VI is time efficient, easy to manage and adapted to work at different outdoor locations.

In our design of shadowing the direct light, the shadowing ball is mounted on the top of a thin arc. Unlike a shadow disc, the shadow ball alignment on the arc is not complicated and time consuming. Direct beam detector is an autonomous unit supervising the right position of the ball and to survey the time of cloudiness. It is functioning on the differential principle of two pairs of the light sensors, with output signals which are conditioned and converted into digital form. Local microconverter is capable of making a corresponding response to sensor's imbalance. A proper positioning of the measuring system is achieved with an electronic compass. It is perfectly suited to outdoor area applications and can be used for quick changes of measuring locations. If properly mounted, the electronic compass and solar tracker system can operate continuously in a loop. The orientation of the system versus north is examined prior the start on the initial position.

The purpose of tracking is to retain the solar shadow on the sensor's surface of the pyranometer. Solar tracking is achieved by two perpendicularly mounted stepping motors. The azimuth and elevation tracking follow the calculation of the solar position over the solar day. Steps are provided by sending single digit signals for each step into I/O digital bus. Steps are timed through software of the real time clock (RTC).

A supervisory computer contains a LabVIEW programming environment where virtual instrument (VI) is running. A VI for diffuse solar radiation measuring encloses some important functions: data acquisition, data processing, data visualization, and data storage. There are some main advantages of using virtual instrumentation. When comparing to the use of text oriented languages it ensures shorter time to build up program application, it provides user-friendly graphical interface, easy changes of program functions, very extensive signal analysis functions, and standard data communications channels.

1 Uvod

Ko svetloba potuje skozi atmosfero, se del sevanja absorbira, del sipa in del odbija. Celotno sevanje, ki ne zajema direktnih sončnih žarkov je difuzno sevanje sonca. Vsota direktnega in difuznega sevanja je globalno sevanje. Shematsko so različne komponente sončnega sevanja prikazane na sliki 1.

Komponento difuznega sevanja (*D*) lahko tudi izračunamo, če poznamo ostali dve komponenti: direktno (*B*) in globalno (*G*) sevanje ter kot (*i*), ki ga oklepa trenutna lega sonca z vertikalo na ravnino senzorja. Enačba, ki po kosinusnem zakonu povezuje vse tri veličine, je

$$G = B \cdot \cos(i) + D \qquad (1)$$

Različni atmosferski pogoji lahko zmanjšajo direktno sevanje za 10%, če je dan jasen in suh pa vse do 100%, če je

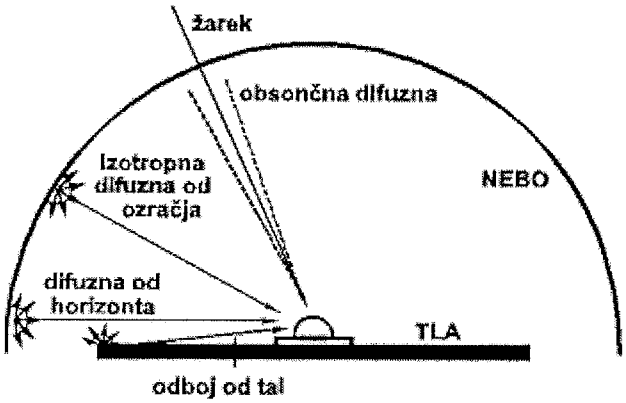

Slika 1: Komponenti sončnega sevanja: direktno in difuzno sevanje.

vreme vlažno in oblačno.

Podatki o meritvah difuznega sevanja sonca so pomembni za različna področja. Difuzno sevanje je bistven element pri načrtovanju ploščatih kolektorjev /1/. Podatke potrebujejo tudi arhitekti, ker je to vir dnevne svetlobe na mestih, ki nimajo direktno vidnega sonca (bloki, spodnja nadstropja stolpnic, stopnišča, kleti, itd.). Velikost difuzne komponente sončnega sevanja zanima agronome in botanike, ker jim podaja bistven vir energije biosfere. Difuzna svetloba vpliva tudi na nekatere človeške sposobnosti: vidljivost, razpoznavnost barv in vozne sposobnosti človeka v prometu, itd. Področja, kjer uporabljajo podatke o difuznem sevanju sonca, so: agronomija (fotosinteza), arhitektura (naravna svetloba bivalnih prostorov), astronomija (spreminjanje izhodnega sevanja sonca), biologija, fotobiologija (svetloba in življenje), fotovoltaika za direktno pretvorbo sončne energije v električno, hidrologija (izhlapevanje in izparevanje vode), klimatologija (klimatske spremembe na osnovi energijskega ravnotežja), meteorologija (numerično predvidevanje in napovedovanje vremena), oceanografija, pasivna solarna energija za osvetlitev in segrevanje bivalnih prostorov, promet in transport (naravna osvetljenost, upravljanje vozil in plovil), solarna termična energija (proizvodnja pare za pogon turbin v termoelektrarnah), solarne tehnologije goriv za pretvarjanje biomase (rastline, pridelki in les) v goriva in vzporedne produkte, solarno gretje za segrevanje vode (industrija in gospodinjstva), solarno razkuževanje in uničevanje nevarnih odpadkov s koncentrirano sončno svetlobo, tehnične vede o materialih (degradacija materialov), zdravje in medicina (vpliv sevanja na kožo).

Teoretično vrednost difuznega sevanja sonca lahko izračunamo na osnovi indeksa čistosti (clearness index) s pomočjo empiričnih enačb, ki so jih zapisali Liu in Jordan /2/ ter Klein /3/. Za izračun difuznega sevanja sonca je bil zgrajen model, iz katerega je nastal računalniški program AML /4/. Osnova za delovanje programa je model, opisan v delu Kumarja /5/. Program je kompakten in hiter. Omogoča pa izračun sevanja za najmanj en cel dan in ne dopušča urne ali manjše delitve.

Difuzno sevanje sonca merimo z zasenčenimi piranometri (shaded pyranometer), ki so opisani v delih številnih avtorjev /5/ - /9/. Te naprave se razlikujejo med seboj po obliki in namestitvi senčnika (zaslonke), ki preprečuje direktnim sončnim žarkom dostop do senzorja piranometra. Glavne izvedbe elementov za senčenje so: senčni obroč, senčni pas, disk, polkrogla in krogla. Senčni pas je lahko večji del obroča ali pa samo trakasti lok krožne oblike /10/. Največkrat se difuzno sončno sevanje meri s piranometri s senčnim obročem ali senčnim pasom (shadow-ring, shadow-band pyranometer). Piranometri s senčnim obročem ali pasom predstavljajo ceneno in enostavno rešitev, kjer je le ena mehanska nastavitev. Nastavitev senčnega elementa je dnevna ali nekajdnevna. Po točni geografski orientaciji instrumenta (smer sever-jug) je potrebna nastavitev obroča v položaj, pri katerem pade senca obroča na senzor piranometra v treh točkah: ob sončnem vzhodu, opoldan in ob sončnem zahodu. Prava lega je dosežena s spreminjanjem nagiba obroča glede na horizontalno ravnino (elevacija). Pri tem načinu merjenja je potrebna korekcija, ker neaktivni del obroča pokrije del površine prostora, ki bi sicer prispeval difuzno svetlobo in povečal izmerjeno vrednost.

Piranometer s senčnim diskom je rešitev, ki v pretežni meri izloča sistematsko napako senčnega obroča. Seveda je ta izvedba tehnično bolj zahtevna in tudi precej dražja /11/. Zahteva namreč elektromehanski sistem za sledenje sonca (enoosni ali pa dvoosni) in ustrezno programsko opremo.

Na tržišču je le majhno število proizvajalcev standardnih merilnikov difuznega sevanja sonca. Naprave so izdelane v zelo majhnih serijah, zato je cena posameznega merilnika visoka. Prvenstveno so merilniki namenjeni za stacionarno uporabo v meteorologiji, kar zahteva mehanske, elektronske in programske prilagoditve pri raziskovalnem delu. Algoritmi delovanja standardnih merilnikov so nespremenljivi in uporabnik nima možnosti poseganja v elektronski in programski sistem delovanja. S tega vidika je izdelava cenejše in vsestransko uporabne izvedbe merilne naprave smiselna, posebno, ker omogoča uporabniku fleksibilno uporabo in upošteva zahteve in posebnosti raziskovalnega dela. Najpomembnejše zahteve, ki se pojavljajo pri raziskavah v zvezi s sončno energijo so: primerno kratek čas začetne nastavitve naprave zaradi pogostega spreminjanja geografskega položaja merilne točke, sočasno preverjanje oblačnosti na senzorju piranometra in senzorju direktnega vpada sončnih žarkov, brezžičen prenos podatkov iz lokalne enote na nadzorni računalnik ter spremenljiv nadzorni program v obliki virtualnega instrumenta. Naštete funkcije morajo biti izvedene s standardno elektronsko in mehansko opremo, ki je dosegljiva na tržišču in z majhnimi mehanskimi prilagoditvami. Nadzorni program v obliki virtualnega instrumenta mora omogočati obdelavo sprejetih podatkov in spreminjanje nastavitev obdelave, konfiguriranje komunikacije, izdelavo dokumentacije in različne grafične prikaze.

2 Piranometer s senčno kroglo

Piranometer je namenjen merjenju globalnega in difuznega sevanja. Za merjenje difuznega sevanja mora biti senzor piranometra v senci. Piranometer s senčno kroglo (shadow ball, sphere) je nadgradnja naprav s senčnim diskom ali senčnim obročem. Ogledali si bomo zgrajeni prototip in delovanje svetlobnega senzorja s celotno konstrukcijo, ki omogoča kontinuirano senčenje senzorske površine v dvoosnem koordinatnem sistemu. V konstrukciji je poleg senčne krogle tudi nadzorni senzorski element, ki preverja direktni vpad sončnega sevanja. Isti element daje tudi podatek o zakritju sonca z oblakom. Za pravilno in usklajeno delovanje sledilnika sonca je potrebno točno začetno pozicioniranje v smeri sever-jug, kar je pri standardnih merilnikih potrebno izvesti ročno. To je dolgotrajen in natančen postopek, ki je bil pri izdelani napravi občutno skrajšan z uporabo elektronskega kompasa.

2.1 Zgradba naprave

Mehanska konstrukcija lokalne enote merilnika difuznega sevanja je prikazana na sliki 2. Konstrukcijo naprave sestavljata dve enoti: fiksna in gibljiva. Fiksna enota ima stabilno ohišje s podstavkom, v katerem je pritrjen glavni motor (koračni) za gibanje v horizontalni ravnini (po azimutu). V ohišju je tudi večina krmilne in merilne elektronike, razen senzorjev in vezij za prilagajanje signalov. Na osi glavnega motorja je pritrjena nosilna plošča, ki nosi lok s senčno kroglo, motor za pomik loka, piranometer in povezovalne elemente. Poleg naštetih glavnih delov ima naprava še elemente, ki služijo za povečanje zanesljivosti delovanja in dodatne funkcije (senzor direktnega vpada sončnega sevanja), začetno pozicioniranje in določitev izhodišča (elementi za pritrditev laserske tehtnice in elektronskega kompasa) in zaščito (varnostna končna stikala).

Piranometer, ki je uporabljen v prototipu merilnika, je Kipp & Zonen Model CM 5/6. Ima primerne merilne lastnosti, ki ga uvrščajo med sekundarne standarde. Posebno pomembni lastnosti sta temperaturni koeficient in časovna stabilnost. Piranometer CM 5/6 ustreza specifikacijam za najboljši izmed treh razredov, kot so definirani v delu /12/.

2.2 Senčna krogla

Ena izmed bistvenih komponent merilne naprave je senčna krogla. Prostorsko gibanje senčne krogle upravlja mikrokontroler sledilnega sistema, ki je del lokalne enote. Pri uporabi senčne krogle je pomembno, da je senca, ki pada na senzor, malo večja od aktivne površine senzorja. Projekcija krogle na senzorsko ploskev je elipsa, katere manjša os je za varnostni rob večja od površine senzorja. Pri postavitvi krogle na nosilni lok je pomembna točna nastavitev senčila na sredino loka. Med sledenjem sonca je presečna ravnina senčne krogle vedno krog, ki ustvari senco na ravnini senzorja. Razmere so prikazane na sliki 3.

Na sliki 3 je prikazana projekcija sončnih žarkov na senzor v času, ko je elevacija manjša od 90°. Projekcija sence, ki

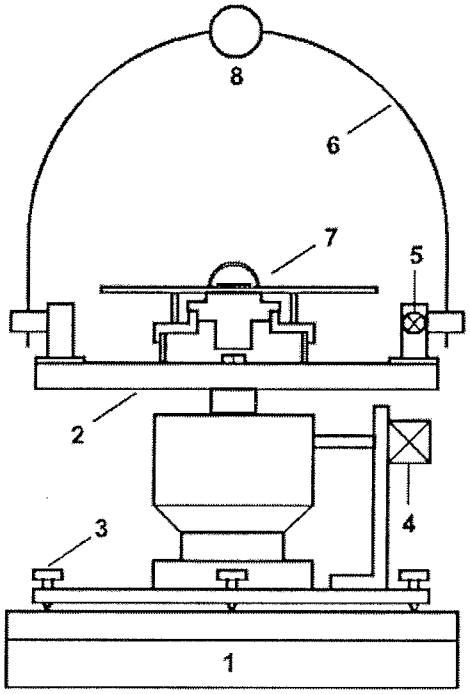

Legenda:
1 - ohišje
2 - nosilna plošča
3 - horizontalno justiranje
4 – koračni motor azimuta
5 – koračni motor deklinacije
6 – nosilni lok
7 – piranometer
8 – senčna krogla

Slika 2: Mehanska konstrukcija merilnika difuznega sevanja.

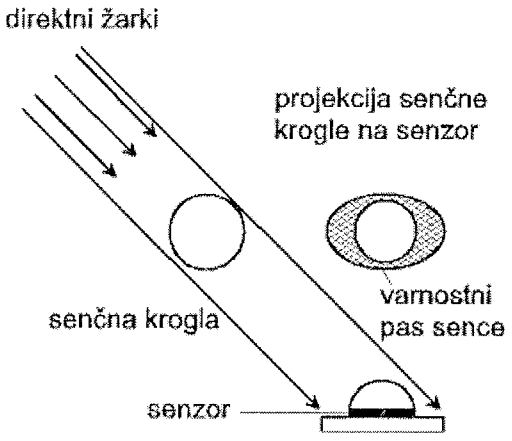

Slika 3: Projekcija direktnih sončnih žarkov prek senčne krogle na horizontalni senzor.

jo povzroča na senzorju senčna krogla, je krog le, ko je sonce točno v zenitu (opoldan) in so žarki pravokotni na ravnino senzorja. To je dosegljivo le v območju ekvatorialnega pasu (± 23,6° N in S). V vseh drugih legah ima senca obliko elipse. Elipsa ustvarja varnostni pas, ki obsega ploskev med zunanjim robom sence in površino senzorja piranometra. Za praktično uporabo je varnostni pas sence širok 5 mm. Ta pas tudi preprečuje večkratne odboje na prozorni zaščitni kupoli senzorja.

Središče senčne krogle je geometrijsko centrirano na nosilni lok in oddaljeno 50 cm od središča senzorja piranometra. Oddaljenost središča senzorja piranometra in središča senčne krogle ustreza standardni razdalji, ki znaša desetkratno vrednost premera senčne krogle /13/.

Le v posebnih primerih in pogojih delovanja (npr. meritve difuznega sevanja sonca med dežjem) je potrebna kompletna zunanja zaščita (stekleni ali plastični zvon). V senčni krogli je nameščen senzor direktnega vpada sončnih žarkov, ki stalno preverja položaj senčila.

2.3 Senzor direktnega vpada žarkov

Senzor direktnega vpada sončnih žarkov je dodatni senzor, ki ima dve funkciji: preverjanje natančne nastavitve pozicije sistema s senčno kroglo in meritev časa zakritja sonca, ko pade svetlobni tok za več kot 50%. Senzor direktnega vpada je izveden s krožno odprtino v cevi in ima štiri senzorske elemente na ravnem dnu cevi. Žarek vpada skozi odprtino na senzorske elemente, ki so prek vezja za prilagajanje signalov povezani z vhodno stopnjo elektronskega sistema za zajemanje podatkov (lokalni mikropretvornik). Zgradba senzorja je prikazana na sliki 4.

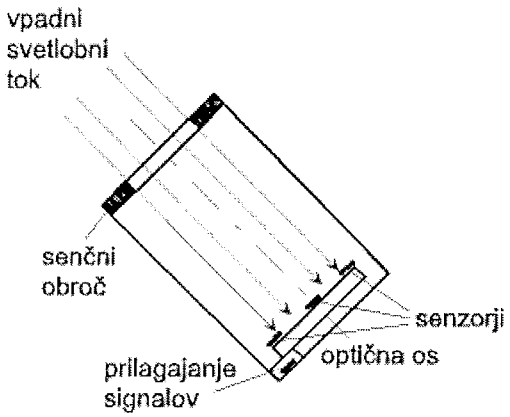

Slika 4: Senzor direktnega vpada sončnih žarkov.

Sistem deluje diferencialno: po dve in dve nasprotni senzorski diodi sta vezani na tokovno-napetostni (I/V) pretvornik, s katerega vodimo napetost na analogno-digitalni (A/D) pretvornik. Ko je osvetlitev nasproti ležečih diod enaka, sta toka diod enaka in senzorski sistem je v ravnotežju. Vsak izmik iz smeri direktnih sončnih žarkov predstavlja neravnotežje tokov senzorskih diod, kar ima za posledico reakcijo mikrokontrolerja in korekcijo pozicije. Sistem ima vgrajeno histerezo, da ne pride do nestabilnosti delovanja.

Ko svetlobna jakost na vseh štirih senzorskih diodah pade pod vnaprej določeno vrednost (50%), je oblačno. Mikrokontroler lokalne enote izvede primerjavo meritve osvetlitve senzorja direktnega vpada sončnih žarkov in meritve senzorja piranometra. Če sta izmerjeni spremembi usklajeni, sledi potrditev oblačnosti. Čas zakritja sonca v času sončnega dne se registrira posebej in je informacija o časovnem poteku oblačnosti nad območjem merjenja. Meritev trajanja oblačnosti ima seveda praktičen pomen le pri izvajanju meritev prek daljšega časovnega obdobja (več dni, tednov, mesecev).

2.4 Avtomatsko pozicioniranje in elektronski kompas

Merilni sistem zahteva za delovanje tridimenzionalno pozicioniranje, ki ga razdelimo na dva koraka. Najprej postavimo senzorsko nosilno ploščo v horizontalno lego, v drugem koraku pa usmerimo sistem proti severu (jugu). Za natančno horizontalno nastavitev uporabimo lasersko vodno tehtnico, ki omogoča točnost nastavitve ±0,5°. Naprava ima za to nastavitev na ohišju predvidene ustrezne justirne vijake. Usmeritev naprave v smer sever-jug je v prvem koraku le približna.

Klasično pozicioniranje naprave je zamudno, procedura pa natančna. Da bi se izognili subjektivnim napakam, smo instrument opremili z avtomatskim pozicionirnim sistemom. Jedro pozicionirnega sistema predstavlja elektronski kompas, ki je bil zgrajen z integriranim magnetnim senzorjem KMZ52 (Philips). Senzor je zelo občutljivo magnetno mostično vezje, ki deluje s pomočjo dveh tuljav v pravokotnem sistemu. Principielna blok shema vezja KMZ52 je prikazana na sliki 5.

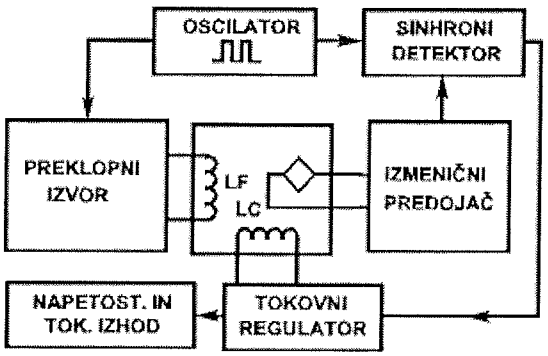

Slika 5: Principielna zgradba elektronskega kompasa.

V vezju je oscilator, ki napaja pravokotno nameščeni tuljavi LF in LC. V mostiču detektirani signal se nato ojači in filtrira, temu pa sledi sinhroni detektor. Izhodni analogni signal je sorazmeren odklonu usmerjenosti vezja glede na magnetno os Zemlje sever - jug. Točnost meritve je izboljšana z izvedbo kompenzacije začetne napake postavitve vezja (offset). Napaka v sledenju sonca je odvisna od točnosti usmerjenosti proti severu in ujetja pravokotnosti sistema. Pri ročni nastavitvi standardnih merilnikov je napaka pri postavitvi velika (do ±10°) in je bila z uporabo elektronskega kompasa na opisovani merilni napravi zmanjšana na ±1°.

Elektronski kompas je izveden kot integriran elektronski modul, ki je povezan s portom mikropretvornika. Procesor mikropretvornika spremlja lego sistema v skladu z izvajanjem nadzornega programa delovanja. Ker je elektronski kompas dvoosni, spremljamo lego vezja v ravninskem koordinatnem sistemu. Lega merilne naprave se preverja ob vsakem vklopu naprave in pri prehodu naprave v aktivni

način delovanja (po bujenju mikropretvornika). Procedura je del samotestiranja (self-test) merilnega sistema. Ob vsakem samotestiranju se izvede meritev položaja (geografske koordinate) in pomik senčnega elementa v izhodiščno lego.

3 Sledenje in izračun koordinat

3.1 Sledilni sistem

Naprave, katerih delovanje je vezano na sledenje sonca, uporabljajo samostojne ali pa integrirane sledilne sisteme. Merilnik difuznega sevanja sonca, ki ga opisujemo, uporablja integrirani sledilni sistem. Sistem sledenja temelji na koordinatnem sistemu, ki ima v svojem središču opazovalca v točki na površini Zemlje. Središče koordinatnega sistema je v središču senzorja piranometra. Koordinati (kota azimuta in elevacije), ki se nanašata na navidezno potovanje sonca po nebu od sončnega vzhoda do sončnega zahoda, določata položaj senčila /13/. Sledilni sistem mora zagotoviti, da pada projekcija senčne krogle stalno na senzor, kot je bilo prikazano na sliki 3.

3.2 Izračun koordinat

Za izračun gibanja sledilnika sonca je bila objavljena množica člankov, algoritem pa opisuje tudi knjiga /15/. Nekateri algoritmi so omejeni na določena časovna obdobja /16/, drugi poudarjajo natančnost (merilna negotovost ±0.0003° do leta 2004) /17/. Posebno pomembna je točnost nastavitve pri velikih kotih med normalo na površino senzorja in vpadnim sevanjem (kosinusni zakon).

Poleg izračuna lokalnih koordinat za gibanje sledilnega sistema je za avtonomijo sistema potrebno tudi vsakodnevno določanje sončnega dne. Sončni dan vsebuje izračun sončnega vzhoda in zahoda ter njuno korekcijo glede na izbrano točko opazovanja. Za izračune smo uporabili empirične izraze, ki jih vsebuje delo Harrigana in Stineja /18/ in zagotavljajo natančnost nastavitve obeh koordinatnih osi pod ± 1°, kar je ustrezno glede na mehansko izvedbo naprave in korak koračnih motorjev.

Trenutni položaj senčila za senčenje direktnega sončnega sevanja v lokalnem koordinatnem sistemu je določen z dvema kotoma: azimutom in elevacijo. Koordinatni sistem za izračun položaja senčila je prikazan na sliki 6.

Elevacija je kot med horizontalno ravnino v opazovani točki (središče senzorja) in smerjo sončnega žarka. Imenovan je tudi višina opazovanega objekta. Elevacija obsega kote od 0° do 90°.

Azimut je v sledilnem sistemu kot, ki ga tvori projekcija direktnega sončnega žarka na horizontalno ravnino z vektorjem med točko opazovanja (senzorjem) in pravim severnim (ali južnim) polom. Pozitivna smer tega kota je v smeri urinega kazalca glede na severni pol, kot je prikazano na sliki 6. Azimut lahko obsega kote od 0° do 360°.

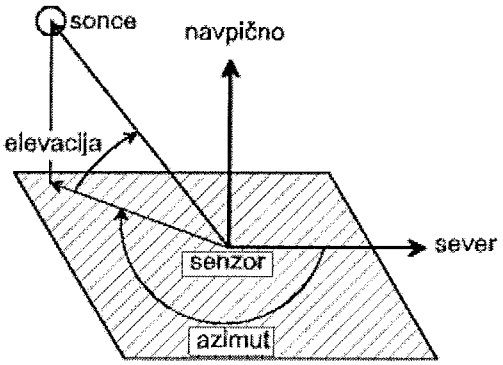

Slika 6: Koordinatni sistem za izračun položaja senčila

Elevacija in azimut se izračunavata stalno na osnovi ure realnega časa. Vsako sekundo se izračuna položaj središča senčne krogle v polarnem koordinatnem sistemu. Ker je razdalja središča senčne krogle glede na središče senzorja piranometra konstantna, se spreminjata samo dva kota: azimut in elevacija. Vsak izmed teh dveh kotov zavzame določeno število korakov koračnega motorja. Ob tem je potrebno upoštevati tudi prestavno razmerje reduktorja, ki je zaradi različnih motorjev in prenosov za vsako koordinatno os različno.

Sistem je v aktivnem stanju med sončnim vzhodom in zahodom. Oba časovna trenutka se izračunata, da se sistem zbudi iz spalnega načina ob sončnem vzhodu in gre v spalni način delovanja (sleep mode) po sončnem zahodu. Ob sončnem zahodu se sistem parkira (motor za pomik po azimutu zavzame položaj 0° - smer vzhod, motor za elevacijo pa 0° glede na horizontalno ravnino). V tem stanju naprava čaka na bujenje naslednjega dne.

4 Virtualni instrument nadzornega sistema

Virtualni instrument (VI) je program, ki deluje v grafičnem okolju. Napisan je v G-jeziku, ki namesto programskih stavkov izvaja programske funkcije v obliki grafičnih simbolov. VI ima čelno ploščo, blok diagrama in ikone (konektorja). Čelna plošča je uporabniški vmesnik, ki vsebuje kontrole in indikatorje. Za merilnik difuznega sevanja sonca je bil razvit VI, ki omogoča zajemanje podatkov, procesiranje, prikaz in shranjevanje.

Čelna plošča VI za merjenje difuznega sevanja sonca vsebuje kontrole in indikatorje za upravljanje podatkov. Upravljanje podatkov je razdeljeno na štiri enote: 1. zajemanje, 2. procesiranje, 3. prikaz in 4. shranjevanje. Za vsako enoto je izdelan posebni del uporabniškega vmesnika.

Zajemanje obsega vzpostavitev komunikacije med lokalno enoto in nadzornim računalnikom, prenos podatkov in začasno shranjevanje. Komunikacija je standardna serijska (RS-232), komunikacijski medij pa je fizični vodnik ali pa radijska zveza. Na čelni plošči so privzeti komunikacijski parametri (baudna hitrost, število podatkovnih bitov, par-

nost, število stop bitov), ki se lahko v meniju spreminjajo. Definiran je začetek in konec prenosa ali kontinuiran prenos do zaustavitve. Pred shranjevanjem podatkov v začasno datoteko se ime datoteke določi v menijskem oknu.

Procesiranje zajetih podatkov je lahko v realnem času za podatke, ki prihajajo, ali pa postprocesiranje, ko so že vsi podatki shranjeni v datoteki. V realnem času je procesiranje počasno, ker so vzorčevalni časi dolgi od 1 s do 1 ure. Običajno se procesirajo podatki, ki so v začasni datoteki. VI ponuja izbiro časovnega intervala opazovanja, meritve karakterističnih vrednosti časovne funkcije (minimum, maksimum, srednja vrednost, efektivna vrednost, največja strmina), kumulativno sevanje (določen integral) za določni dan in trajanje oblačnosti.

Prikaz podatkov je na XY grafu, ki je uporabljen kot tračni diagram za prihajajoče podatke (kontinuiran prenos po komunikacijskem kanalu) ali kot graf za postprocesiranje. Rešitev za tračni diagram je izvedena s posebnim virtualnim podinstrumentom (subVI). XY graf se lahko izbere samo za prikaz podatkov iz začasne datoteke, ker morajo biti podatki obeh koordinatnih osi na razpolago pred začetkom risanja. Za prikaz podatkov so na čelni plošči nastavitve, s katerimi uporabnik izbere časovni interval in načine filtriranja podatkov.

Shranjevanje podatkov je avtomatsko v začasno datoteko na disku nadzornega računalnika. Na čelni plošči se lahko izbira med tremi formati shranjevanja: ASCII, datalog in binarni. ASCII format je v VI privzet format, ker ga lahko neposredno pregledujemo in spreminjamo, zasede pa največ pomnilniškega prostora. Podatki se lahko filtrirajo in shranjujejo v kompaktni obliki. Po zaključku shranjevanja se datoteka avtomatsko zapre. Pri sledečih shranjevanjih je v VI na voljo možnost za dodajanje podatkov v že obstoječo datoteko.

5 Rezultati delovanja

Zgrajen je bil prototip merilnika difuznega sevanja sonca. Za sestavne dele so bili izbrani standardni materiali in moduli, ki so na tržišču. Za nadzorni sistem je bil uporabljen LabVIEW, ki je v zgrajeni napravi omogočal enostavnost preverjanja delovanja ter dodajanja in spreminjanja funkcij.

Začetna nastavitev koordinat je bila izvedena z elektronskim kompasom, ki je omogočil mnogo hitrejšo nastavitev, kot jo imajo drugi merilniki difuznega sevanja na tržišču.

Senca na senzorju je dobljena s premikajočo se kroglo. Krogla se nahaja na polkrožnem loku. Premik krogle po azimutu in elevaciji poganjata koračna motorja.

Tako kot pri drugih izvedbah merilnikov difuznega sevanja se je pojavil tudi v razvitem prototipu problem mrtvega hoda zobnikov med nosilcem pomične krogle in koračnima motorjema. Pri sledenju sonca se pojavlja mrtvi hod dvakrat: v začetnem položaju (ničelna lega), ko sistem ob sončnem vzhodu začenja sledenje in opoldan, ko se začne elevacija zmanjševati. Zaradi lastne teže se dopoldan mrtvi hod pojavi samo v izhodišču, nato pa na prenose deluje stalna sila teže loka in senčila. Ko gre senčilo prek ravnine lokalnega poldnevnika (opoldan), se pojavi mrtvi hod, ki ima obratno smer glede na silo teže nosilnega loka in senčila. Algoritem krmiljenja koračnih motorjev je zagotovil približevanje izračunani vrednosti položaja senčila vedno iz smeri, ki je nasprotna smeri sile teže. S tem je mrtvi hod zobniških prenosov izločen, nastavitev lege senčila pa traja le nekaj sekund.

Merilni sistem začne vsak dan sledenje sonca iz istega začetnega položaja: to je ničelna lega sistema. Nahaja se na elevaciji 0° in azimutu 90° (smer vzhod). Sistem se zjutraj iz te točke premakne, ko dobi podatek o sončnem vzhodu in se vanjo vrne zvečer, ko dobi podatek o sončnem zahodu. V ničelni legi sistem ostane prek noči (spalni način delovanja).

Za preizkus delovanja je bila uporabljena brezžična komunikacija za prenos podatkov. Komunikacija je radiofrekvenčna (RF), serijska, kompatibilna z RS-232 standardom in deluje na ISM področju 433 MHz.

Primer izmerjenega časovnega poteka difuznega sevanja v obdobju enega sončnega dne (12 ur za datum 14 marec 2006 na lokaciji 46° 03' N, 13° 14' E) je prikazan na sliki 7.

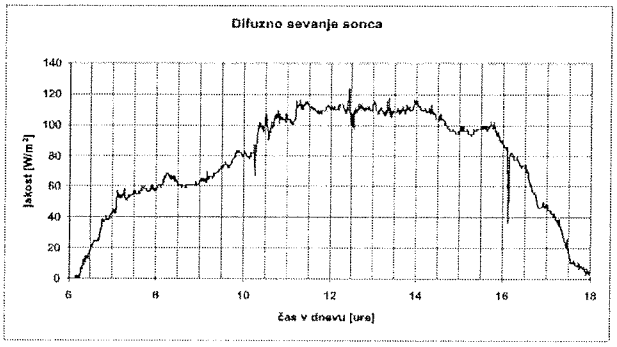

Slika 7: Časovni potek difuznega sevanja sonca.

Izmerjeni rezultati difuznega sevanja sonca, ki jih prikazuje slika 7, so bili prenešeni iz VI v preglednico (Excel).

Pri meritvi obstaja tudi sistematska napaka zaradi pokritja dela zgornjega polprostora koordinatnega sistema z mehanskim nosilcem in senčno kroglo. Velikost te napake smo izračunali in je v velikostnem razredu pod 1% merjene vrednosti.

Nadzoni program prototipa merilne naprave je VI, ki poteka na nadzornem računalniku kot grafični program v LabVIEW okolju. VI je sestavljen iz podinstrumentov (subVI), kjer so realizirane posamezne podprogramske funkcije. V oknu čelne plošče je prikazana izbira komunikacijskih parametrov za sprejem podatkov prek standardnega serijskega kanala (RS-232) in način prikaza podatkov. Podatki se lahko pregledujejo tako kot prihajajo v tračnem diagramu (v realnem času). Po zapisu v datoteko se lahko pregledujejo v grafu po končanem zajemanju (v virtualnem času). V oknu čelne plošče so na voljo še drugi kriteriji prikaza in izračuni: minimalna in maksimalna vrednost meritve, kumulativno difuzno sevanje in kumulativni čas zakritja z ob-

laki za določen časovni interval, čas najhitrejše spremembe sevanja. Za prenos podatkov v preglednice so na voljo nekateri standardni formati: ASCII, Excel, itd.

6 Sklep

Meritev difuznega sevanja sonca predstavlja tehnični problem, ki ga proizvajalci merilne opreme, kot tudi uporabniki rešujejo na različne načine. Najenostavnejša je seveda rešitev z vrhunsko merilno opremo, ki pa predstavlja možnost le za najbogatejše. Vendar ni niti taka oprema brez pomankljivosti in ne zagotavlja absolutne točnosti. V kolikor razpolagamo z vitalnimi deli merilnega sistema, lahko izvedemo zelo kvalitetne meritve tudi z mnogo cenejšo napravo, ki vsebuje novosti in prednosti pred podobnimi merilniki in je primerna za uporabo tudi pri raziskovalnem delu.

Merjenje difuzne svetlobe je izvedeno s piranometrom, ki je zasenčen s senčno kroglo. Gibanje senčne krogle določa algoritem mikropretvornika. Ustvarjanje sence na senzorju piranometra je primarna naloga senčne krogle. Obenem pa senčna krogla opravlja tudi meritev časa oblačnosti, ker je v njej integriran senzor direktnega vpada sončnih žarkov.

Elektronski kompas z mikropretvornikom postavlja napravo v družino avtomatskih ali inteligentnih senzorjev. Uporabniku prihrani precej truda in poizkusov točne orientacije glede na geografske smeri neba. Izvedba elektronskega kompasa je prilagojena mikroprocesorsko zasnovanemu sistemu in daje dober rezultat glede na razmeroma majhen finančni vložek, ki je za izdelavo vezja potreben.

Nadzorni sistem je namenjen upravljanju podatkov (data management). Izdelan je kot virtualni instrument (VI) s pripadajočimi virtualnimi podinstrumenti. VI ima grafični vmesnik za postavitev potrebnih upravljalskih funkcij in dostop do podatkov v numerični in grafični obliki. Program, ki je sestavljen v okolju LabVIEW, je fleksibilen in omogoča hitre spremembe konfiguracije sistema in procesiranja podatkov. VI omogoča tudi shranjevanje podatkov, preverjanje njihove konsistence glede na konfiguracijo in zahteve uporabnika in posredovanje podatkov drugim sistemom po standardnih komunikacijskih poteh.

Merilnik difuznega sevanja sonca je bil izdelan iz standardnih mehanskih in elektronskih komponent, ki so dosegljive na tržišču. Mehanske komponente (prenosi, reduktor, nosilna plošča, lok, senčnik) so bile prilagojene in povezane v funkcionalno celoto. Uporabljene elektronske komponente so velikoserijska integrirana vezja in pasivne komponente s poznanimi karakteristikami. Za elektroniko lokalne enote je bila uporabljena nezahtevna tehnologija tiskanih vezij (dvoplastna) in povezovalni elementi za zunanjo uporabo.

7 Reference

/1/ Veeran PK, Kumar S. Diffuse radiation on a horizontal surface at Madras. *Renew Energy*, 1993, **3** (8): 931-4

/2/ Liu Yb, Jordan RC. The interrelationship and characteristic distribution of direct, diffuse and total radiation. *Solar Energy*, 1971, **13**: 289-90

/3/ Klein SA. Calculation of monthly average insolations on tilted surfaces, *Solar Energy*, **19**, 1977: 325-9

/4/ AML - program diffuse.aml: http://www.wsl.ch/staff/niklaus.zimmermann/programs/aml1_4.html

/5/ Kumar, L., Skidmore, A.K. and Knowles, E., Modelling topographic variation in solar radiation in a GIS environment. *Int. Journal for Geographical Information Science*, 1997, **11** (5): 475-497.

/6/ M. P. Thekaekara, *Solar radiation measurement - Techniques and instrumentation*, Solar Energy, vol. 18, no. 4, 1976, p. 309-325.

/7/ F. Kesten, *Measurement and analysis of solar radiation data*, Performance of solar energy converters: Thermal collectors and photovoltaic cells, Lectures of the Course, Ispra, Italy, November 11-18, 1981, Dordrecht, D. Reidel Publishing Co., 1983, p. 1-64.

/8/ J. R. Hickey, *Solar radiation measuring instruments - Terrestrial and extra-terrestrial*, Proc. Seminar Optics in solar energy utilization, San Diego, Aug. 21, Palos Verdes Estates, Calif., Society of Photo-Optical Instrumentation Engineers, 1975, p. 53-61.

/9/ K. L. Coulson, Y. Howell, Solar radiation instruments, Sunworld, vol. 4, no. 3, 1980, p. 87-94.

/10/ E. C. Kern, Jr., Rotating Shadowband Radiometer, Irradiance, USA: www.irradiance.com

/11/ M. Ceschia, Z. Gorup, E. Toppano: A shadow disc instrument for measuring diffuse solar radiation, Congrsso SIF, Napoli, 1988

/12/ *Guide to meteorological Instruments and Methods of Observation*, 7th Ed., World Meteorological, 2006, http://www.wmo.ch/web/www/IMOP/publications/CIMO-Guide/Draft%207th%20edition/-Part1-Ch07Final_Corr_LSP.pdf

/13/ Instrument Descriptions - http://www.cmdl.noaa.gov/star/bodyframe.html

/14/ S. Lakeou, E. Ososanya, B. Latigo, W. Mahmoud, G. Karanja, W. Oshumare: Design of a Low-cost Solar Tracking Photo-voltaic (PV) Module and Wind Turbine Combination System, 21st European Photovoltaic Solar Energy Conference, 4-8 September 2006, Dresden, Germany, http://www.udc.edu/cere/5BV.1.39.pdf

/15/ Meeus, J., 1998. Astronomical Algorithms, second ed. Willmann-Bell, Inc., Richmond, USA.

/16/ Michalsky, J.J., 1988. The astronomical Almanac's algorithm for approximate solar position (1950-2050), *J. Solar Energy*, **40** (3): 227-235)

/17/ Ibrahim Reda, Afshin Andreas, Solar position algorithm for solar radiation applications, *Solar Energy*, **76** (2004): 577-589

/18/ R. W. Harrigan, W. B. Stine, Solar Energy Fundamentals and Design with Computer Applications, John Wiley & Sons Inc., New York, 1985

Doc. dr. Žarko Gorup
Fakulteta za elektrotehniko, Univerza v Ljubljani
Tržaška 25, SI-1000 Ljubljana, Slovenija
E-mail: zarko.gorup@fe.uni-lj.si
tel +386 1 4768 325; fax +386 1 4768 725

V. pred. mag. Niko Basarič
Fakulteta za elektrotehniko, Univerza v Ljubljani
Tržaška 25, SI-1000 Ljubljana, Slovenija
E-mail: niko.basaric@fe.uni-lj.si
tel +386 1 4768 331;

Prispelo (Arrived): 18.01.2007 *Sprejeto (Accepted):* 15.06.2007

DEVELOPMENT AND CHARACTERIZATION OF A LOW-FREQUENCY NOISE MEASUREMENT SYSTEM FOR OPTOELECTRONIC DEVICES

Marko Jankovec, Marko Topič

Faculty of Electrical Engineering, University of Ljubljana, Ljubljana, Slovenia

Key words: noise measurement, FFT spectrum analyzer, transconductance amplifier, 1/*f* noise

Abstract: A noise spectral density measurement system for low-frequency current noise was built and thoroughly characterized from dynamic and noise point of view. The system uses the SR570 transconductance amplifier and the SR780 FFT spectrum analyzer. The built in battery power supply in the SR570 together with an effective double shielding arrangement enables good low frequency interference protection in noisy environments. Results of dynamic and noise analyses and a resulting comprehensive noise model of the SR570 are presented. Besides other noise parameters also 1/*f* noise components of noise sources in the SR570 are identified. Further, the influence of DUT impedance to the overall system noise properties is shown. The noise measurement system performance utilizing the developed noise model is demonstrated by the low-frequency noise measurement of a-Si:H *pin* diode.

Razvoj in karakterizacija nizkofrekvenčnega šumnega merilnega sistema za optoelektronske elemente

Kjučne besede: šumne meritve, FFT spektralni analizator, transkonduktančni ojačevalnik, 1/*f* šum

Izvleček: Zgradili smo šumni merilni sistem za meritev gostote močnostnega spektra tokovnega šuma pri nizkih frekvencah in ga natančno okarakterizirali iz dinamičnega in šumnega vidika. V merilnem sistemu sta uporabljena transkonduktančni ojačevalnik SR570 in FFT spektralni analizator SR780. Vgrajeno baterijsko napajanje v SR570 skupaj z učinkovitim dvojnim oklopom omogoča visoko odpornost proti nizkofrekvenčnim motnjam v šumnem laboratorijskem okolju. V članku predstavljamo rezultate dinamične in šumne analize merilnega sistema ter celotnega šumnega modela ojačevalnika SR570. Poleg kataloških šumnih parametrov smo ovrednotili tudi 1/*f* spektralne komponente šumnih virov ojačevalnika SR570. Nadalje je pokazan vpliv impedance merjenca na šumne lastnosti celotnega merilnega sistema. Delovanje šumnega merilnega sistema in uporabo šumnega modela smo prikazali na primeru meritve nizkofrekvenčnega šuma a-Si:H *pin* diode.

1. Introduction

Noise performance of any kind of photodetection system is basically determined by noise of photodetector and noise of readout electronics /1/. The upper limit of signal-to-noise ratio and dynamic range of the whole system are initially determined by the noise of the detector. In the case of a photodiode, the useful signal is usually superimposed by a random component, which is a consequence of concentration and mobility fluctuations of free charge carriers. This random signal can be expressed as a superposition of shot, 1/*f* (flicker) and thermal noise sources /2/. While the physical backgrounds of thermal and shot noise are well known, the origin of 1/*f* noise is still a matter of research /3/.

If a photodetector operates in a charge storage mode, when its (DC) current signal is integrated in a storage capacitance and read out after certain integration time, the 1/*f* noise becomes important /4/. Additionally, the 1/*f* noise investigation of low-quality material devices, such as a-Si:H TFTs or *pin* diodes, gives deeper insight into the device physics providing potential for improvements /5, 6/. Since the 1/*f* noise of a photodetector is an important parameter, especially at low radiation intensities and high speed readout requirements, its quantitative determination is necessary for device characterization and optimization of the readout electronics.

We have built-up a low frequency current noise spectral density measurement setup for two-terminal devices, which is mainly intended for low-frequency noise spectral density measurements of optoelectronic detectors. Prior to any device characterization a comprehensive test of the measurement setup was performed since various internal and external noise sources contribute to the total system noise and have to be evaluated and separated from the signal that originates from the Device Under Test (DUT). Furthermore, the influence of the impedance of the DUT to the noise properties of the measurement system was investigated. Finally, the obtained noise model of the measurement system was applied for noise measurement of an α-Si:H *pin* diode.

2. Measurement system

The noise measurement setup is presented in fig. 1. It consists of a double shielded measurement box, a battery powered Low-Noise Amplifier (LNA) and a Fast-Fourier Transform (FFT) spectrum analyzer. Temperature of the

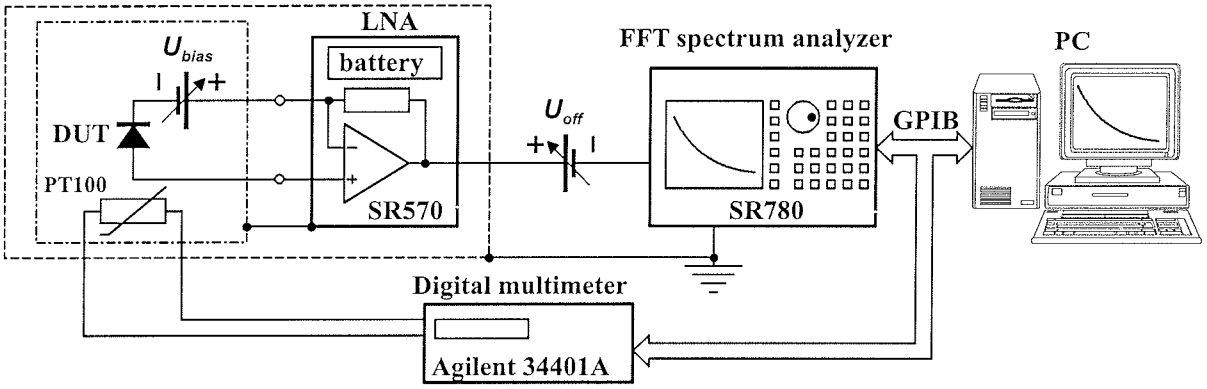

Fig. 1: Noise measurement setup with variable voltage bias (U_{bias}) and offset (U_{off}) sources, temperature monitoring and double shielding from external interference.

inner measurement box is monitored by a PT100 temperature sensor, whose resistance is acquired by an Agilent 34401A digital multimeter. Both digital instruments are controlled by personal computer (PC) via General Purpose Instrument Bus (GPIB).

Conventional spectrum analyzers which are based on a heterodyne principle have limited lower frequency range (arround 10 Hz) making them less suitable for $1/f$ noise measurement. On the contrary, FFT spectrum analyzers have fundamental upper frequency limit due to limited calculation capabilities, while their lower frequency limit is only determined by the available measurement time, since they can sample the signal over arbitrarily long period and perform the FFT transform to calculate the spectral density. For our system we chose the SR780 FFT spectrum analyzer made by Stanford Research System /7/. It features a wide range of frequency spans from 102.4 kHz down to 195.3 mHz with maximum resolution of 800 points thus enabling noise spectral density measurements resolution up to 244 mHz. Further, the built in 18-bit A/D converter together with low noise input amplifier stage offers high dynamic range useful for measuring low amplitude signal superimposed to higher DC bias.

The choice of LNA as a critical system component depends on the expected type of DUTs and the desired measurement quantities. Since the output of a photodetector is usually a current signal, we looked for a transconductance amplifier for current noise measurements. For its proper operation, the transconductance has to be lower than the DUT admittance, which might be a problem in the case of low resistive or high capacitive DUTs, due to input voltage noise amplification. Considering all these facts we chose SR570 /8/ as the most appropriate LNA. It features low input current and voltage noise, and its transconductance can be set from 1 mA/V down to 1 pA/V, where it uses one of two different input preamplifiers, each for its own sensitivity range. For extremely low signal measurements, the built in lead-acid rechargeable batteries for off-line powering minimize power-line interference noise problems. External interference with the connections of DUT and bias source at the input of the SR570 is suppressed by a careful coaxial cabling, which is additionally reduced by a high-permeability mumetal box. The mumetal box is together with the SR570 enclosed in a bigger aluminum box.

Although the SR570 is equipped with current offset and voltage bias sources that can be useful in some cases, it turned out that they generate too much additional noise to be useful for our design rules. Thus, we had to introduce two external variable voltage sources U_{bias} and U_{off} (Fig. 1) for biasing DUTs and for canceling a consecutive output voltage offset, respectively. Both are made of a sealed lead-acid battery and a variable wire wound resistor divider, which features the lowest intrinsic noise. The equivalent resistance of divider is approximately 500 Ω with negligible effect to the noise of the whole system. The chosen battery capacity is high enough to sustain a fixed DC voltage for 12 hours. All noise measurements were taken at room temperature in an air-conditioned room with well defined temperature stabilization (25 ± 0.5 °C).

3. Results

Prior to noise measurement of any DUT a detailed characterization of the measurement system has to be performed. Due to wide dynamic range of the SR780, the overall noise of the measurement system is determined solely by the LNA, which will be investigated further in detail. The simplified scheme of the transconductance amplifier SR570 is presented in fig. 2.

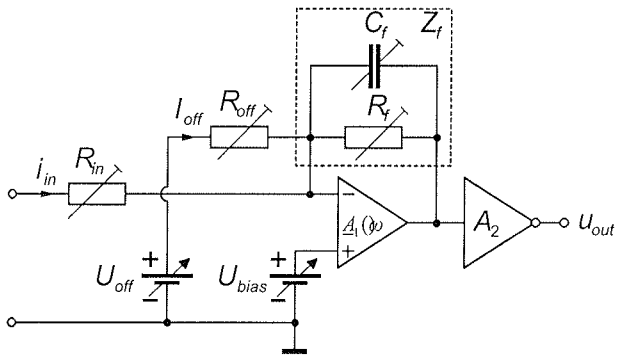

Fig. 2: The simplified scheme of a transconductance amplifier SR570.

It basically consists of an ultra low-noise operational amplifier with feedback resistance R_f. The value R_f is equal to the inverse value of the transconductance down to 100 pA/V for decade values, while below 100 pA/V the sensitivity is increased by a second stage voltage amplifier A_2. Although not desired in some cases, the added variable feedback capacitance can lower the bandwidth of preamplifier to compensate the voltage noise enhancement in the case of high capacitive input termination. For that reason an input resistance R_{in} is included, which is set according to the value of R_f in order to limit the voltage gain of the amplifier in the case of low impedance of the DUT.

3.1. Small signal model of SR570

Fig. 3 presents the small signal model of the amplifier. The feedback impedance $\underline{Z}_f$ (C_f | | R_f) is transformed to the input as a Miller impedance $\underline{Z}_{fmil}$ according to the open loop gain of the front stage $\underline{A}_1(\omega)$, which is modeled as a DC gain A_0 with two poles ω_1 and ω_2. For the second stage a constant voltage gain A_2 in the investigated frequency range is assumed. Thus the voltage drop on $\underline{Z}_{fmil}$ caused by the input current $\underline{I}_{in}$ is amplified by both gain stages $\underline{A}_1(\omega)$ and A_2 (Eq. 3).

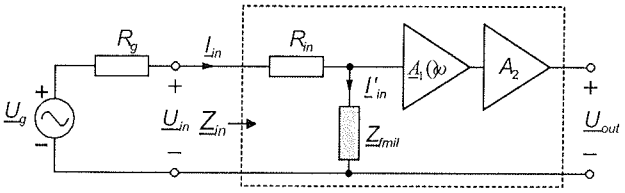

Fig. 3: The small signal model of the SR570 amplifier.

$$\underline{A}_1(\omega) = \frac{A_0}{(1 + j\omega/\omega_1)(1 + j\omega/\omega_2)} \tag{1}$$

$$\underline{Z}_{fmil}(\omega) = \frac{\underline{Z}_f}{1 + \underline{A}_1} = \frac{1}{1 + \underline{A}_1}\left(\frac{R_f}{1 + j\omega R_f C_f}\right) \tag{2}$$

$$\underline{U}_{out}(\omega) = \underline{A}_1 A_2 \underline{Z}_{fmil} \cdot \underline{I}_{in} \tag{3}$$

In order to determine small signal parameters of the amplifier, the internal and external transfer characteristics from DC to 100 kHz have been measured.

$$\underline{H}(\omega) = \frac{\underline{U}_{out}}{\underline{U}_{in}} = \underline{A}_1 A_2 \frac{\underline{Z}_{fmil}}{R_{in} + \underline{Z}_{fmil}}, \tag{4}$$

$$\underline{H}_{ext}(\omega) = \frac{\underline{U}_{out}}{\underline{U}_g} = \underline{A}_1 A_2 \frac{\underline{Z}_{fmil}}{R_g + R_{in} + \underline{Z}_{fmil}}. \tag{5}$$

By comparing the dynamic model output to the measured data (fig. 4 and fig. 5), we have obtained small signal parameters of the model, which are listed in table 1. The experimentally determined values are denoted in bold, all other are taken from the SR570 datasheet. The differences in A_0 and ω_1 values are due to the usage of two different input preamplifiers.

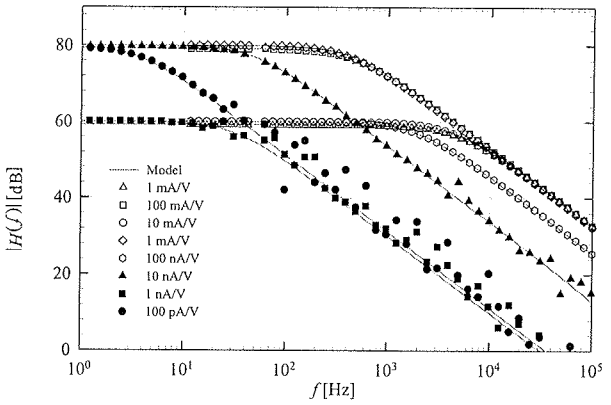

Fig. 4: Measured frequency characteristics of the SR570 voltage gain (symbols) at different sensitivities, compared with the small signal model results (lines).

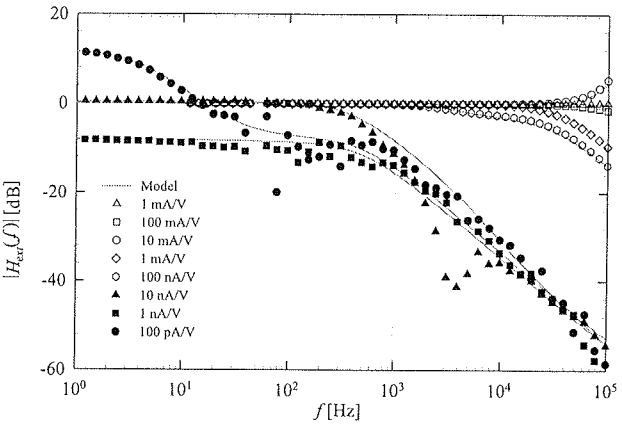

Fig. 5: Measured frequency characteristics of the SR570 external voltage gain (symbols) at different sensitivities, compared with the small signal model results (lines).

Table 1: Parameters of the SR570 small signal model at different transconductance settings.

Transconductance [A/V]	R_g [Ω]	R_f [Ω]	R_{in} [Ω]	B_{-3dB} [Hz]	C_f [pF]	A_0 [V/V]	$\omega_1/2\pi$ [Hz]	$\omega_2/2\pi$ [Hz]
10^{-3}	10^3	10^3	1	$1{\cdot}10^6$	**110**	$\mathbf{4{\cdot}10^6}$	**1.10**	$\mathbf{2{\cdot}10^5}$
10^{-4}	10^4	10^4	1	$5{\cdot}10^5$	**110**	$\mathbf{4{\cdot}10^6}$	**1.10**	$\mathbf{2{\cdot}10^5}$
10^{-5}	10^5	10^5	100	$2{\cdot}10^5$	**6.0**	$\mathbf{4{\cdot}10^6}$	**1.10**	$\mathbf{2{\cdot}10^5}$
10^{-6}	10^6	10^6	100	$2{\cdot}10^4$	**6.0**	$\mathbf{4{\cdot}10^6}$	**1.10**	$\mathbf{2{\cdot}10^5}$
10^{-7}	10^7	10^7	10^4	$2{\cdot}10^3$	**4.8**	$\mathbf{4{\cdot}10^6}$	**1.10**	$\mathbf{2{\cdot}10^5}$
10^{-8}	$9.6{\cdot}10^7$	10^8	10^4	200	**4.2**	$\mathbf{10^6}$	**0.55**	$\mathbf{2{\cdot}10^5}$
10^{-9}	$2.6{\cdot}10^9$	10^9	10^6	15	**4.2**	$\mathbf{10^6}$	**0.55**	$\mathbf{2{\cdot}10^5}$
10^{-10}	$2.6{\cdot}10^9$	10^{10}	10^6	10	**4.2**	$\mathbf{10^6}$	**0.55**	$\mathbf{2{\cdot}10^5}$
10^{-11}	$2.6{\cdot}10^9$	10^{11}	10^6	10	**4.2**	$\mathbf{10^6}$	**0.55**	$\mathbf{2{\cdot}10^5}$
10^{-12}	$2.6{\cdot}10^9$	10^{12}	10^6	10	**4.2**	$\mathbf{10^6}$	**0.55**	$\mathbf{2{\cdot}10^5}$

3.2. Noise model of SR570

The noise model of the SR570 is shown in fig. 6 (dashed box) together with the noise model of the DUT.

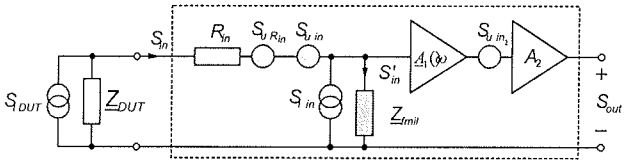

Fig. 6: The SR570 noise model with the DUT's impedance (Z_{DUT}) and current noise source ($S_{i\,DUT}$).

The DUT model is represented by the impedance Z_{DUT} and a current noise source $S_{i\,DUT}$. In the SR570 small signal model additional current and voltage noise sources are added, where only the voltage noise source $S_{u\,R_{in}}$, which represents the thermal noise of the input resistance R_{in}, can be analytically expressed:

$$S_{u\,R_{in}} = 4kTR_{in}. \tag{6}$$

Other noise sources (equivalent input voltage and current noise sources $S_{u\,in}$ and $S_{i\,in}$ and input voltage noise of the second stage $S_{u\,in2}$) can only be determined by the noise measurement of the amplifier at certain input conditions, at which only one of the noise sources prevails over others. The output noise S_{out} is a consequence of all noise sources

$$S_{out}(\omega) = \left(S'_{in}(\omega)\left|\underline{Z}_{fmil}\underline{A}_1\right|^2 + S_{u\,in_2}\right)A_2^2, \tag{7}$$

where the equivalent input noise S'_{in} can be expressed as:

$$S'_{in}(\omega) = \frac{S_{i\,in}(\omega)\cdot\left|\underline{Z}_{DUT}+R_{in}\right|^2 + S_{i\,DUT}(\omega)\cdot\left|\underline{Z}_{DUT}\right|^2 + S_{u\,in}(\omega) + S_{u\,R_{in}}}{\left|\underline{Z}_{DUT}+R_{in}+\underline{Z}_{fmil}\right|^2}. \tag{8}$$

At open circuit input conditions $\left|\underline{Z}_{DUT}\right| \to \infty$ we can assume

$$S_{i\,DUT}(\omega) \to 0 \;\Rightarrow\; S'_{in}(\omega) = S_{i\,in}(\omega), \tag{9}$$

and consequently becomes

$$S_{out}(\omega) = \left(S_{i\,in}(\omega)\left|\underline{Z}_{fmil}\underline{A}_1\right|^2 + S_{u\,in_2}\right)A_2^2. \tag{10}$$

The output noise can be transferred to the input

$$S_{in}(\omega) = S_{i\,in}(\omega) + \frac{S_{u\,in_2}}{\left|\underline{Z}_{fmil}\underline{A}_1\right|^2} \approx S_{i\,in}(\omega) + \frac{S_{u\,in_2}}{\left|\underline{Z}_f\right|^2}, \tag{11}$$

where at lower frequencies the input current noise $S_{i\,in}$ dominates, while towards higher frequencies the second stage voltage noise prevails due to drop of feedback impedance Z_f. In fig. 7 the measured and calculated current noise density spectra transferred to the input at open circuit input conditions of SR570 are presented, from which the parameters of the equivalent input current noise source $S_{i\,in}$ and second stage voltage noise source $S_{u\,in2}$ are determined. The input noise current source is described as a sum of flat spectrum and $1/f$ component in a form of .

$$S = S_0 + A_f / f^{\gamma} \tag{12}$$

The square roots values of parameters S_0, A_f, γ and $S_{u\,in2}$ at different transconductance settings are listed in table 2.

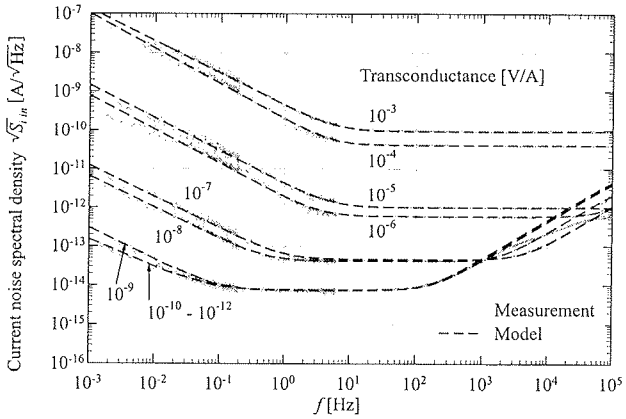

Fig. 7: Measured (full line) and calculated (dashed line) current noise density spectra of the SR570 transferred to the input at open circuit conditions.

Table 2: The list of parameters of the equivalent input current noise source $S_{i\,in}$ and second stage voltage noise source $S_{u\,in2}$.

	$S_{i\,in} = S_0 + A_f/f^{\gamma}$			$S_{u\,in_2}$
Transconductance [A/V]	$\sqrt{S_0}$ [A/√Hz]	$\sqrt{A_f}$ [A/√Hz]	γ	$\sqrt{S_{u\,in_2}}$ [V/√Hz]
10^{-3}	$9.3\cdot10^{-11}$	$4.3\cdot10^{-10}$	1.66	0
10^{-4}	$4.1\cdot10^{-11}$	$1.9\cdot10^{-10}$	1.82	0
10^{-5}	$9.9\cdot10^{-13}$	$4.2\cdot10^{-12}$	1.70	0
10^{-6}	$5.4\cdot10^{-13}$	$1.8\cdot10^{-12}$	1.76	$2.2\cdot10^{-7}$
10^{-7}	$4.0\cdot10^{-14}$	$4.4\cdot10^{-14}$	1.64	$3.2\cdot10^{-7}$
10^{-8}	$3.0\cdot10^{-14}$	$2.3\cdot10^{-14}$	1.64	$8.4\cdot10^{-7}$
10^{-9}	$7.1\cdot10^{-15}$	$1.1\cdot10^{-15}$	1.64	$1.7\cdot10^{-6}$
10^{-10}	$7.5\cdot10^{-15}$	$1.1\cdot10^{-15}$	1.44	$1.7\cdot10^{-6}$
10^{-11}	$7.5\cdot10^{-15}$	$1.1\cdot10^{-15}$	1.44	$1.7\cdot10^{-6}$
10^{-12}	$7.5\cdot10^{-15}$	$1.1\cdot10^{-15}$	1.44	$1.7\cdot10^{-6}$

The remaining noise parameter of SR570 that has to be determined is equivalent input voltage noise $S_{u\,in}$, which can be determined by output noise measurement at short-circuit input termination $\left|\underline{Z}_{DUT}\right| \to 0$. Under this condition Eq. 10 simplifies into

$$S'_{in} = \frac{S_{i\,in}\cdot\left|R_{in}\right|^2 + S_{u\,in} + S_{u\,R_{in}}}{\left|R_{in}+Z_{fmil}\right|^2}. \tag{13}$$

In order to avoid possible saturation of SR570 due to input offset voltage, we have measured noise density spectra at

all transconductance settings at standard 50 Ω BNC input termination. Considering already determined parameters of noise sources, we extracted the input voltage noise from measurement. Each of two distinct spectra, shown in fig. 8, can be attributed to one of the two preamplifiers used for two transconductance ranges. They can also be modeled as a sum of flat and $1/f$ components , as shown in table 3.

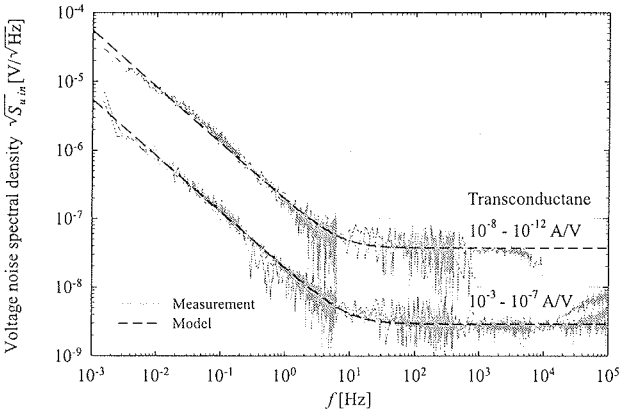

Fig. 8: Noise power density spectra of the equivalent input noise voltage source of SR570 at different sensitivities, extracted at 50 Ω input termination.

Table 3: The SR570 equivalent input noise voltage source parameters.

Transconductance range [A/V]	$S_{u\,in} = S_0 + A_f/f^{\gamma}$		
	$\sqrt{S_0}$ [V/√Hz]	$\sqrt{A_f}$ [V/√Hz]	γ
10^{-3} ... 10^{-7}	$2.9 \cdot 10^{-09}$	$1.9 \cdot 10^{-08}$	1.64
10^{-8} ... 10^{-12}	$3.5 \cdot 10^{-08}$	$1.7 \cdot 10^{-07}$	1.74

Using the obtained noise model we can investigate the influence of external factors to the overall noise of the SR570. The most direct one is the influence of the DUT impedance (Z_{DUT}), which will be shown separately for resistive and capacitive part, since most semiconductor photonic sensors exhibits capacitive nature. The influence of DUT resistance R_{DUT} on the system noise is presented for transconductance of 10^{-7} A/V in fig. 9. It is clearly seen, that the voltage noise increases while decreasing the R_{DUT} and would supersede other noise sources, if there wasn't input resistance R_{in}, which saturates the whole system noise. But unfortunately the current divider of R_{in} and R_{DUT} causes the decrease of the measured DUT current noise which further diminishes in the noise of R_{in}. Therefore for each transconductance setting there is a range of allowed DUT resistances that can give valid results. In the case of transconductance of 10^{-7} A/V this range spans approximately from 10^4 to 10^7 Ω.

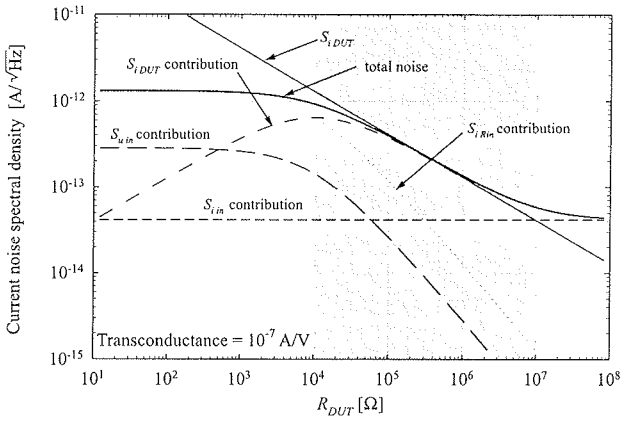

Fig. 9: Influence of the DUT resistance on the SR570 noise properties at f = 100 Hz. The usable R_{DUT} range is marked in gray.

To show the role of DUT capacitance (fig. 10) we chose the transconductance of 10^{-8} A/V, where the effect is more pronounced due to higher equivalent input noise voltage. At low frequencies the noise floor is limited by input current noise, while the influence of input voltage noise increases with frequency due to the decrease of DUT impedance. The DUT capacitance together with the inductive nature of input impedance forms a resonant peak, which can significantly raise the noise floor in case of high capacitive DUTs.

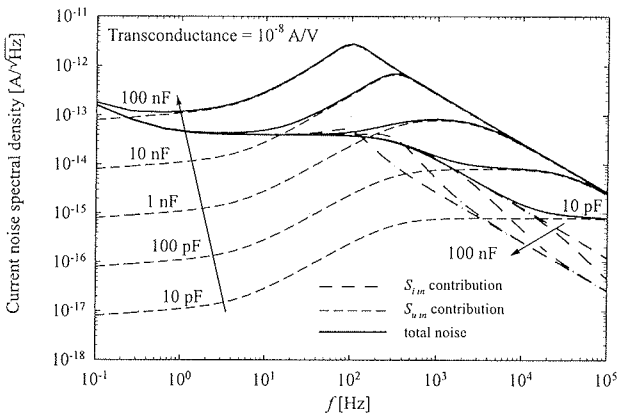

Fig. 10: Effect of the DUT capacitance on the SR570 noise performance.

3.3. Noise measurement of a-Si:H *pin* diode

In order to demonstrate the usefulness of the developed and characterized noise measurement setup results of noise measurement of an amorphous silicon (a-Si:H) *pin* diode are presented. The diode area was 1 mm^2 and the *p*, *i*, *n* layer thicknesses were 10, 400 and 20 nm, respectively. Since the noise model of our measurement system also requires known DUT impedance, we initially measured dynamic properties of the diode /9/.

From acquired system noise density spectra the part that originates from the diode is extracted using previously de-

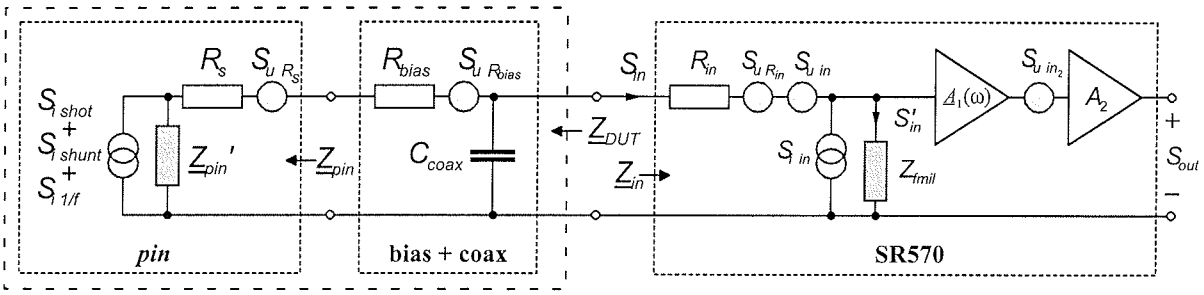

Fig. 11: Noise model of measurement system including a-Si:H pin diode, bias circuit, coaxial cable connection and SR570 transconductance amplifier.

scribed noise model of measurement system considering additional factors (voltage bias resistance thermal noise ($S_{u\,Rbias}$), coaxial cable capacitance C_{coax} and the noise model of the a-Si:H *pin* diode) as presented in fig. 11. The noise of offset voltage source U_{off} and the input noise of the SR780 FFT spectrum analyzer are neglected.

The noise model of the a-Si:H *pin* diode was formed on the basis of previously used noise models of similar devices /10, 11/. All dynamic parameters of the diode except series resistance R_s are combined in the impedance Z'_{pin}. The total noise of the a-Si:H *pin* diode is composed of three independent current noise sources: shot noise $S_{i\,shot}$, thermal noise of shunt resistance $S_{i\,shunt}$ and $1/f$ noise $S_{i\,1/f}$. In addition, a voltage thermal noise source of series resistance $S_{u\,Rs}$ is present. All noise sources except $1/f$ noise can be calculated from known diode parameters. The missing $1/f$ noise component is extracted from the measurement results accounting contributions of all other known noise components. Fig. 12 presents measured noise density spectra of aSi:H *pin* diode at forward bias of 420 nA at the output of SR570. Noise system components from noise model of the SR570 (Fig. 11) are shown as well. The influence of the voltage noise $S_{u\,in}$, particularly at lower frequencies, determines the system noise, which is a consequence of low diode impedance at forward bias. Measured noise spectrum prevails system noise almost in the whole frequency range and is approaching to the calculated noise spectrum of the measured diode at higher frequencies. The excess noise at frequencies below 100 Hz can be attributed to $1/f$ noise of the measured diode, but it diminishes in the system noise below 10 mHz, due to different slopes of spectra.

According to measured spectra, transferred to the input of SR570 (fig. 13), at frequencies above 100 Hz, shot noise of the diode ($S_{i\,shot}$) is dominant, while below 100 Hz the $1/f$ noise prevails. Thermal noises of series ($S_{u\,Rs}$) and shunt ($S_{i\,shunt}$) resistance are negligible. By subtracting the system, shot and thermal noise components from the measured noise, the excess noise spectrum can be extracted. It exhibits typical $1/f$ dependence and can be modeled by an empirical expression

$$S_{i,1/f} = \frac{A_f}{f^{\gamma}}, \qquad (14)$$

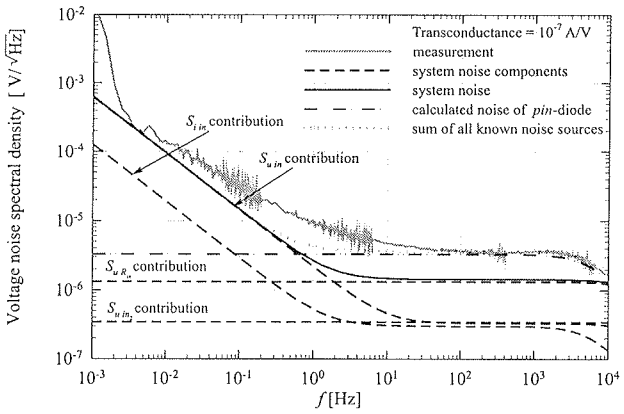

Fig. 12: Noise voltage density spectrum, measured at the SR570 output, of the a-Si:H pin diode at forward current bias of 420 nA. The contribution of individual noise sources of the measurement system and the known noise components of the pin diode are added for comparison. The observed excess noise is 1/f noise component of the pin diode.

where A_f is power density at f = 1 Hz and γ determines the slope of the spectrum. The $1/f$ shape of the spectrum with slope γ = 1.00 can be observed from f = 0.01 Hz (where it prevails system noise) up to 100 Hz, where it diminishes into the flat part of the spectrum. The noise current density of $1/f$ component at 1 Hz is $\sqrt{A_f} = 1.0 \cdot 10^{-12}\,\mathrm{A}/\sqrt{\mathrm{Hz}}$.

4. Discussion

The presented noise measurement system was successfully applied for the current noise measurement of a-Si:H *pin* diodes at low frequency range from 10 mHz up to 10 kHz. Below 10 mHz the high slope of the low-frequency system noise component makes the measurement uncertain, while the upper limit is determined mainly by the bandwidth of the LNA. One of the important outcomes of the presented study is that besides input current noise also input voltage noise of the transconductance amplifier is important. Its contribution is directly correlated to the impedance of the applied DUT, which also has to be known prior to actual noise measurement. In the case of low im-

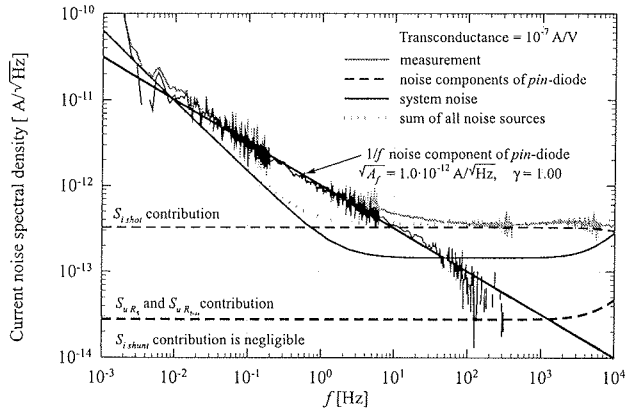

Fig. 13: Noise current density spectrum, transferred to the SR570 input, of the a-Si:H pin diode at forward current bias of 420 nA. The contribution of individual known noise sources of the pin diode and the total noise of the measurement system are added for comparison. The excess noise is subtracted from the calculated overall noise of the system, which yields 1/f noise component of the pin diode.

pedance or high capacitive DUTs the input voltage noise can mainly determine the total system noise performance. Thus, only by knowing all the parameters that influence the noise performance of the system, one can determine the part of the noise that originates from the DUT itself.

This is especially important in the case of noise measurements of high capacitive devices, such as large area aSi:H *pin* diodes with thin layers that exhibit high capacitance and very low intrinsic noise. In our case we could successfully measure only the smallest area diodes (1 mm^2) where the capacitance was sufficiently low thus keeping the input voltage noise below the critical values.

The problem of external low-frequency electric and magnetic interference was successfully eliminated by an arrangement of aluminum and mumetal shielding combination. The remaining external interference problems were mechanical vibrations that cause microphone effects in the input coaxial cable connections. This was partially solved by putting the system in the corner close to concrete walls and avoiding any movements near it as much as possible. Fortunately, the mechanical vibrations appear in the spectrum only at a certain frequencies and can be easily noticed. In such cases the measurement had to be repeated.

5. Conclusions

The low-frequency noise measurement system based on transconductance amplifier SR570 and a FFT spectrum analyzer SR780 was built. Dynamic and noise properties of the SR570 were thoroughly analyzed resulting in a comprehensive noise model of the complete measurement system. Besides other noise sources also 1/*f* noise components of the SR570 was identified. The influence of DUT impedance to the overall system noise properties was demonstrated. The noise measurement system utilizing the obtained noise model was used for low-frequency noise measurement of a-Si:H *pin* diodes. 1/*f* noise with the ideal slope (γ = 1.00) and noise density of $\sqrt{A_f}=1.0\cdot10^{-12}\mathrm{A}/\sqrt{\mathrm{Hz}}$ at 1 Hz was identified to be dominant below 10 Hz, while above 10 Hz the diode's shot noise prevails.

6. References

/1/ E. Uiga, Optoelectronics, Prentice Hall, New Jersey, 1995, ISBN 0-02-422170-8.

/2/ Ambrozy, Electronic noise, Akademiai kiado, Budapest, 1982, ISBN 963 05 2665 4.

/3/ H. Yoshida, M. Yoshida, T. Shinoda, I. Saito, I/f noise produced by the random motion of the carriers crossing potential barriers in semiconductors, J. Appl. Phys., Vol. 76, No. 11, 1994, pp. 7372-7376.

/4/ F. Blecher, Noise of a-Si:H pin diode pixels in imagers at different operating conditions, MRS proc., vol. 557, 1999, pp. 869-874.

/5/ F. Blecher, Photo- and dark current noise in a-Si:H pin diodes at forward and reverse bias, MRS proc., Vol. 507, 1998, pp. 175-180.

/6/ P. A. W. E. Verleg, Fluctuationg defect density probed with noise spectroscopy in hydrogenated amorphous silicon, MRS proc., Vol. 467, 1997, pp. 221-225.

/7/ Model SR780 Network Signal Analyser Manual, Stanford Research Systems, 1996.

/8/ Model SR570 Low-noise Current Preamplifier, Stanford Research Systems, 2000.

/9/ H. Stiebig, U. Nosan, M. Krause, M. Jankovec, M. Topič, Dynamic properties of ultraviolet sensitive detectors, J. Non-Cryst. Solids 338-340, 2004, pp. 772-775.

/10/ R. Miller, Rauschen, Springer-Verlag, ISBN 3-540-51145-8, 1990.

/11/ M. Jankovec, H. Stiebig, F. Smole, M. Topic, Noise characterization of a-Si:H pin diodes, J. Non-Cryst. Sol. 352, 2006, pp. 1829-1831.

Dr. Marko Jankovec, univ. dipl. ing. el.
Prof. Dr. Marko Topič, univ. dipl. ing. el.

University of Ljubljana,
Faculty of Electrical Engineering
Laboratory of Photovoltaics and Optoelectronics
Tržaška cesta 25, SI-1000 Ljubljana, Slovenia
Tel.: +386 (0)1 4768 321
Fax:+386 (0)14264630
E-mail: marko.jankovec@fe.uni-lj.si

Prispelo (Arrived): 19.04.2007 *Sprejeto (Accepted):* 15.06.2007

LOW-POWER DUAL-PORT ASYNCHRONOUS CMOS SRAM DESIGN TECHNIQUES

Tan Soon-Hwei, Loh Poh-Yee, Mohd-Shahiman Sulaiman, Zubaida Yusoff

Multimedia University, Cyberjaya, Malaysia

Key words: SRAM, Low-Power, CMOS, Dual-Port, Asynchronous, Non-volatile

Abstract: This paper describes the review and short tutorial on design techniques for low-power SRAM, focusing on the design of a 1-Mb CMOS SRAM on CMOS 0.25-μm process. The building blocks of the SRAM are individually discussed and various techniques are described, with the most appropriate one chosen for the block. SRAM power saving techniques are also described and implemented in the 1-Mb memory. The designed SRAM is simulated across different Process, Voltage, and Temperature (PVT) corners under the presence of parasitics. The performance of the 1-Mb SRAM is then compared with that of the previously published work. It is found that a minimum read access time of 4.26ns is achieved. The SRAM can operate at maximum frequency of 220MHz in dual-port mode and dissipates minimum active power of 31mW and is able to retain data at 0.1V supply voltage and consumes a standby power of 80nW. The SRAM occupies an area of 115mm^2.

Tehnike načrtovanja asinhronih dvovhodnih CMOS SRAM vezij z nizko porabo

Kjučne besede: SRAM, majhna poraba, CMOS, dvovhodni, asinhroni

Izvleček: V prispevku podamo pregled tehnik načrtovanja asinhronih dvovhodnih CMOS SRAM vezij z nizko porabo s poudarkom na načrtovanju 1-Mb CMOS SRAM vezja v 0,25um CMOS tehnologiji. Vsakega posebej opišemo sestavne bloke vezja SRAM, kakor tudi najbolj primerno tehniko načrtovanja. Ravno tako obravnavamo tehnike za zniževanje porabe in opišemo konkretni primer pri 1-Mb vezju. Načrtano vezje SRAM simuliramo pri različnih parametrih procesa ter vrednostih napetosti in temperature (PVT) ob prisotnosti parazitnih dejavnikov. Te rezultate primerjamo z drugimi predhodno objavljenimi rezultati. Ugotovimo, da dosežemo minimalni bralni čas 4.26ns. Vezje SRAM lahko deluje z največjo frekvenco 220MHz v dvovhodnem načinu, pri čemer porabi najmanj 31mW ter je zmožno ohraniti podatke tudi pri napajalni napetosti 0.1V. Poraba moči v stanju pripravljenosti je 80nW. Površina vezja je 115mm^2.

1 Introduction

Large portion of modern digital chips are occupied by memory and its capacity is forecasted to further increase in the new era of System on Chip (SoC). Hence high density while maintaining high-speed memory design is urgently needed by the semiconductor industry especially due to a great demand for cache applications in very fast processors. Concurrently, VLSI circuit designers also have to take power consumption problem into consideration due to the increased integration and operating frequency. In addition, portable equipment such as laptop computers, PDAs and cellular phones are more widely used nowadays and this raises the importance of low power design for longer battery operation /1/,/2/. This paper aims at exploring and implementing high speed and power savings techniques into memory design to overcome speed degradation and high power dissipation issues caused by large memory capacity.

This paper describes a 1-Mb SRAM with 64K words x 16-bit organization. The SRAM operates properly with the supply voltage of 1.5V in order to support portable equipment running on 1.5V batteries. A minimum 4.6ns access time and 31mW active power have been achieved by Hierarchical Word Decoding architecture, current-mode technique and pulse-mode technique. The proposed SRAM has four operation modes - active read mode, active write mode, active dual-port mode and standby mode.

Section 2 of this paper discusses circuit design and circuit techniques used for the SRAM. Characteristics of the designed SRAM and brief performance comparisons with other published works are presented in Section 3. This paper is concluded in Section 4.

2 Circuit Design & Techniques

2.1 Chip Architecture & Hierarchical Word Decoding

HWD architecture reduces latency by accessing smaller memory blocks. The principle in this technique is to partition memory array into several portions and to map these portions to different physical memory banks that can be selected or deselected independently. Also, it reduces power dissipation by shutting down portions that are not accessed potentially /3/.

The overall block diagram of the SRAM is illustrated in Figure 1. A 1-Mb memory array is partitioned into four quadrants and each quadrant contains eight 32Kb local blocks. Each local block contains 256 rows and 128 columns of memory cells. Row select word-line has a three-level hierarchical structure, which are global word-lines, sub-global word-lines and local word-lines. All quadrants are connected to an I/O block that contains data, signal and address input buffers, data output multiplexers and data output buffers. Tapered buffers with large current driving capabil-

ity are used. Control block contains Address Transition Detection (ATD) circuit and global control circuitry. The pre-decoder, global row decoder, sub-global row decoder and local row decoder works together to generate row select signals for the local blocks. Global row decoder contains a 2-to-4 decoder that selects one out of the four quadrants. Sub-global row decoder contains a 3-to-8 decoder that selects one out of the eight local blocks. Local row decoder contains buffers that drive the large word-line capacitive load. A pre-decoding stage is used to reduce transistors count and decoding delay. Two sets of decoder were placed to support dual-port design.

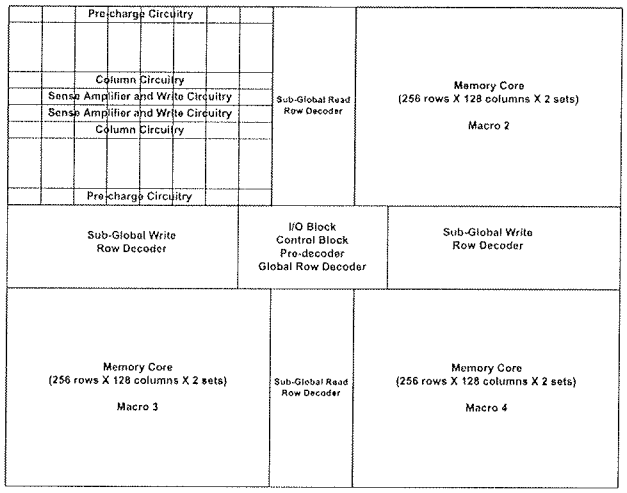

Fig. 1: Overall Block Diagram of 1Mb SRAM

Row select signals are distributed to 32 local blocks. These signals can be ensured to arrive at different blocks with similar delay by using Balanced Path H- Tree or X-Tree Signaling technique. H-Tree signaling technique was chosen for this paper. It is particularly useful for regular array networks as the loading of each node leaf is equal.

Figure 2 shows the HWD decoding stages for read and write decoders. Read/write enable signal is ANDed with ATD signal at the very beginning of decoding stage to avoid instantiating internal operation when SRAM is disabled and thus save power. The SRAM is also implemented advanced read function implicitly. When read memory instruction with same address is assigned to the SRAM subsequently, the ATD circuit stops generating control pulse and thus no internal operation will occur. Instead, previous data outputs are used and this contributes to more power savings.

2.2 Current-mode Sensing & Writing Technique

Voltage-mode sense amplifier senses differential voltage in the bit-lines and convert it to full-rail swing output. Voltage-mode write circuitry pulls down bit-lines voltage to certain voltage level that can overpower the memory cell. These voltage-mode circuitries can cause large bit-line voltage swing and hence power dissipation problem. Also, speed degradation is another problem as the discharging delay for pulling down bit-lines voltage is long especially when the bit-line capacitance is large. Other than that, a long period is required to restore bit-lines voltage after every operation.

To avoid these problems, current-mode technique is implemented for the SRAM in this paper. It was first proposed by /4/. The main idea is to use a low-resistance current-signal circuit to reduce voltage swing on the long transmission line and to avoid speed degradation problem caused by signal delay in the high capacitive interconnect. Delay of current-mode circuitry is insensitive to bit-line and data-

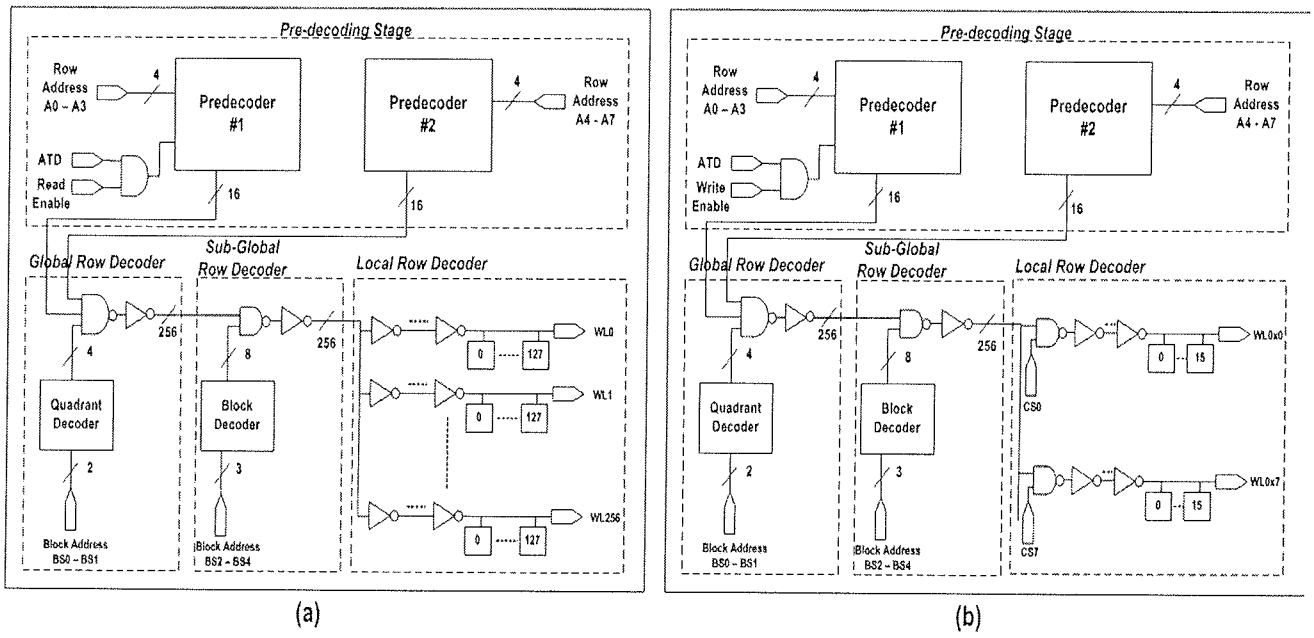

Fig. 2: (a) HWD Read Decoding Stages (b) HWD Write Decoding Stages

line capacitance /3/,/5/. In addition, it helps to reduce coupling noise to the adjacent bit-lines as bit-lines voltage swing is minimized.

Figure 3 shows a block diagram that describes the internal structure of the local 32Kb memory block that implements current-mode technique. Two sets of local row decoder and column decoder have been placed to support the dual-port feature. Column selector and current conveyor pass data in electrical forms to the local output circuitry. Column selector determines which column is selected for operation. Current conveyor acts like a current signals transmitter and is part of the current-mode circuitry. Local data output circuitry has a current-mode sense amplifier, output latch and tapered buffers. Local data input circuitry has a current-mode write circuitry and tapered buffers. Write circuitry translates input data into recognized electrical signals to modify memory cell's data.

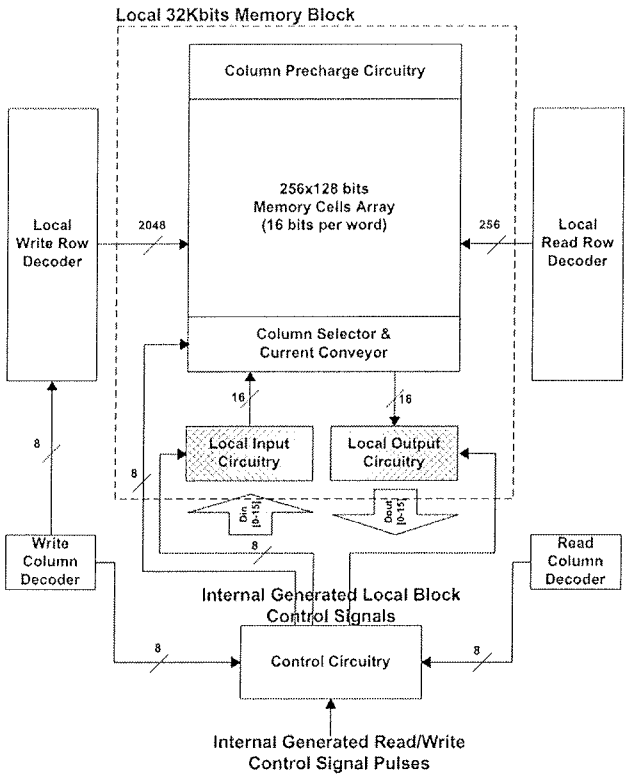

Fig. 3: Block Diagram of Local Memory Block

Figure 4 shows the bit-line peripheral circuits. It includes 7T memory cell, per-charge circuitry, current conveyor and column selector. 7T memory cell is used to implement current-mode writing technique. An additional equalization transistor is added and it forms a write port whereas the access transistors form a read port. The Source terminals of the PMOS transistors are connected to two common voltage lines that are called write bit-lines. These bit-lines connect pre-charge circuitry and other memory cells of the same column. PMOS-based pre-charge circuitry is used and is biased in linear region. No external control signal is supplied to the pre-charge circuitry as bit-lines capacitance is not needed to be discharged. Two sets of pre-charge circuitry are placed to support dual-port design. A two-input two-output PMOS-based current conveyor based on Caprio's bipolar cross-coupled quad circuit is used to implement current-mode technique /4/. This current conveyor forms a virtual short-circuit to the bit-lines and transports currents to the inputs of Clamped Data Line Sense Amplifier. In addition, it also serves as a column selector circuit. Current conveyor consists of four PMOSs and all transistors must be of equal size to create similar voltage level at input nodes of the circuit. Also, it contains an additional equalization transistor to solve the pattern-dependant problem /5/. Column equalization signal enable this transistor after every read operation. All the PMOS transistors in the current conveyor circuit operate in saturation region.

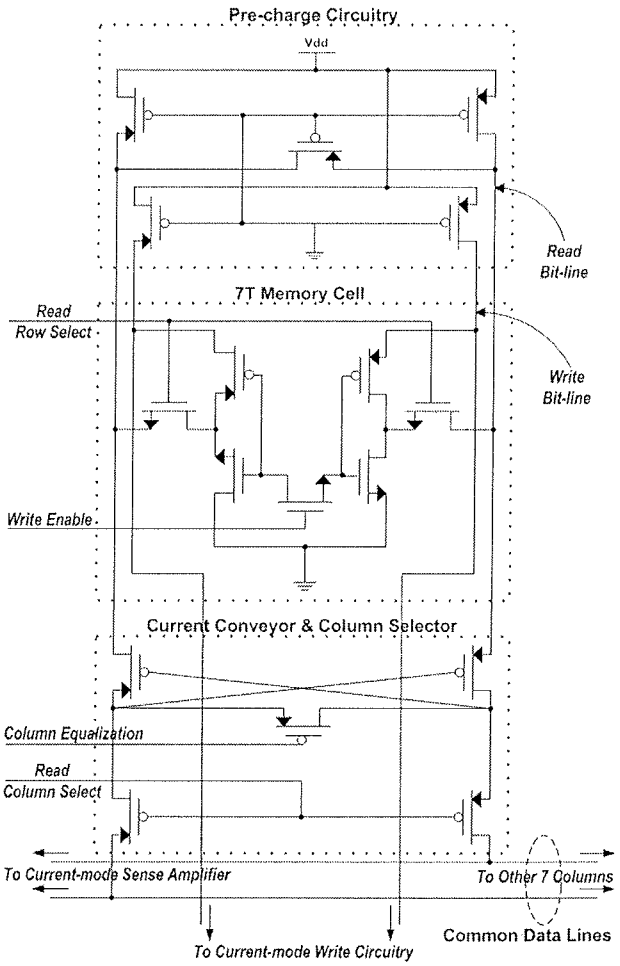

Fig. 4: Bit-line Peripheral Circuits

In general, current-mode sensing circuit is composed of current transporting circuit and current-to-voltage converter. A current transporting circuit or current conveyor is required to have two characteristics - low input resistance and unity current gain. Its main function is to transport differential currents from bit-lines to common data-lines when a memory column is selected. A current-to-voltage converter senses the differential input currents and convert these differential signals to a full swing CMOS voltage. Clamped Data Line Sense Amplifier (CDLSA) circuit topol-

ogy is chosen in this paper /6/. Figure 5 shows the transistor-level circuit of CDLSA. It clamps the data-lines using two NMOS transistors (M5 & M6) that are tied to ground and forces it to a voltage level closed to ground to provide virtual short-circuit feature. It also contains a cross-coupled inverter M1-M4 that provides complementary outputs. It has an equalization NMOS, Meq, that drives the cross-coupled inverter to meta-stable state during equalization phase.

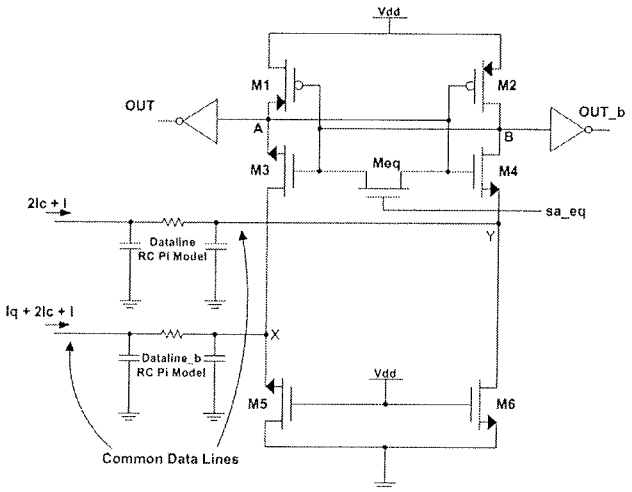

Fig. 5: Clamped Data Line Sense Amplifier

The circuit operates in two phases: equalization phase and sensing phase. During equalization phase, sense amplifier equalization signal (sa_eq) is pulled high to equalize voltage at node A and node B. The signal is disabled to start the sensing phase after sufficient differential currents are built up. M3 and M4 sources the differential currents into sense amplifier output nodes. Then, the small parasitic capacitance at output nodes are charged to either higher or lower voltage level depends on the differential currents flow in. Cross-coupled inverter forms a positive feedback amplifier to amplify the differential nodes voltage to corresponding CMOS voltage level.

The SRAM implements current-mode writing technique that was proposed by /7/. The proposed technique has a limitation where size of the row of a memory block must equal to SRAM word size. In this paper, row decoder and local control circuit have been redesigned so that the write circuitry can perform operation to the chosen columns only. The column select signal is ANDed with row select signal before reaching memory cell's write port. Figure 6 shows the transistor-level circuit of current-mode write circuitry and its circuit operation. Current-mode write operation can be achieved by loading differential currents into storage nodes of memory cell through the write bit-lines. This circuit operates in two phases: equalization phase and evaluation phase. Before equalization phase begins, write enable signal arrives earlier and either M8 or M9 is turned ON. If M9 is turned ON, current flows through M9 to ground and causes current flowing into the storage node becomes lesser. During equalization phase, write equalization signal turns ON M7 and the storage nodes are forced to a voltage level closed to V_{dd} /2. As M3 and M5 sources different currents, nodes capacitance is charged to different voltage levels. During evaluation phase, M7 is disabled and the differential voltage between two nodes is amplified to full swing CMOS voltage level. M10-M13 are placed as shown in Figure 6 to pass both high and low input voltages effectively and hence M8-M9 can be biased to operate in either saturation region or cut-off region.

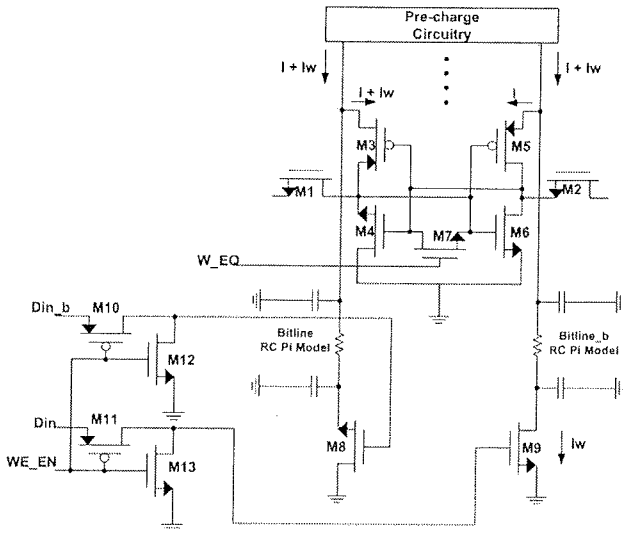

Fig. 6: Current-mode Write Circuitry

2.3 Pulse-mode Technique & ATD Circuit

Pulse-mode technique is one of the two most commonly used techniques in reducing dc current /8/. When external clock signal is used for generating internal control signals, the circuit is turned on every cycle yet no operation is requested. Besides that, the clock cycle period might be too long for an operation to complete. As a result, asynchronous SRAM design using Address Transition Detection (ATD) circuitry is invented to reduce power consumption by supplying pulse signals to the internal circuitries.

A simple ATD circuit together with the ATD pulse signal waveform is shown in Figure 7. The main function of ATD is to generate a pulse whenever a transition of address signal is triggered. Duration of the ATD pulse is determined by the delay element in ATD circuit. The delay element circuit is designed such that pulse duration will be just enough for an SRAM operation to complete. In order to generate pulses of similar pulse width under various conditions, modified Schmitt Trigger delay circuit is used as the delay element. It uses capacitors to control the delay time. This design can generate different delay by altering the size of capacitor /9/. The transistor-level circuit of delay circuit is shown in Figure 8.

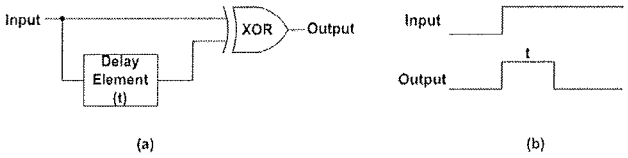

Fig. 7: ATD Circuit and Output Waveform

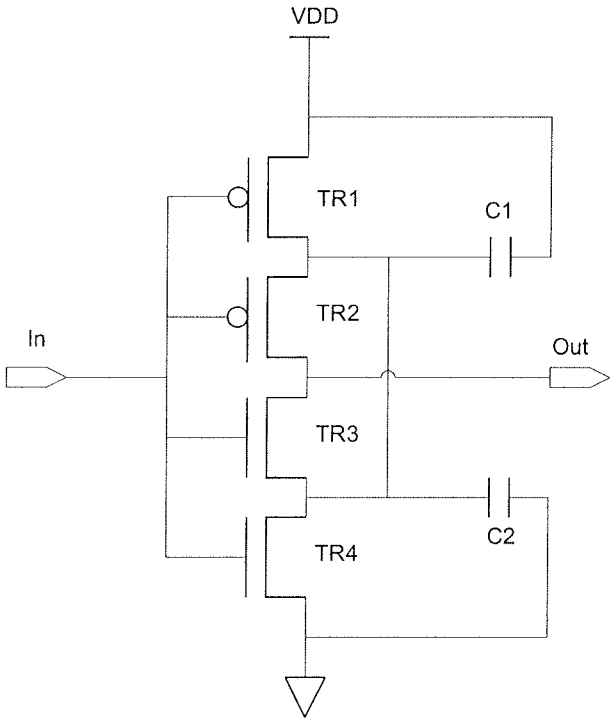

Fig. 8: Modified Schmitt Trigger Delay Circuit

Pseudo-NMOS is implemented to perform NOR operation to the 17 inputs (Refer to Figure 9). Pseudo-NMOS also avoids the series connection of PMOS transistors and reduces transistor count. However, this design suffers from reduced noise margin and high static power dissipation.

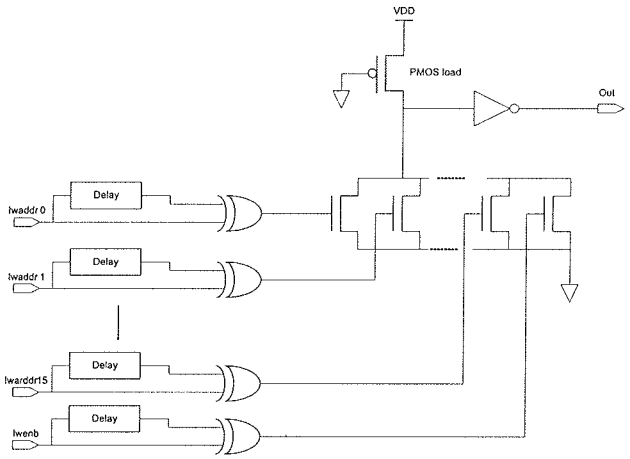

Fig. 9: Pseudo NMOS OR gate ATD

3 RAM performance

The SRAM was validated under various process, voltage and temperature (PVT) corners as listed in Table 1. Stimulus was setup so that a write operation was performed first followed by a dual-port operation and then a read operation.

Table 1: Simulation Conditions for 1Mb SRAM

Parameter	*Range*
Supply Voltage	1.4V - 1.6V
Temperature	25°C - 85°C
Process Corner	TT,FF,FS,SF,SS
Input Signal Slope (10% - 90%)	80ps - 400ps

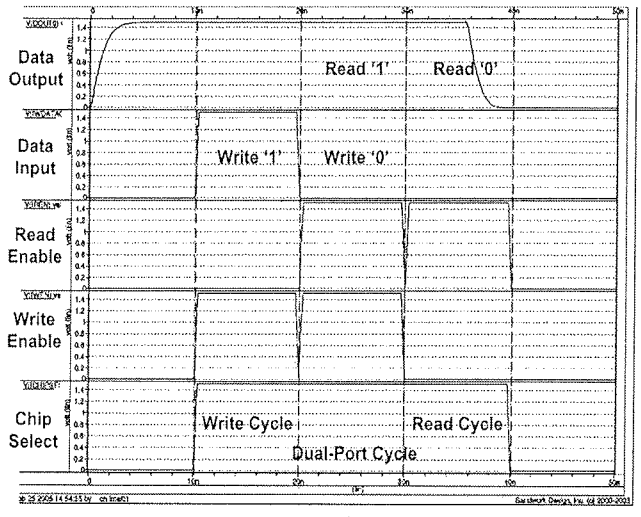

(a)

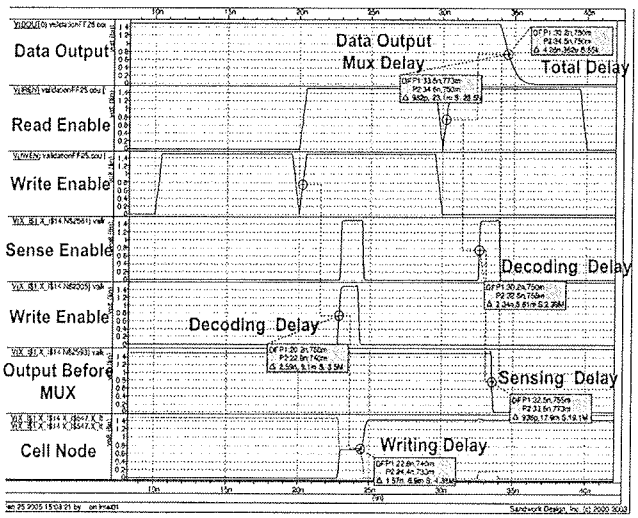

(b)

Fig. 10: (a) Simulation Waveform of 1Mb SRAM (b) Delay Measurement

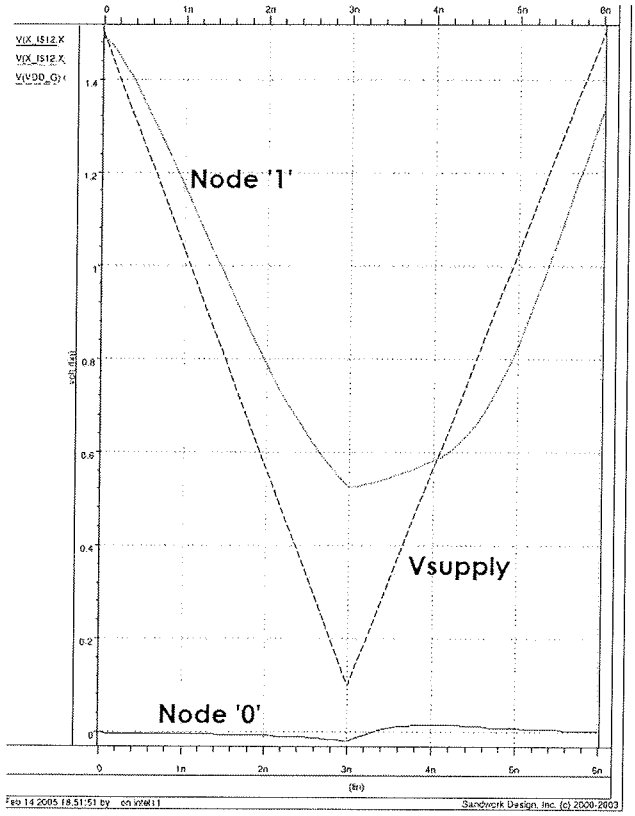

Fig. 11: Data Retention Analysis

Simulation waveform is shown in Figure 10(a) together with the minimum delay measurement shown in Figure 10b. Minimum read access delay, decoding delay, sensing delay and output MUX delay were measured as 4.26ns, 2.34ns, 0.93ns and 0.98ns, respectively. The maximum operating frequency is 220MHz@FF 25°C, 1.5V, and the typical operating frequency is 160MHz@TT, 1.5V. In contrast to the voltage-mode SRAMs, the designed SRAM has omitted two delay stages. They are bit-line/circuit recovery delay and discharging delay. Minimum average active current for read cycle is 13.35mA, write cycle is 13.52mA and dual-port cycle is 20.75mA.

Data retention analysis was performed and the simulation waveform is shown in Figure 11. It is used to measure the minimum supply voltage for which the designed memory cell can still retain the stored data. From simulations, it is found that the memory cell is able to retain data even the supply voltage is ramped from 1.5V to 0.1V across all skews with varied temperature. Minimum standby current at 0.1V supply voltage is 0.8μA. Therefore, standby power can be reduced significantly by lowering the supply voltage during suspend mode. However, additional voltage down converter (VDC) circuit is needed to downgrade the supply voltage to 0.1V.

Compared to other published papers on SRAM design, this project is projected to achieve smaller read access delay and lower active power. The read access delay comparison is shown in Table 2 and active power consumption comparison is shown in Table 3. The major characteristics of the SRAM are summarized in Table 4.

Table 2: Read Access Delay Comparison

	This Project	*/9/*	*/10/*	*/11/*
CMOS Process	0.25μm	0.3μm	0.35μm	0.5μm
Vsupply	1.5V	3V	3V	3.3V
Sensing Technique	Current Mode	Current Mode	Current Mode	Voltage Mode
Memory Size	1Mb	1Mb	256Kb	4Mb
Read Access Delay	4.26ns	7ns	9ns	25ns

Table 3: Active Power Consumption Comparison

	This Project	*/9/*	*/12/*	*/10/*
CMOS Process	0.25μm	0.3μm	0.5μm	0.35μm
Vsupply	1.5V	3V	5V	3V
Operating Freq(MHz)	150	100	100	100
Memory Size	1Mb	1Mb	1Mb	256Kb
Active Power	31.13mW (Dual-Port)	140mW	260mW	84mW

Table 4: Characteristics of SRAM

Organization	64K words x 16-bit
Power Supply Voltage	1.5 ± 0.1V
Operating Frequency	Max: 220MHz Typical: 160MHz
Read Access Time	Min: 4.26ns Typical: 5.94ns
Average Active Current	Min : Read: 13.35mA Write: 13.52mA Dual-Port: 20.75mA Typical : Read: 21.13mA Write: 23.18mA Dual-Port: 29.75mA
Min Data Retention Voltage	0.1V
Standby Current@0.1V	Min: 0.8μA Typical: 6.2μA
Die Size	≈ 11.5mm x 10mm
Tested Input Signal Slope	100ps - 500ps

4 Conclusions

An example for a design of an asynchronous dual-port 1-Mb CMOS SRAM with 64K words x 16-bit organization has been presented. The SRAM employs various low-power SRAM design techniques and is capable of performing read and write operations simultaneously. Hierarchical Word Decoding has been implemented at architecture-level to reduce decoding delay needed for large memory array. At circuit-level, the proposed SRAM implements current-mode techniques for both read and write operation. Power consumption can be further reduced by using pulse-mode technique together with the ATD circuit.

5 References

/1/ Kiyoo Itoh et. al, "Trends in Low Power RAM Circuit Technologies", *IEEE Symp. Low Power Elec. Dig. of Tech. Papers*, pp. 84-87, Oct. 1994.

/2/ Hiroki Morimura et. al, "A 1-V 1-Mb SRAM for Portable Equipment", *IEEE In. Symp. on Low Power Electronics and Design*, pp. 61-66, Aug. 1996.

/3/ P. Y. Chee et. al, "A High-speed Current-mode Sense Amplifier for CMOS SRAMs", *Proc. of the 35th Mid. Symp. on Circuits and Sys.*, pp. 620-622, Aug. 1992.

/4/ Evert Seevinck et. al, "Current-mode Techniques for High-speed VLSI Circuits with Application to Current Sense Amplifier for CMOS SRAMs", *IEEE J. Solid-State Circuits*, vol. 26, pp. 525-536, April 1991.

/5/ H. Wang et. al, "A Low Power Current Sensing Scheme for CMOS SRAM", *IEEE In. Workshop on Memory Tech. Design & Testing*, pp. 37-45, Aug. 1996.

/6/ Jinn-Shyan Wang et. al, "Low-Power Embedded SRAM Macros with Current-Mode Read/Write Operations", *Proc. IEEE Symp. Low Power Elec. and Design*, pp. 282-287, Aug. 1998.

/7/ Muhammad M. Khellah et. al, "Circuit Techniques For High Speed And Low Power Multi-Port SRAMs", *Proc. 11th Annual IEEE In. ASIC Conference*, pp. 157-161, Sept. 1998.

/8/ Martin Margala, "Low-Power SRAM Circuit Design", *IEEE In. Workshop on Memory Tech., Design and Testing*, pp. 115-122, Aug. 1999.

/9/ Katsuro Sasaki et. al, "A 7-ns 140-mW 1-Mb CMOS SRAM with Current Sense Amplifier", *IEEE J. Solid-State Circuits*, vol. 27, pp. 1511-1518, Nov. 1992.

/10/ S. M. Wang et. al, "Full Current-Mode Techniques for High-Speed CMOS SRAMs", *IEEE In. Symp. on Circuits and Sys*, pp/ 580-582, May 2002.

/11/ Fumio Miyaji et. al, "A 25-ns 4-Mbit CMOS SRAM with Dynamic Bit-Line Loads", *IEEE J. Solid-State Circuits*, vol. 24, pp. 1213-1217, Oct. 1989.

/12/ Teruo Seki et. al, "A 6-ns 1-Mb CMOS SRAM with Latched Sense Amplifier", *IEEE J. Solid-State Circuits*, vol. 28, pp. 478-483, April 1993.

/13/ Toshihiko Hirose et. al, "A 20-ns 4-Mb CMOS SRAM with Hierarchical Word Decoding Architecture", *IEEE J. Solid-State Circuits*, vol. 25, pp. 1068-1074, Oct. 1990.

/14/ Akinori Sekiyama et. al, "A 1-V Operating 256-kb Full CMOS SRAM", *IEEE J. of Solid-State Circuits*, Vol. 27, May 1992.

/15/ Jinn-Shyan Wang et. al, "A New Current-Mode Sense Amplifier for Low-Voltage Low-Power SRAM Design", *11th Annual IEEE In. ASIC Conference*, pp. 163-167, Oct. 1998.

Tan Soon-Hwei, Loh Poh-Yee, Mohd-Shahiman Sulaiman, Zubaida Yusoff
Multimedia University, Cyberjaya, Malaysia
zubaida@mmu.edu.my

Prispelo (Arrived): 20.07.2007 *Sprejeto (Accepted):* 15.06.2007

WAVELET BASED NOISE REMOVAL FROM EMG SIGNALS

M. S. Hussain[1], M. B. I. Reaz[1], M. I. Ibrahimy[1], A. F. Ismail[1], F. Mohd-Yasin[2]

[1]International Islamic University Malaysia, Kuala Lumpur, Malaysia
[2]Faculty of Engineering, Multimedia University, Selangor, Malaysia

Key words: Denoising, Mean power frequency, SEMG, wavelet transform.

Abstract: Wavelet transform has been applied in this research for removing noise from the surface electromyography signal (SEMG). The effectiveness of the noise removal is quantitatively measured using Root Mean Square (RMS) Error. This paper reports on the effectiveness of the wavelet transform applied to the SEMG signal as means of removing noise to retrieve information related to muscle contraction and nerve system. Power spectrum analysis has been applied to SEMG signals where mean power frequency was calculated to indicate changes in muscle contraction. Wavelet based noise removal and power spectrum analysis on the EMG signal from the right "biceps brachii" muscle was performed using four wavelet functions. With the appropriate choice of the wavelet function (WF), it is possible to remove noise effectively to analyze SEMG significantly. Results show that WFs Daubechies (db2) provide the best noise removal from the raw SEMG signals among other WFs Daubechies (db6, db8) and orthogonal Meyer. The algorithm is intended for FPGA implementation of portable bio medical equipments to detect neuromuscular disease and muscle fatigue.

Odprava suma iz EMG signalov z valčno tranformacijo

Kjučne besede: odstranjevanje šuma, srednja frekvenca šuma, SEMG, valčna tranformacija

Izvleček: V prispevku opišemo uporabo valčne transformacije za odpravo šuma iz signala SEMG (Surface ElectroMyography Signal) z namenom pridobiti informacijo o povezavi med krčenjem mišice in živčnim sistemom. Učinkovitost metode kvantitativno izmerimo z izračunom RMS napake pri odpravi šuma. Za odpravo šuma iz EMG signala desne mišice "biceps brachii" smo uporabili štiri valčne funkcije. Rezultati kažejo, da s funkcijo Daubechies (db2) dosežemo najboljše rezultate med izbranimi (db6, db8 in ortogonalna Mayer funkcija). Algoritem nameravamo v končni fazi implementirati v vezje FPGA za uporabo v prenosni biomedicinski opremi za ugotavljanje nevromišičnih obolenj in mišične utrujenosti.

1. Introduction

EMG signal represents the electrical activity of muscles to gather information about muscular and nervous systems. It is commonly used in diagnosis of muscle weakness, muscle fatigue, nerve damage etc /1/. EMG signals detected directly from the muscle or from the skin by using surface electrodes, respectfully, show a train of motor unit action potentials (MUAP) plus noise. It is difficult to obtain high-quality electrical signals from EMG sources because the signals typically have low amplitude (in range of mV) and are easily corrupted by noise. The simplest way method of removing narrow bandwidth interference from recorded signal is to use a linear, recursive digital notch filter. But the disadvantage of the notch filter is that, it distorts the signal /2/.

Wavelet-based noise removal is performed in this research prior to EMG signal analysis. Wavelet denoising (noise removal) has been found effective in denoising a number of physiological signals /3/. It is preferred over signal frequency domain filtering because it tends to preserve signal characteristics even while minimizing noise. This is because a number of threshold strategies are available, allowing reconstruction based on selected coefficients /4/.

It is desired to apply a method of spectral analysis to study the frequency characteristics of random signals like EMG. In the SEMG, recruitment and increase in the firing frequencies are seen as an amplitude increase of the SEMG signal /5/. Changes in the EMG power spectrum are used as an indicator of changes in muscle contraction and muscle fatigue for ergonomic purposes /6/.

For this study wavelet functions, Daubechies (db2, db6, db8) and Meyer (dmey) are used during the wavelet transform for noise removal. These WFs are chosen based on the shapes of the mother wavelet, which are similar to MUAP /3, 7/. RMS Error was calculated to measure the effectiveness of the noise removal using these wavelets. As a tool for analyzing frequency components of the EMG signals, Fast Fourier Transform (FFT) is considered. A superposed EMG signal can be considered as summation of sine waves with different frequency velocity. The FFT algorithm is described as a decomposition of the EMG signal to its underlined sinus contents. Within applied EMG frequency analysis the most important parameters are the mean and median.

Results show that, WFs db6, db8 and dmey show similar kind of RMS error indicating that they perform similar kind of noise removal for SEMG. Meanwhile, WF db2 presents less RMS error compared to the other three WFs, resulting better noise removal for the EMG signal. The effectiveness was observed more clearly while analyzing the power spectrum properties of the SEMG signals.

2. Methodology

For this experiment, 6 separate EMG data files were used. The sample raw EMG signals of a subject from University Kebangsaan Malaysia are used for the simulation of the algorithm. SEMG was recorded from the left "biceps brachii" muscle of a normal subject aged 22. All analog channels are recorded at 1000 samples per second. Two surface electrodes were used to capture the raw EMG signals and the distance between the electrodes were 3.5 inches. SEMG signal was captured during the subjects rest position, light contraction level, strong contraction level and contraction with load (weight 1 kg).

These SEMG signals were denoised using discrete wavelet transform (DWT) and a threshold method. The DWT and threshold based denoising was implemented using MATLAB Wavelet toolbox. Mean frequency from the power spectrum was calculated to estimate the muscle contraction at various muscle contraction stages. Fig. 1 shows the flow of the algorithm.

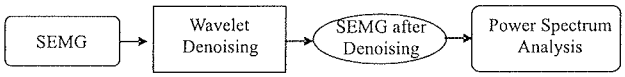

Fig. 1 Algorithm flow

A. Wavelet Denoising

Wavelets commonly used for denoising biomedical signals include the Daubechies 'db2', 'db8' and 'db6' wavelets and orthogonal Meyer wavelet. The wavelets are generally chosen whose shapes are similar to those of the MUAP /3/. Fig. 2 gives the process of noise removal using wavelet transform.

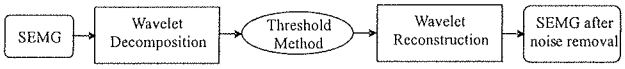

Fig. 2 Wavelet denoising method

Wavelet decomposition: The WT decomposes a signal into several multi-resolution components according to a basic function called the wavelet function. Filters are one of the most widely used signal processing functions. The resolution of the signal, which is a measure of the amount of detail information in the signal, is determined by the filtering operations, and the scale is determined by upsampling and downsampling (subsampling) operations. The DWT is computed by successive lowpass and highpass filtering of the discrete time-domain signal as shown in Fig. 3. In the figure, the signal is denoted by the sequence **x[n]**, where n is an integer. The low pass filter is denoted by G_0 while the high pass filter is denoted by H_0. At each level, the high pass filter produces detail information, **d[n]**, while the low pass filter associated with scaling function produces coarse approximations, **a[n]**. With this approach, the time resolution becomes arbitrarily good at high frequencies, while the frequency resolution becomes arbitrarily good at low frequencies.

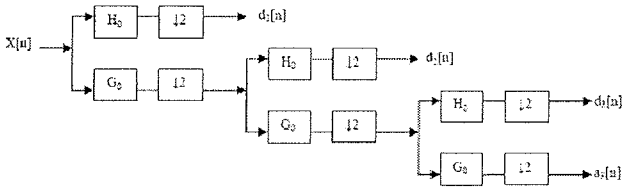

Fig. 3 Three level wavelet decomposition tree

Threshold method: Suppose that the contaminated signal **f** equals the SEMG signal **s** plus the noise signal **n**. The threshold method is applied as followed:

1. The energy of the original signal **s** is effectively captured, to a high percentage, by transform values whose magnitude are all greater than a threshold, $T_s > 0$.
2. The noise signal's transform values all have the magnitudes while lie below a noise threshold T_n satisfy $T_n < T_s$.

Then the noise in **f** can be removed by thresholding its transform. All values of its transform whose magnitude lies below the noise threshold T_n are set equal to 0.

Signal reconstruction: An inverse transform is performed, providing a good approximation of **f**. The reconstruction is the reverse process of decomposition. The approximation and detail coefficients at every level are upsampled by two, passed through the low pass and high pass synthesis filters and then added. This process is continued through the same number of levels as in the decomposition process to obtain the original signal.

B. RMS Error Calculation

The RMS Error of the contaminated signal **f** compared with the original signal **s** is defined by equation 1.

$$RMS\ Error = \sqrt{\frac{(f_1 - s_1) + (f_2 - s_2) + \ldots + (f_N - s_N)}{N}} \quad (1)$$

The RMS Error was calculated for the four WFs where **f** is the raw SEMG signal and **s** is the signal after denoising. **N** is the number of samples.

C. Power Spectrum Analysis

Power Spectrum Analysis: The power spectrum (PS) was obtained using fast Fourier transform (FFT) techniques. Hanning window was used with a 256 point FFT. The mean power frequency was obtained from equation 2.

$$pf_{mean} = \frac{\int fPS(f)df}{\int PS(f)df} \quad (2)$$

3. Results and discussion

Wavelet denoising method is applied to SEMG signal at various muscle contraction stages (rest, light contraction, strong contraction and contraction with load). RMS Error

was calculated for each of the WFs (db2, db6, db8 and dmey) during all the muscle contraction states, which are given by table 1.

Table. 1 RMS error of SEMG signal at various stages using four WFs

Muscle Stage	db2	db6	db8	dmey
Rest	0.005	0.005	0.005	0.005
Light	0.0162	0.0166	0.0166	0.0163
Strong	0.0279	0.0281	0.027	0.0272
Load (Start Point)	0.0632	0.0641	0.0621	0.0608
Load (Mid Point)	0.0795	0.0826	0.0801	0.0811
Load (Fatigue Point)	0.0388	0.0385	0.0385	0.0391

Similar kind of RMS Error is found using db6, db8 and dmey. RMS Error is less using db2 compared to the other WFs, which means that it is more effective during the noise removal process. Fig. 4 illustrates the result of denoising method using db2 with 4 levels of decomposition for a sample SEMG signal.

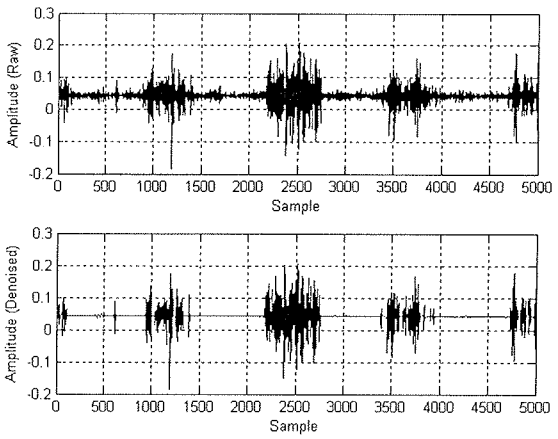

Fig. 4 Noisy SEMG from "Biceps Brachii" muscle (top) and result of wavelet denoising performed using the 'db2' wavelet with 4 levels of decomposition (bottom)

The mean power spectrum was calculated for the analysis of SEMG signal. According to the study by Hagberg and Ericson, mean power frequency was lower at low contraction levels when compared with high contraction levels /8/. Moritani et al. also obtained similar results where significant increase in SEMG amplitude and mean power frequency were found with increasing force /9/. It is also shown that during muscle fatigue, the power spectrum of SEMG shows a shift to lower frequencies /10/. Mean/ Median frequency is used to quantify this shift. The cause of this is related to the changes in the MU and changes in the firing characteristics of the MU. The analysis performed in this study also shows that mean power frequency increased with increase of muscle contraction. Fatigue was also noticed by observing a shift to lower frequencies in the power spectrum. Fig. 5 shows the mean power frequency of SEMG signal at the various muscle contraction stages using the WFs. According to the figure, mean power frequency for all four WFs increased from rest stage to strong muscle contraction stage. The contraction further increased when the load was added. However, mean power frequency dropped from the initial load stage to the end of the muscle contraction indicating muscle fatigue. The effectiveness of noise removal using WF db2 is also clear in fig. 5 where the curve shows higher mean power frequency for the SEMG signal which gives a better representation of muscle contraction during at higher muscle contraction stages.

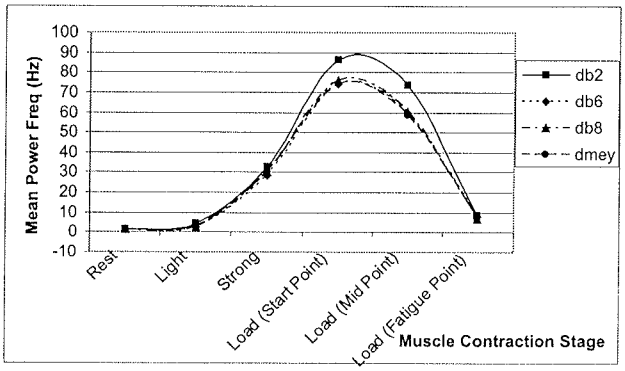

Fig. 5 Mean power frequency of SEMG signal at various muscle contraction stages using the WFs

4. Conclusion

Wavelet based noise removal has the added advantage that it is fast and easy to implement. Wavelet theory has already enjoyed great success in other biomedical signal processing, and expected to provide a powerful complement to conventional noise-removal techniques (such as notch filters and frequency domain filtering as mentioned earlier) for EMG signals. All four WFs can effectively remove noise from SEMG signal but according to this research, WF db2 is found to be most efficient for removing noise from SEMG signal. The wavelet based noise removal technique proposed in this research can be used for the analysis and characterization of EMG signal to understand muscle contraction significantly.

VHDL, a hardware description language, will be used to model the algorithm, which will be followed by extensive testing and simulation to verify the functionality of the algorithm that allows efficient FPGA implementation. The chip will be cost effective, portable and robust for a portable EMG related biomedical equipments.

5. References

/1/ J. V. Basmajian, C. J De Luca, "Muscles Alive - The Functions Revealed by Electromyography", The Williams & Wilkins Company, Baltimore, 1985

/2/ T. David Mewette, N. Homer, J. R. Karen, "Removing Power Line Noise from Recorded EMG", Proceedings of the 23rd annual international conference, pp 2190- 2193, Oct 25-28, Istanbul, Turkey

/3/ P. Carre, H. Leman, C. Fernandez, C. Marque, "Denoising of the uterine EHG by an undecimated wavelet transform, IEEE Trans. on Biomedical Signal Processing, vol 45, issue 9, pp 1104-1114, 1998

/4/ S. Mallat, "A wavelet tour of signal processing", 2nd edition, Academic Press, 1998, New York, USA

/5/ H. S Milner Brown., R. B. Stein, "The relationship between the surface electromyogram and muscular force", J of Physiol (Lond), vol. 246, pp 549-569; 1975

/6/ L. Lindstrom, R. Kadefors, I. Petersen, "An electromyographic index for localized muscle fatigue", J of Appl Physiol: Respirat Environ Exercise Physol, vol. 43, pp 750-754, 1977

/7/ P. W. Mark, "Wavelet-based noise removal for biomechanical signals: A comparative study", IEEE Trans. on biomedical engineering, vol 47, no. 2, pp. 360-360

/8/ M. Hagberg, B. E. Ericson; "Myoelectric power spectrum dependence of muscular contraction level of elbow flexors", Eur J of Appl Physiol, vol. 48, issue 2, pp 147-156, 1982

/9/ T. Moritani, A. Nagata, M. Muro, "Electromyographic manifestations of muscular fatigue"; Med Sci Sport Exerc; vol. 14, pp 198-202, 1982

/10/ C. J. De Luca, "Myoelectrical manifestations of localized muscular fatigue in humans; CRC critical reviews in Biomedical Engineering", vol. 11, issue 4, pp 251-279, 1985

M. S. Hussain, M. B. I. Reaz, M. I. Ibrahimy, A. F. Ismail
Dept. of Electrical and Computer Engineering,
International Islamic University Malaysia, Gombak,
53100 Kuala Lumpur, Malaysia
F. Mohd-Yasin
Faculty of Engineering, Multimedia University, 63100
Cyberjaya, Selangor, Malaysia
Tel: +603-61964435, Fax: +603-61964488, Email:
mamun.reaz@iiu.edu.my

Prispelo (Arrived): 25.05.2006 *Sprejeto (Accepted):* 15.06.2007

SENSORS FOR MEASUREMENT OF TREMOR TYPE JOINT MOVEMENTS

Samo Ribarič[1] and Janez Rozman[2]

[1] Institute of Pathophysiology, Faculty of Medicine, Ljubljana, Slovenia
[2] ITIS d.o.o. Ljubljana, Center for Implantable Technology and Sensors, Ljubljana, Slovenia

Key words: tremor; Parkinson's disease, joint movement, apomorphine, sensor

Abstract: We developed sensors for measurement of the angle of joint deflection in tremor type joint movements. Two hand tremor measuring configurations that measure hand tremor amplitude with reference to the joint involved in tremor movement were evaluated. The shape of tremor sensors could be adapted to fit the contour of a specific joint. This modification did not degrade the sensor's sensitivity or dynamic range. We conclude that this method reduces between-subjects and within-subject variability of hand tremor measurements and also locates the hand muscle groups that are most active in tremor movement thus enabling their local treatment.

Tipala za merjenje s tremorjem povzročenih gibov v sklepih

Ključne besede: tremor, Parkinsonova bolezen, gib v sklepu, apomorfin, tipalo

Izvleček: Razvili smo tipala za merjenje kota upogiba v sklepih okončin, ki ga povzroča tremor. Z meritvami tremorja v zapestju in v prstu smo preverili delovanje dveh merilnih sistemov, ki sta bila opremljena z omenjenimi tipali. Obliko in velikost merilnih sistemov smo prilagodili ergonomiji merjenega sklepa. Taka prilagoditev ni omejila občutljivosti in merilnega območja tipal. Zaključujemo, da predstavljena metoda za merjenje tremorja, v primerjavi z obstoječimi metodami, zmanjšuje variabilnost meritev tremorja roke in olajša določitev mišičnih skupin, ki so najbolj aktivne pri tremorju okončine.

1 Introduction

Tremor is a rhythmic, involuntary oscillatory movement of a body part /1/. It is characterized by tremor amplitude and frequency. Identification of a specific type of tremor requires tremor amplitude assessment during different states of the body; during rest, active movement and posture of the affected body part. With the exception of primary orthostatic tremor, tremor frequency cannot determine the type of tremor since the frequencies of many tremor types overlap. Tremor can be assessed with a variety of techniques including clinical rating scales /2,3/, multichannel calibrated accelerometry /4/, electromyography /5/, multidimensional electromagnetic systems /6,7/, video image processing /8,9/, spirography /10/ and functional performance tests /11/. Clinical rating scales for example, Unified Parkinson's Disease Rating Scale (UPDRS) or Tremor Research Group Rating Scale (TRGRS), are still the most commonly used methods for tremor assessment in the clinical setting /12/. On the one hand clinical rating scales are only semi quantitative and prone to interobserver variability, but on the other instrumental measurement methods are complex, often unavailable for ambulatory patient assessment and adapted for a specific type of tremor /12/. Instrumental methods enable an accurate (0.1 mm amplitude resolution and frequency accuracy of 0.1 Hz) /6,9/ and long term tremor assessment (24 hours or more) /4/ but still measure tremor amplitude in the same way as clinical rating scales - by measuring displacement of a body part without reference to the joint movement that is responsible for tremor movement.

All healthy people experience some normal, transient tremor during their lifetime. The most common disease related (pathological) tremors are drug induced tremor, parkinsonian tremor and tremor associated with multiple sclerosis. Parkinson's disease (PD) is a progressive degenerative disorder of the central nervous system with tremor being one of its four main features /13/. Tremor is usually contributed to Parkinson's disease (PD) if the patient has any form of pathological tremor and fulfils the UK brain bank criteria for PD /14/. Rest tremor is the most common form of tremor in PD and appears in 80-90% of PD patients. The tremor of PD is usually asymmetrical, usually starting in the fingers of one hand and spreading proximally to the wrist and forearm /15/. PD patients experience a considerable variation in tremor amplitude in time, but a patient's tremor frequency is constant. Tremor frequency in PD patients ranges from 3 to 11 Hz, but is usually between 4 Hz to 6 Hz /1/.

Dopamine replacement therapy is the most common form of PD treatment. Apomorphine is used for testing patient responsiveness to dopamine replacement therapy (apomorphine test) and for treatment of patients with advanced PD /16/. Since PD is a progressive, chronic disease, the patient's medical condition has to be regularly monitored to achieve a best possible balance between an attenuation of PD clinical signs (*e.g.* tremor) and symptoms and drug side effects. Local treatment of PD tremor, for example hand tremor, can be achieved with botulinum toxin injections /17/. This type of treatment is possible only if the muscles that contribute most to tremor movement are identified.

The objective of this study was to develop a method for hand tremor measurements in ambulatory patients with PD. To achieve this objective we tested two hand tremor measuring configurations and evaluated rest tremor in PD patients before and after treatment with apomorphine, a dopaminergic agonist.

2 Methods

Two methods were used to attach the sensors to the hand - configurations 1 and 2. In configuration 1, one end of the sensor was mounted on a rigid glove and the second end rested on a steel ring (Figure 1). The glove was made of a non-toxic, non-allergic epoxy resin for medical use. Sensors were attached to the glove with brass screws and were positioned over the steel ring with aluminum spacers (Figure 2). In configuration 2, sensors were placed directly over the measured joints and secured to the skin with a strong waterproof adhesive tape (Figure 3). Tremor sensors were designed and developed by research company ITIS d.o.o. Ljubljana, Slovenia. Each sensor was essentially a complete Wheatstone bridge consisting of four force transducers glued onto a stainless steel strip. Technical details of both sensors are summarized in Table 1.

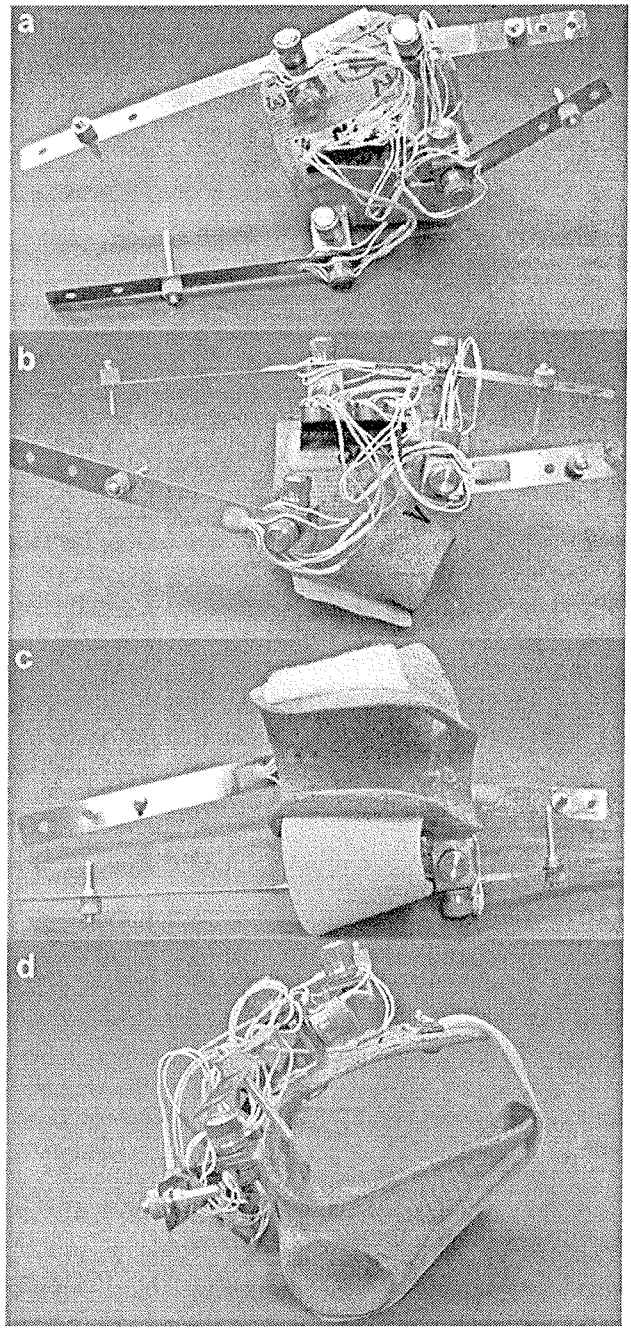

Fig. 1: Hand tremor sensor configuration 1 in four views top view (a), side views (b,c) and front view(d).

Table 1: Technical characteristics of sensors type 1 and type 2.

	type 1	type 2
sensor type	full Wheatstone bridge consisting of four force transducers	full Wheatstone bridge consisting of four force transducers
sensor material	semiconductive material	metal foil
manufacturer	Celesco, USA	Hottinger Baldwin Messtechnik GMBH, Germany
product code	P05-02-500	1-LY41-10/700
nominal resistance	500 Ω	700 Ω ± 0,3 %
conversion factor	≈ 10	2,08 ±1 %
glue for attachemnet to the steel support	Micromeasurements, USA M-bond 610	Hottinger Baldwin Messtechnik GMBH, Germany EP 250

The shape and size of tremor sensors was adjusted to fit the joint contour. Such alterations changed their mechanical properties (voltage output and resonance frequency) and required the sensors to be calibrated individually. Sensors in configuration 1 were of two types; a pair of shorter sensors for finger tremor measurement (sensors type 1A) and a second pair of longer sensors for recording wrist joint movement (sensors type 1B). In configuration 2 three sensors were essentially equal in size, shape and technical characteristics (sensors type 2B); the shape of the sensor that measured flexion-extension in the MCP joint (sensor type 2A) was adapted to fit the joint contour (top panel in Figure 2). Sensors type 1 and 2 were calibrated when mounted on the hand.

Tremor induced voltage changes in sensors were amplified by a custom designed bridge amplifier and stored on an IBM compatible PC. Analogue to digital (AD) conversion of force transducer signals (sampling rate 100 Hz) was performed by a 16-bit National Instruments data acquisition card PCI 6036e (National Instruments Corporation, Austin, TX, USA) with a voltage input range of ± 10 V. To determine sensitivity of the measuring setups we measured the common noise for type 1 and type 2 sensors.

We measured the angle of joint deflection in two degrees of freedom; during flexion-extension and abduction-adduction in wrist joint and metacarpophalangeal joint (MCP) of the 2. (index) finger. Therefore four sensors were used to measure rest tremor in each hand. Tremor sensors were

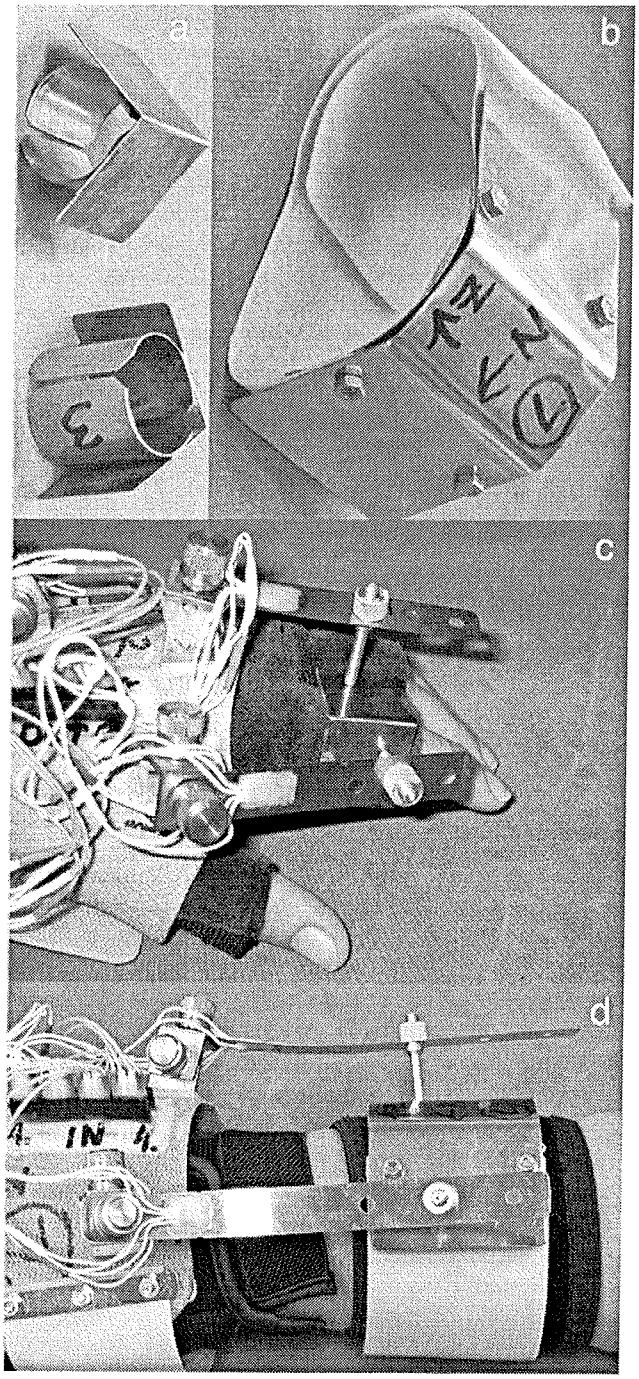

Fig. 2: Details of hand tremor sensor configuration 1: (a) steel ring for support of sensor S_{1A}, (b) steel ring for support of tremor sensor S_{1B}, close-up views of mounted tremor sensor type S_{1A}, (c) and tremor sensor type S_{1B} (d).

attached at predefined sites over the wrist and MCP joints of patients with PD. The sensor's location was inspected visually so that the sensors at the same joint were perpendicular to each other. We evaluated rest hand tremor in 5 PD patients before and after application of a tremor reducing drug (i.e. apomorphine (APO)). Only hand tremors with frequencies between 3 and 11 Hz were considered to be associated with PD /1/. An informed written consent was obtained from each patient. Patients were advised that they

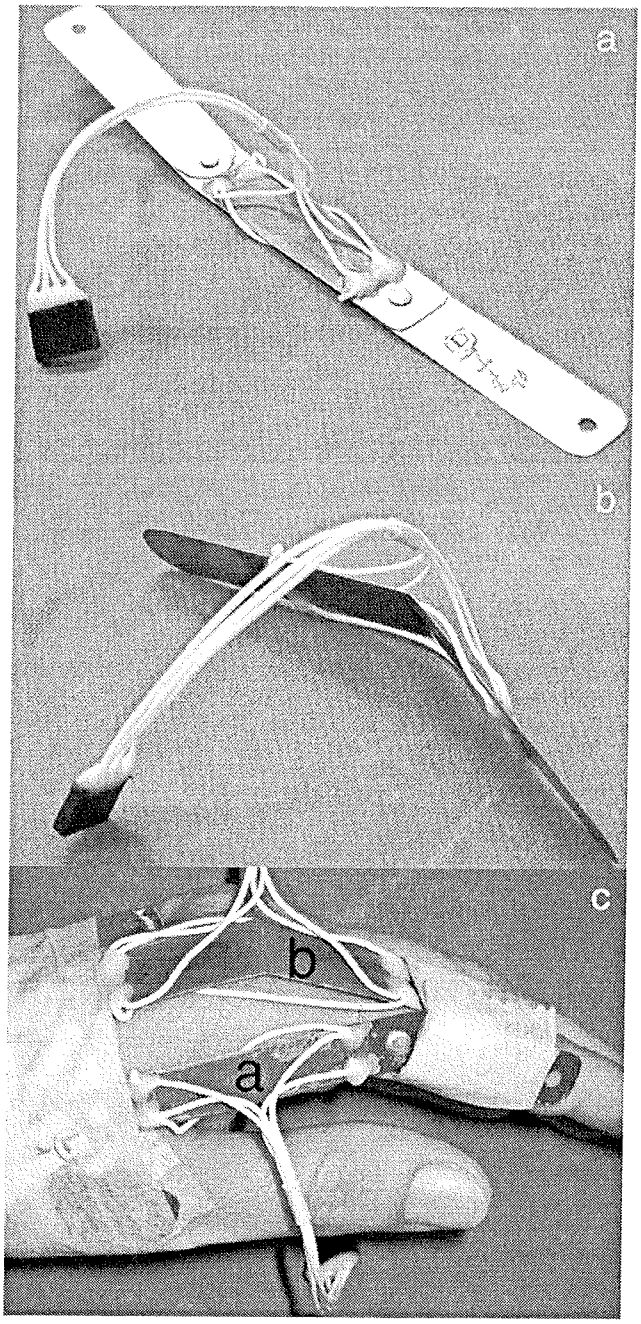

Fig. 3: Hand tremor sensors S_{2B} (a) and S_{2A} (b) in configuration 2 (c).

were free to terminate the measurements at any time, should they experience any discomfort. The study protocol was approved by the National Medical Ethics Committee of Slovenia and is in accordance with the Helsinki Declaration of 1975.

3 Results

A sensor's resonance frequency also depends on the sensor's size and shape. The resonance frequencies of sensors 1A, 1B, 2A and 2B range from 15 Hz to 47 Hz (Figure 4).

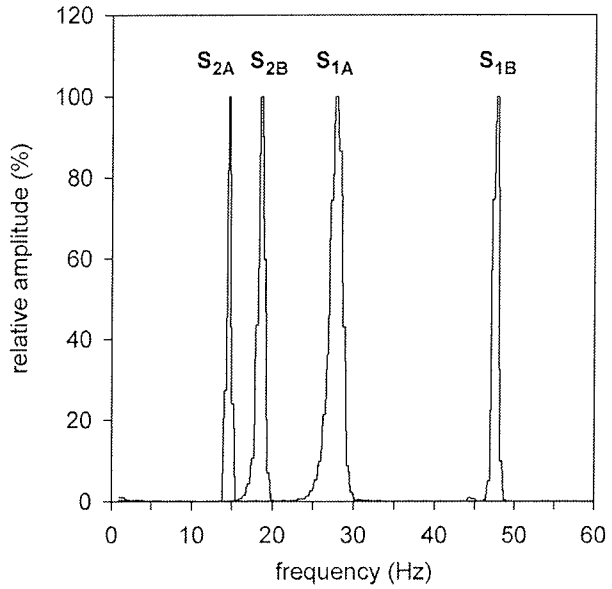

Fig. 4: Resonance frequencies of hand tremor sensors S_{1A}, S_{1B}, S_{2A} and S_{2B}.

The average common noise (five recordings) of sensors in configuration 1 and 2 is presented in Figure 5. Common noise amplitude was below 0.001 V.

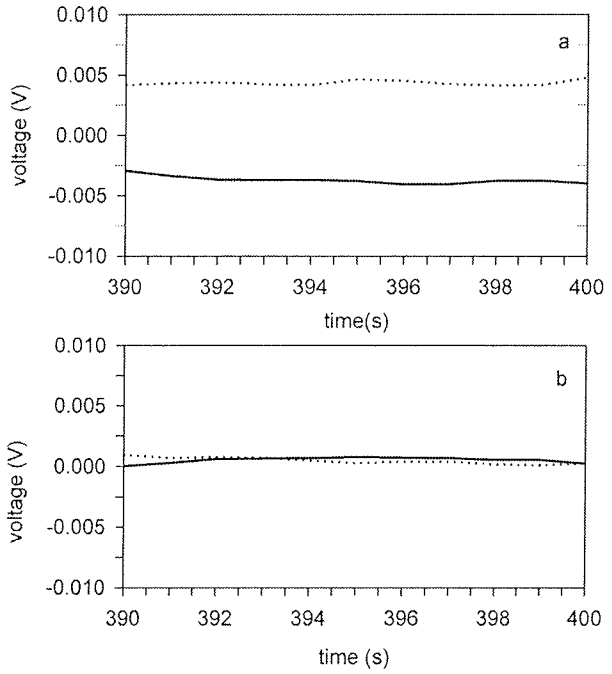

Fig. 5: Average common noise of tremor sensors 1: dotted line S_{1A}, straight line S_{1B} (a) and tremor sensors 2: dotted line S_{2A}, straight line S_{2B} (b). Each record represents an average of five measurements.

The voltage change (average of five successive measurements) in tremor sensors 1A, 1B, 2A and 2B, relative to an angle of joint deflection, is presented in Figure 6. Quadratic correlation between the angle of joint deflection and the corresponding voltage output of tremor sensors type

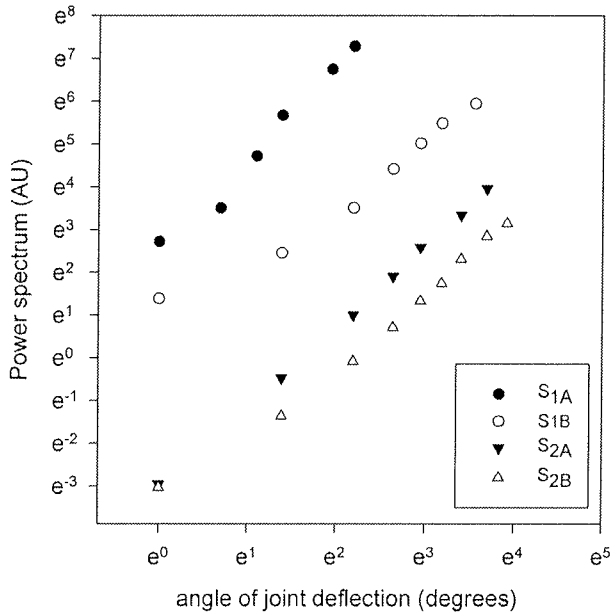

Fig. 6: Relationship between the angles of deflection and power spectra for hand tremor sensors S_{1A}, S_{1B}, S_{2A} and S_{2B}.

1 and type 2 was established by a series of joint deflections from 0.1^0 to 50^0 (Table 2).

Table 2: Quadratic curve fit of voltage changes at defined angles of joint deflection for sensors S_{1A}, S_{1B}, S_{2A} and S_{2B}. R^2 is the relative predictive power of the quadratic curve fit model. P values are the probability values that the sensors' data do not fit the quadratic curve fit model.

	$y = \beta_0 + \beta_1 x + \beta_2 x^2$				
sensor	β_0	β_1	β_2	R^2	P
S_{1A}	-6.184	-10.949	19.362	0.999	<0.001
S_{1B}	-11.829	5.047	0.188	0.990	<0.001
S_{2A}	0.039	0.034	0.032	0.998	<0.001
S_{2B}	-0.261	0.079	0.008	0.994	<0.001

Congruence between the observed hand tremor amplitude and calculated hand tremor amplitude (calculated from power spectra of tremor induced voltage changes) was evaluated by simultaneous visual and instrumental measurements of wrist hand tremor in 5 patients with PD. The results of this evaluation are presented in Figure 7. The observed and calculated TRGRS (calculated from power spectra of tremor sensor voltage changes due to wrist joint movement) were in a perfect linear correlation (R^2=1).

A typical example of a time course of hand tremor amplitude in the wrist joint and finger joint after APO application is shown in Figure 8.

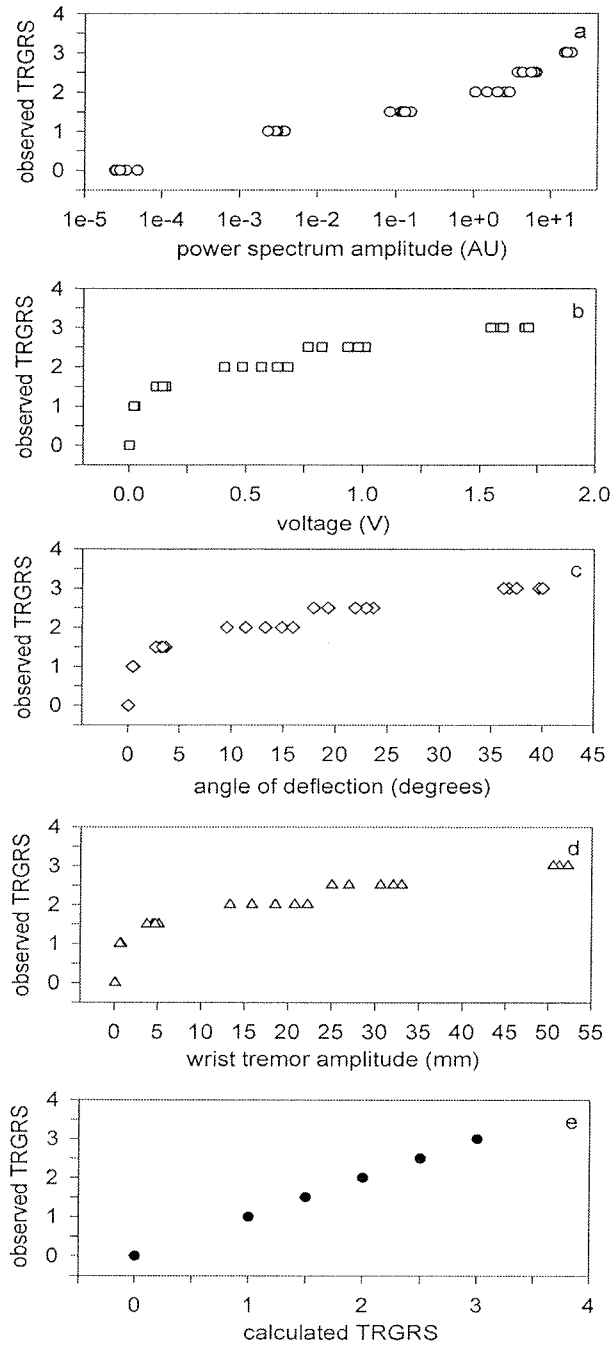

Fig. 7: Relationship among the observed TRGRS and calculated power spectrum amplitude (a), tremor induced voltage change (b), angle of wrist joint deflection (c), wrist tremor amplitude (d) and calculated TRGRS (e) in five patients with Parkinson's disease. The observed and calculated TRGRS (calculated from power spectra of tremor sensor voltage changes due to wrist joint movement) are in a perfect linear correlation. TRGRS scale: 0 = tremor not observed on visual inspection, 1 = tremor barely observed; 1.5 = tremor amplitude below 10 mm; 2 = tremor amplitude 10 - 29 mm; 2.5 = tremor amplitude 30 - 49 mm; 3 = tremor amplitude 50 - 99 mm; 3.5 = tremor amplitude 100 - 199 mm.

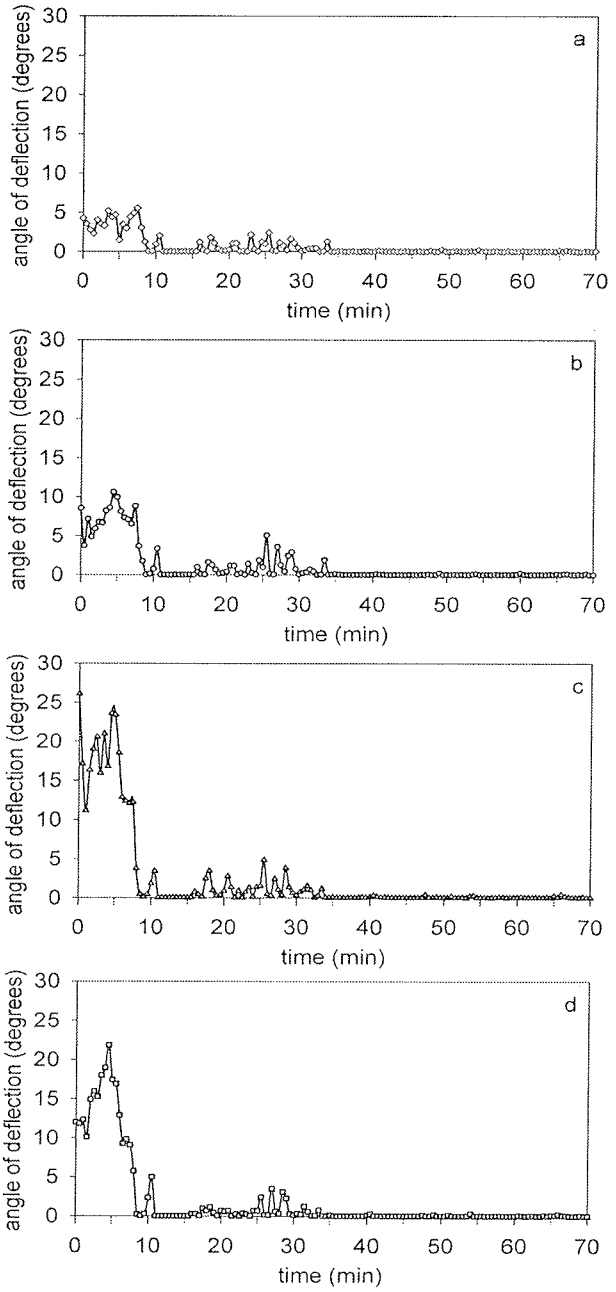

Fig. 8: Time course of hand tremor amplitude of a patient with PD after application of the tremor reducing drug APO. The angle of deflection was measured: in the metacarpophalangeal joint of the index finger (flexion-extension in graph a; abduction-adduction in graph b) and in the wrist joint (flexion-extension in graph c; abduction-adduction in graph d). Each data point on graphs a to d represents an average angle of deflection during a 30 s time window. The patient received APO at t = 0 min.

4 Discussion

We developed and tested two hand tremor measuring configurations (1 and 2) that measure hand tremor amplitude

with reference to the joint involved in tremor movement, thus reducing between-subjects and within-subject variability of hand tremor measurements. Tremor sensors in configuration 1 had a higher resonance frequency than in configuration 2. Therefore configuration 1 sensors can measure all types of tremor including primary orthostatic tremor with a frequency of up to 20 Hz /1/. The average rest tremor frequency in our PD patients was 4.5 ± 0.3 Hz (average ± SD). Tremor frequency in patients with PD is constant, usually between 4 and 6 Hz, and exceptionally up to 11 Hz /1/. Therefore the resonance frequency of type 1 and type 2 sensors did not interfere with tremor evaluation in PD patients. The typical upper frequency range of most tremors, with the exception of primary orthostatic tremor, is below 12 Hz; therefore, as far as sensor resonance is concerned, sensors in configuration 2 are appropriate for measurement of most types of hand tremor. Compared to tremor sensors in configuration 2, tremor sensors in configuration 1 gave a higher voltage output for a given angle of deflection. This was due to a relatively high degree of sensor bending in configuration 1, to adapt the sensor shape to a specific hand contour. Configuration 2 had two major advantages over configuration 1: (i) a smaller voltage output for a given angle of deflection enables measurement of large angles at the same voltage input settings (± 10 V) of an AD data acquisition board and (ii) hand tremor measurements were not impeded by variations in hand size. In patients with large or small hands it was difficult to ensure a good fit with sensors in configuration 1.

Hand tremor amplitude was evaluated by tremor sensors and clinically with the TRGRS. Both methods were in agreement (Figure 7) when assessing APO induced hand tremor changes; the observed and calculated TRGRS were in a perfect linear correlation. The presented hand tremor sensors can measure the changes in hand tremor amplitude over time. Figure 8 shows the changes in finger and wrist tremor amplitude after APO application during a 70 min time window.

Tremor assessment methods can measure clinically undetectable tremor /6,7,8,9/. The presented force transducer tremor evaluation method can also measure clinically undetectable tremor in PD patients. The absolute limit of the method's sensitivity is determined by the common noise amplitude which is one order of magnitude smaller than the smallest calibrated sensor output voltage amplitude.

Multidimensional evaluations are recommended for assessment of tremor severity in clinical trials /15/. Electromagnetic devices can track motion with six degrees of freedom (translational and rotational) /7,8/. The presented force transducer method measures joint movement with two degrees of freedom and provides an effective, simple and low cost alternative to multidimensional electromagnetic devices /6,7/ or 3D video tremor evaluation methods /8,9/ for hand tremor evaluation in PD patients.

The shape of a force transducer tremor sensor can be adapted to fit the contour of a specific joint (Figure 2,3). This modification does not degrade the sensor's sensitivity or dynamic range but does require recalibration (Figure 6).

5 Conclusions

We developed and tested a tremor evaluation method that measures hand tremor amplitude with reference to the joint involved in tremor movement. This method reduces between-subjects and within-subject variability of hand tremor measurements and also locates the hand muscle groups that are most active in tremor movement thus enabling their local treatment.

6 Acknowledgements

This work was supported by the Ministry of Higher Education, Science and Technology, Republic of Slovenia, under research programme P3-0171. The authors thank Professor Zvezdan Pirtošek, Andrej Bartolić, MD, and Nurses Lidija Ocepek and Zdenko Garaševič at the Dept. of Neurology, Ljubljana University Medical Centre for their assistance.

7 References

/1/ G. Deuschl, P. Bain, M. Brin, Consensus statement of the movement disorder society on tremor, Mov. Disord., 13suppl(3) (1998) 2-23.

/2/ P. Martinez-Martin and M. J. Forjaz, Metric attributes of the unified Parkinson's disease rating scale 3.0 battery: Part I, feasibility, scaling assumptions, reliability, and precision, Mov. Disord., 21(8) (2006) Aug 1182-1188.

/3/ M. J. Forjaz and P. Martinez-Martin, Metric attributes of the unified Parkinson's disease rating scale 3.0 battery: part II, construct and content validity, Mov. Disord., 21(11) (2006) 1892-1898.

/4/ T. Thielgen, F. Foerster, G. Fuchs, A. Hornig, J. Fahrenberg, Tremor in Parkinson's disease: 24-hr monitoring with calibrated accelerometry, Electromyogr. Clin. Neurophysiol., 44 (2004) 137-146.

/5/ F. Foerster and M. Smeja, Joint amplitude and frequency analysis of tremor activity, Electromyogr. Clin. Neurophysiol., 39 (1999) 11-19.

/6/ J. M. Spyers-Ashby, M. J. Stokes, P. G. Bain, S. J. Roberts, Classification of normal and pathological tremors using a multidimensional electromagnetic system, Med. Eng. Phys., 21 (1999) 713-723.

/7/ P. E. O'Suilleabhain and R. B. Dewey Jr., Validation for tremor quantification of an electromagnetic tracking device, Mov. Disord. 16(2) (2001) 265-271.

/8/ M. Swider, The application of video image processing to quantitative analysis of extremity tremor in humans, J. Neurosci. Methods, 84 (1998) 167-172.

/9/ R. Wenzelburger, J. Raethjen, K. Loffler, H. Stolze, M. Illert, G. Deuschl, Kinetic tremor in a reach-to-grasp movement in Parkinson's disease, Mov. Disord., 15(6) (2000) 1084-1094.

/10/ S. L. Pullman, Spiral analysis: A new technique for measuring tremor with a digitizing tablet, Mov. Disord., 13(3) (1998) 85-89.

/11/ P. G. Bain, Clinical measurement of tremor, Mov. Disord., 13(3) (1998) 77-80.

/12/ W. G. Bradley, editor, Neurology in clinical practice, Philadelphia: Butterworth-Heinemann, (2004) 302-306.

/13/ C. Frank, G. Pari, J. P. Rossiter, Approach to diagnosis of Parkinson disease, Can. Fam. Physician, 52 (2006) 862-868.

/14/ A. J. Hughes, S. E. Daniel, S. Blankson, A. J. Lees, A clinicopathologic study of 100 cases of Parkinson's disease, Arch. Neurol., 50(2) (1993) 140-148.

/15/ P. G. Bain, L. J. Findley, P. Atchison, M. Behari, M. Vidailhet et al., Assessing tremor severity, J. Neurol. Neurosurg. Psychiatry, 56 (1993) 868-873.

/16/ J. C. Sharma, L. Macnamara, M. Hasoon, M. Vassallo, Diagnostic and therapeutic value of apomorphine in Parkinsonian patients, Int. J. Clin. Pract., 58(11) (2004) 1028-1032.

/17/ R. M. Trosch and S. L. Pullman, Botulinum toxin A injections for the treatment of hand tremors, Mov. Disord., 9(6) (1994) 601-609.

Samo Ribarič
Institute of Pathophysiology, Faculty of Medicine,
Zaloška 4, SI-1000 Ljubljana, Slovenia
Tel.: +386 1 5437053, Fax.: +386 1 5437021,
E-mail: samo.ribaric@mf.uni-lj.si

Janez Rozman
ITIS d.o.o. Ljubljana, Center for Implantable Technology and Sensors, Lepi pot 11, SI-1001, Ljubljana, Slovenia

Prispelo (Arrived): 26.01.2007 *Sprejeto (Accepted):* 15.06.2007

USING OEE APPROACH FOR IMPROVING MANUFACTURING PERFORMANCE

Robert Ferko[1], Alenka Žnidaršič[2]

[1]Droga Kolinska d. d., Ljubljana, Slovenija
[2]Metronik d.o.o., Ljubljana, Slovenija

Key words: Performance measurement, Manufacturing improvement, Key performance indicators, Overall Equipment Effectiveness

Abstract: Competition and the drive for profit are forcing manufacturing companies to introduce different approaches for improving performance. Because of its holistic view, the Overall Equipment Effectiveness (OEE) approach is the best for managing operations in the context of cost and efficiency-focused manufacturing, while it gives managers the information where the equipment is loosing time. In this paper, the concepts of OEE approach together with the implementation framework are presented. OEE accepted as a key performance indicator and benchmark measure in several machine and asset-intensive industries, like semiconductor, electronics, pharmaceutical or food industry.

We can conclude from our experiences working with industry, that OEE is a very good measure for monitoring manufacturing performance if all key parameters are calculated automatically in real time directly from process data. This requirement can be fulfilled by using information technologies (IT), which provide process equipment connectivity. Using proper IT support, OEE approach provides systematic analysis of equipment utilisation, efficiency and quality. By continuous real-time OEE monitoring and prompt actions, management can drive the factory towards excellence in operational performance and lower production costs.

In the article, a conceptual framework for OEE is introduced using a systematic approach with information technology as an enabler. Based on literature and practical examples, the implementation life-cycle is discussed and critical success factors are outlined. OEE results are interpreted through an example of a packaging line over a one-week working period. Finally some important aspects of an OEE implementation are outlined and as a conclusion, the benefits of using OEE in manufacturing companies are described.

Izboljševanje proizvodne učinkovitosti s spremljanjem skupne učinkovitosti OEE

Ključne besede: Merjenje učinkovitosti, Izboljševanje proizvodne učinkovitosti, Ključni indikatorji proizvodne učinkovitosti, Skupna učinkovitost

Izvleček: Večina proizvodnih sistemov v praksi izvaja proizvodne procese pod pričakovanimi. Pogosto obratujejo z manjšim obsegom proizvodnje, nižjo produktivnostjo in višjimi stroški. Ker so proizvodna podjetja nenehno pod pritiskom po stalnem zviševanju proizvodne učinkovitosti, so se prav v proizvodnem okolju izoblikovale številne managerske metode oziroma pristopi za povečevanje kakovosti in produktivnosti. Ena izmed tovrstnih pristopov je tudi izračunavanje in spremljanje celovita učinkovitost opreme OEE, ki obravnava (učinkovitost) proizvodne opreme na osnovi izračunavanja razpoložljivosti, zmogljivosti in kakovosti. Ta pristop je zelo razširjen v visoko-intenzivnih avtomatiziranih industrijskih panogah, med katere sodijo elektronska industrija, živilska industrija, farmacija in druge.

Iz lastnih izkušenj lahko povzamemo, da je OEE zelo dobro merilo za spremljanje učinkovitosti proizvodnega procesa ob pogoju, da se ključni podatki izračunavajo v realnem času. To zahtevo je mogoče izpolniti z uporabo informacijskih tehnologij, ki zagotavljajo povezavo s proizvodnimi napravami. Ob ustrezni informacijski podpori, OEE metodologija zagotavlja transparentno obravnavo vzrokov za neučinkovitosti in na tak način predstavlja dobro orodje proizvodnemu managementu za sprejemanje ukrepov v smeri večje učinkovitosti tako proizvodne opreme kot celotne tovarne.

V prispevku je predstavljen konceptualen okvir, ki odgovarja na vprašanje, kako se na standardiziran (sistematičen) način lotiti obvladovanja (ne)učinkovitosti in kako pri tem čim bolj učinkovito uporabiti informacijske tehnologije. Na osnovi strokovne literature in primerov iz prakse so opisane ključne točke implementacije, ki podjetjem zagotavljajo rezultate. V zaključku bodo predstavljeni tudi učinki, ki jih proizvodna podjetja lahko dosežejo z uporabo opisanega pristopa.

1. Introduction

Recent trends indicate that many manufacturing processes are not performing as intended, so far as cost effectiveness in terms of their operation and support is concerned. They often operate at less than full capacity, with low productivity, and the costs of producing products are high. To manage the manufacturing (operational) performance, different approaches can be used. Among them, Overall equipment effectiveness (OEE) derived from Total Productive Maintenance (TPM) /14,2/ is considered as most widely used set of performance metrics to analyse the efficiency of a single machine or an integrated manufacturing system (Hansen, 2001). It provides the answer how well the manufacturing equipment is running compared to the ideal plant.

OEE is a function of availability (operating rate), performance rate, and quality rate. The three dimensions are measures of the equipment losses. Nakajima (1988) defined six major loss categories: i.e. breakdown losses, set-up and adjustment losses, minor or idling stoppage losses, reduced speed losses, defect or rework losses and start-up losses, that have direct impact on manufacturing performance and consequently also to operational costs. By reducing or eliminating losses, the management is able to maximise productivity and optimise operational costs.

OEE is especially suitable for equipment-intensive manufacturing where capacity utilisation is a high priority and downtimes are expensive in terms of lost capacity /9/ . Because of its holistic view, OEE is the best for managing operations in the context of cost and efficiency-focused manufacturing, while it gives managers the information where the equipment is loosing time. It is a way to benchmark and provide a quantitative feedback on equipment efficiency. The biggest enabler for getting OEE accepted as a management tool in practice is the development of highly automated production equipment and IT technologies, which enable automatic data collection, such as downtime events, scrap, etc. and leading to the OEE calculation in real time.

As reported by MESA International, OEE is accepted as one of the standard KPI (i.e. Key Performance Indicator) for benchmarking in several machine and asset-intensive industries, such as electronics equipment, semiconductor, medical device, pharmaceutical, food and automotive. In 2001 SEMATECH, the consortium of semiconductor manufacturers, reported that the relative importance of OEE improvement in semiconductor industry has grown significantly and is expected to require 9-15% increment per year in order to stay on the productivity curve /10/. It was noted, that the complete semiconductor industry must move toward highly efficiently factories. A major effort already underway for OEE improvements has been done in collaboration with SEMI (Semiconductor Equipment and Materials International) and resulted in creation of several guidelines and standards (e.g. E10, E79). Based on OEE research conducted by Leachman /7/, SEMI issued a revised standard for measurement of overall equipment efficiency for semiconductor industry /11/.

While machine and assets-intensive industries have used this metric for quite some time, now managers in discrete industries are adopting it (modify it) by making it less equipment specific and introducing labour and assembly operations, OEE becomes more plant-wide representing Overall Factory Effectiveness /6/.

The paper is organized as follows. First a definition of the OEE metrics is given, then it is explained how OEE can be used for driving manufacturing improvements. The third section will present the framework for OEE implementation. At the end, some open questions about OEE approach implementation will be discussed and conclusions will be given.

2. About OEE approach

OEE is a very simple set of metrics to indicate the current status of a manufacturing process and also a complex tool allowing managers to understand the effect of the various events in the manufacturing process. Although OEE is seen to be defined as standard metrics, it still requires further modification on classification of losses. A number of authors have written about the definition and measurement of OEE /5,8/. Dal et al. /3/ described that OEE appears differently in various OEE literatures because the levels of OEE measurement and the factors affected are different in various business sectors and industries. Thus, a customized OEE in different industries or business sectors is required. The standard OEE metrics background is described in the following section.

2.1 OEE metrics definition

From the OEE point of view, the equipment efficiency is lower than the expected full potential, because of equipment availability and utilization losses: such as breakdowns, setup and adjustments (i.e. downtime losses), speed losses, small stops, idling (i.e. performance losses) and product scrap, low product yields (i.e. quality losses). The role of management is to maximise effective operating time for each single piece of equipment while at the same time reducing or eliminating losses /6/.

The basis for OEE calculation is scheduled operating time which indicates the overall time scheduled for production without time for breaks, lunch, planned preventive maintenance or periods, where there is nothing to produce. The effective operating time is then calculated from scheduled operating time as represented graphically in Figure 1.

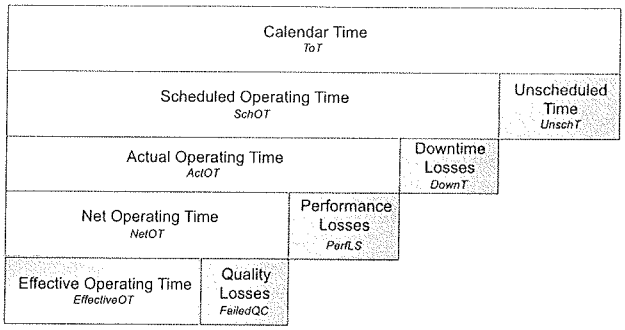

Fig. 1: Schematic representation of Effective Operating Time calculation

The impact of different types of losses to manufacturing performance of a single piece of equipment is measured through calculating its **Operating rate**, **Performance rate** and **Quality rate** /4/.

Operating rate or **Availability** (in %) quantifies equipment downtime and operating time. Downtime loss includes any event that stops planned production for an appreciable length of time. Examples include equipment failures, material shortages, and changeover time. They can be classified as planned (e.g. set-up or changeover time) or unplanned (e.g. equipment failures). Operating rate is calculated as follows:

$$Or(\Delta T) = \frac{SchOT(\Delta T) - DownT(\Delta T)}{SchOT(\Delta T)} = \frac{ActOT(\Delta T)}{SchOT(\Delta T)} \quad (1)$$

where $DownT(\Delta T)$ is referred to the total time that equipment is not available for production and $SchOT(\Delta T)$ to scheduled operating time, both calculated for observed production time period ΔT.

Performance rate (in %) takes into account speed loss, which include any factor that cause the equipment to operate at less than the maximum possible speed, when running. Examples include machine wear, poor materials and operator inefficiency. Performance rate is calculated as follows:

$$\mathrm{Pr}(\Delta T)=\frac{Mp(\Delta T)}{ActOT(\Delta T)\cdot NomCp(\Delta T)} \qquad (2)$$

where $Mp(\Delta T)$ is referred to total production in observed time, $ActOT(\Delta T)$ to actual operating time and $NomCp(\Delta T)$ to nominal equipment capacity, all calculated for observed production time period ΔT.

Quality rate (in %) is a measure of process yield, determining the amount of product that meets quality requirements the first time without adjustments, recycles and so on. It is calculated as follows:

$$Qr(\Delta T)=\frac{Mp(\Delta T)-FailedQC(\Delta T)}{Mp(\Delta T)} \qquad (3)$$

where $Mp(\Delta T)$ is the total production in observed time and $FailedQC(\Delta T)$ the quantity of scrap and rework (product). The measurement of quality losses is restricted to quality losses that are immediately recorded.

The calculation of basic equations defined by (1), (2) and (3) is simple for equipment which is designed to execute only one operation. For cases, when two or more operations can be executed on one type of equipment sequentially or in parallel, the observed parameters for all operations considering relationships factors are aggregated in a separate equation /7/.

Overall equipment effectiveness (in %)

To combine all three measures, the metrics for calculating overall performance (OEE) of a single piece of equipment (i.e. machine or line) is defined as:

$$OEE(\Delta T)=Or(\Delta T)\cdot \mathrm{Pr}(\Delta T)\cdot Qr(\Delta T) \qquad (4)$$

where ΔT is referred to the observed production time period. As such, OEE is measured in percentages (%) and indicates the overall equipment effectiveness. In addition to the basic formula, some authors /2/ argue to use different weights for factors Or, Pr and Qr, while they are not equally important in all industry sectors. Weighted OEE metrics is defined as follows:

$$OEE(\Delta T)=w_1\cdot Or(\Delta T)\cdot w_2\cdot \mathrm{Pr}(\Delta T)\cdot w_3\cdot Qr(\Delta T) \qquad (5)$$

where w_i, $0 < w_i \leq 1$ represents the importance weights for each individual OEE parameter.

Overall factory effectiveness (in %)

OEE metrics defined by equations (4) and (5) are about achieving excellence in individual equipment. However, successful analysis of individual machine OEE's only is not sufficient, as no machine is isolated in a factory, but operates in a linked and complex environment. Overall factory effectiveness (OFE) is about combining activities, the relationships between different machines and processes, integrating information, and the decisions and actions across many independent systems and sub-systems. Several different approaches to OFE can be found in the literature / 6/. The most common and simple ones are **straight average** and **weighted average methods**.

Using straight average method, OFE metrics for the entire plant is calculated as a product of average values for Or, Pr and Qr as follows:

$$OFE(\Delta T)=\frac{\sum_{i=1}^{N}Or_i(\Delta T)}{N}\cdot\frac{\sum_{i=1}^{N}\mathrm{Pr}_i(\Delta T)}{N}\cdot\frac{\sum_{i=1}^{N}Qr_i(\Delta T)}{N} \qquad (6)$$

where N is the total number of equipment with OEE measuring.

Weighted average method is using weights for separate piece of equipment and it is calculated as follows:

$$OFE(\Delta T)=\frac{\sum_{i=1}^{N}w_i\cdot Or_i(\Delta T)}{\sum_{i=1}^{N}w_i}\cdot\frac{\sum_{i=1}^{N}w_i\cdot \mathrm{Pr}_i(\Delta T)}{\sum_{i=1}^{N}w_i}\cdot\frac{\sum_{i=1}^{N}w_i\cdot Qr_i(\Delta T)}{\sum_{i=1}^{N}w_i} \qquad (7)$$

The weights can be set-up using plant production time, equipment importance for production, etc. Both approaches for OFE calculation do not include information on different types of equipment connections and dependencies. More sophisticated approaches incorporate also a so called equipment coordination factor /6/. Because of their complexity, these approaches are not widely used in practice.

The fundamental concept of OEE is not new. By evolution of new production management strategies, such as lean manufacturing /13/ along with high-technology production equipment and developments in information technology (IT), the OEE principles are finding wider application in the industry.

3. OEE implementation

OEE implementation is connected with two important issues: how to use OEE as a management tool and how to get accurate data for OEE metrics calculation. The sec-

ond issue is covered by using appropriate IT, while the first one has a business context.

3.1 OEE as a management tool

OEE approach concentrates around activities needed for systematic improvement of production equipment and consequently business results. There are several ways, how managers can use it as a business tool. The most common way is to use OEE as a systematic approach to run actions for improving manufacturing performance. Quite often, the OEE indicator is also used for benchmark purposes and to drive business decisions /9/.

a. OEE as a systematic approach to run (continuous) actions for improving manufacturing performance

The main objective to measure OEE is to make constraint or bottleneck equipment run more efficiently. OEE and its individual factors can provide managers real-time information to see where the equipment is loosing performance, i.e. if it has much downtime or speed losses or if the quality is poor. If the OEE score is below an acceptable benchmark, the analysis of its three components can direct the attention of managers toward downtime and other indicators of poor performance, determine their causes and rectify them. Downtimes are associated to categories, therefore reasons and sub-reasons have to be associated. In this way, the manager is able to properly analyze downtime categories. The managers' focus should not be on a snapshot for a single day, but rather to monitor the trends in real time and see if improvement efforts actually make the equipment run more effectively.

b. OEE for benchmarking

Managers can use OEE indicator to benchmark or analyze it across similar plants to identify best practices /3/. By comparing the historical and current index against these benchmarks, managers can gain valuable insights into the effectiveness of their capital assets (production equipment), identify bottlenecks and make investment decisions.

According to the literature /9/ the average OEE (ΔT) score for production plants is approximately 60% and the best OEE (ΔT) is generally considered to be 85% for batch and discrete production plants ($Or \geq 95\%$, $Qr \geq 95\%$ and $Pr \geq 95\%$) and even 95% for continuous ones /1/.

c.OEE for supporting business decisions

OEE can be used with financial metrics such as return on capital employed (ROCE), to make decisions on whether to keep a plant open, close it, invest in it, or consolidate it with another operation /3/.

In all three cases, input data quality for calculating OEE metrics is the most critical factor to accept OEE approach as a management tool that brings results. Traditional approach to OEE is based on manual data entry of downtime events by operators into a specialised software application. This approach does not guarantee complete and accurate input data. The evolution of high-technology production equipment and IT development bring the so called "bottom-up" approach centred on raw process data acquired from process control equipment or SCADA systems /12/. By using specialized OEE software products, which leverages modern technology for real-time data collection, raw process data are automatically evaluated based on predefined fault models and OEE metrics are calculated and displayed to the managers. The specialized OEE solution providers are mainly global companies developing software for process automation and control, such as GE Fanuc and Siemens. The main strength of this approach is that all required data are acquired automatically from the process in real time and can provide also automatic reasoning about downtime causes.

3.2 Implementing OEE using information technologies

Implementing OEE using IT technologies is considered as a classical software-project approach with its own life cycle. The major stages are the following:

- **Requirements and system analysis.** Each OEE project starts with the requirements definition and extensive analysis from the equipment and efficiency point of view.
- **Downtime modelling.** Based on requirements and analysis, downtime model for each production component (under OEE study) is defined. The downtime model represents the relations between observed raw process data, downtime events and the root cause (or causes) of downtime. The relations can be expressed in terms of expert rules or decision AND-OR trees, or by using other known modelling techniques (for example qualitative modelling approach). The model complexity increases in case of more interconnected devices, while their interdependence represents another dimension of the model. It is important to realise, that the accuracy and completeness of the downtime model plays a key role in correct downtime detection and classification.
- **OEE system specification and design.** The purpose of the specification and design phase is to propose a complete solution to the OEE by taking into account the aspects investigated in the previous stages, which is feasible for implementation.
- **Implementation.** Implementation is often done by using specialized configurable and modular OEE software products, which covers the following functional segments:
  a. **Process data collection.** Standard interface for automated production equipment, i.e. a single machine or production line, provides automated collection of raw process data to process historian in real-time. Examples of raw process data are equipment operating condition (i.e. produc-

tion line is working, production line is stopped, etc.), initial and end time of downtime, downtime location, produced product quantity, scrap, etc.

b. **Downtime detection.** Using raw process data, pre-defined downtime models are evaluated in a real-time. Downtime events are stored to the relational data base automatically together with the time stamps for start and end.

c. **Classification.** First, OEE system tries to identify the root cause (or causes) for downtime automatically from the model. If not possible, the operator is able to define it manually based on pre-defined list of possible causes. This task can be done through a specialized application clients installed in the production floor. One example of such OEE production client can be seen at Figure 2.

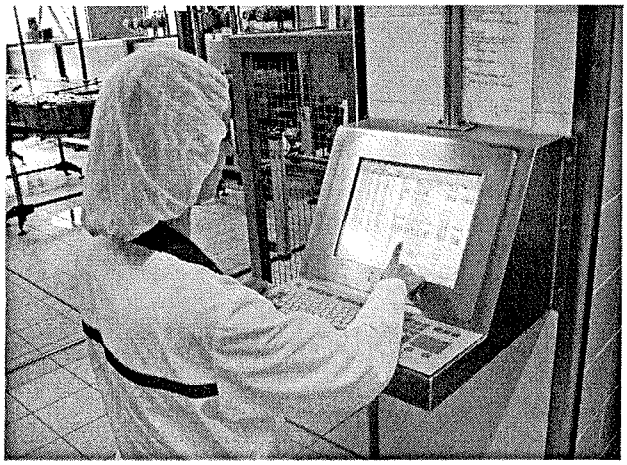

Fig. 2: OEE production client

d. **OEE metrics calculation.** Based on evaluated downtime events, data about produced products and scrap, OEE parameters are calculated along with the OEE metrics automatically. The calculation is triggered by an event, which is often production order start and production order end. These events are triggered manually by the operators or automatically by appropriate electrical signal, captured automatically from production line.

e. **OEE visualisation and analysis.** OEE indicators together with three separate parameters *Operating rate*, *Performance Rate* and *Quality rate* are displayed in a way to be understood by production managers in real time. The downtime analysis enables them to explore the causes that have generated production efficiency losses. In such a way, managers are able to understand where the factory bottlenecks are and which are the real downtime reasons, and allow them to react accordingly. Often, OEE monitoring is performed using web application client or modern communication devices such as GSM, PDA etc. One example of such OEE visualisation client can be seen at Figure 3.

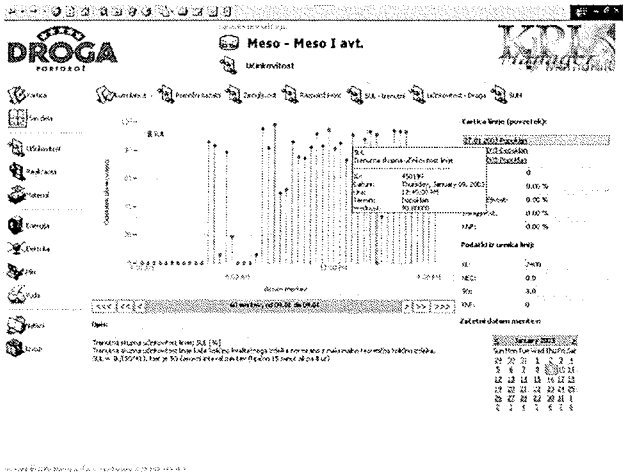

Fig. 3: OEE visualisation client

Such specialised OEE software product also fulfils IT requirements for reliability, scalability, ease-of-administration, security and low cost of ownership.

- **Maintenance.** Maintenance of OEE system is an unavoidable step in the cycle since any technological change to the production process equipment might involve the redesign of some parts of the OEE solution.

3.3 OEE interpretation through an example

To illustrate OEE concept, consider a packaging line for soft drinks scheduled to operate in two or three shifts starting at 6:00 a.m. Process data are collected and evaluated automatically with time period of 15 minutes. Downtime events are stored in a relational database together with identified the root cause (or causes) for downtime. As an example for downtime set records, the sample for a single day is shown in Table 1.

From industry practice, monitoring OEE per shift to improve operational shift performance shows good results. Therefore, operating rate, performance rate and quality rate are calculated along with the OEE metrics automatically per working shift. The OEE results for a week-time period are shown in Figure 4. The results show that the overall efficiency for packaging line goes from maximum 75% to lower values, while the average value is 35%. Figure 5 shows in detail all three parameters governing the OEE. The average value of performance rate *Pr* (40%) lead us to conclusion that only 40% of time was spent on actual production.

The analysis of *Or*, *Qr* and *Pr* results (Figure 5) can give us the a detailed interpretation for poor performance of this packaging line.

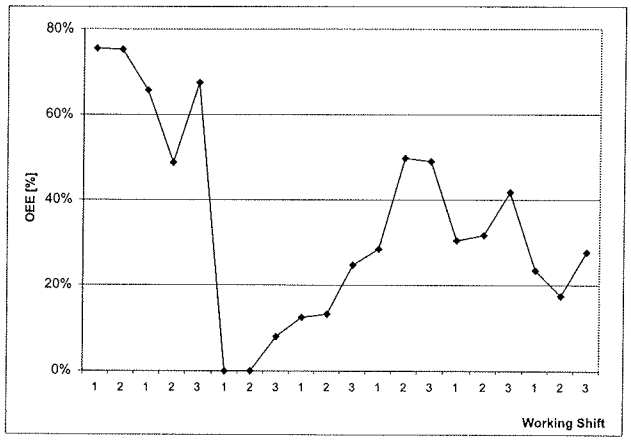

Fig. 4: OEE trends for packaging line calculated per shift in a week

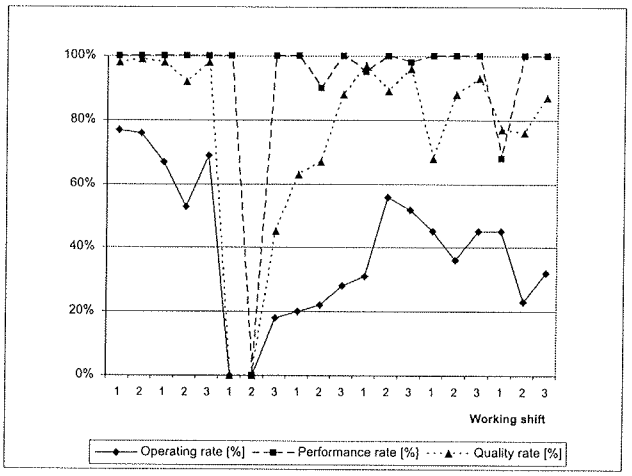

Fig. 5: Or, Qr and Pr results for OEE shown on Figure 4

Looking at the performance rate (*Or*) trend line, the value reaches zero during the third day. To analyse deeper, downtime records show that stoppage of packaging line was planned because of the product change. Changeover took time of two working shifts. Then production continued with the start-up phase and equipment tuning after it has been restarted. In this phase, the scrap quantity increased, while several short line stoppages caused by tuning resulted in low operational rate.

Further more, it can be seen from Figure 5 that the first two working days performance rate was higher than the last ones. Again, downtime analysis shows (see Table 1) that breakdowns of supporting systems and machine failure were the main reason for poor performance.

The overall performance rate trend shows that the total downtime (scheduled and not-scheduled) for packaging line is relatively big. This packaging line was not operational because of several not-scheduled reasons at average 2.4 hours per day, which can be classified in the following categories: problems between production (organizational problems), supporting systems breakdown, material shortage, machine failure, short automatic stops and not defined events. The Figure 6 shows which categories of downtimes had impact on operational performance discussed in this section. Product change (37%) and short automatic stops (30%) dominate among the downtime categories.

Table 1 One day sample of downtime records (the 6th day from Fig. 4 or 5)

Downtime	Total duration (min)	Error	Type
01-Product change	65,45		
08:43:57	26,88	116-Operator manual stop	scheduled
14:19:32	18,17	0001-Line is stopped	scheduled
15:06:53	17,40	0001-Line is stopped	scheduled
02-Loading	24,80		
08:16:52	2,02	0001-Line is stopped	scheduled
13:05:31	3,78	0001-Line is stopped	scheduled
03-Control procedure	10,38		
07:20:57	0,97	0001-Line is stopped	scheduled
10:44:34	3,42	0001-Line is stopped	scheduled
04-Problems between production	32,07		
08:08:13	0,22	0001-Line is stopped	non-scheduled
10:48:11	6,77	0001-Line is stopped	non-scheduled
11:48:00	12,42	112-Short disturbance	non-scheduled
07-Supporting systems breakdown	62,00		
05:45:23	14,60	0001-Line is stopped	non-scheduled
06:00:00	35,43	0001-Line is stopped	non-scheduled
99-Machine failure	65,54		
07:22:30	3,35	052-Filling machine	non-scheduled
07:27:06	1,15	052-Filling machine	non-scheduled
07:30:30	1,33	113-Tetra TOP machine is stopped	non-scheduled
07:32:36	0,67	113-Tetra TOP machine is stopped	non-scheduled
07:42:40	6,70	116-Operator manual stop	non-scheduled

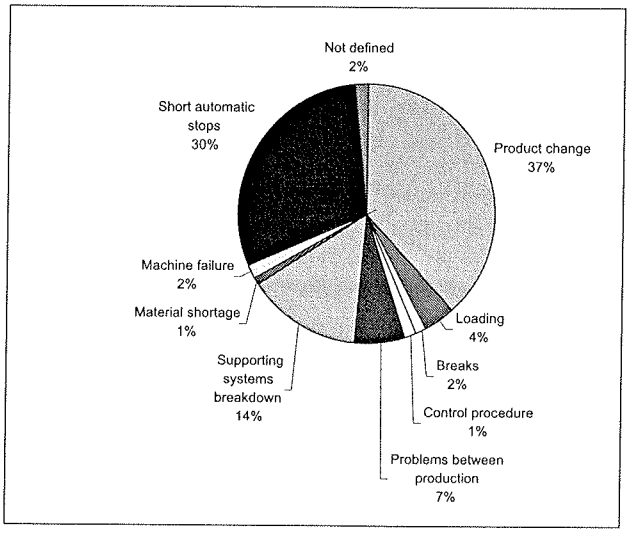

Fig. 6: Downtime categories relating to OEE from Figure 4

There are many ways to raise the OEE on this packaging line. Additional training of operators has already been implemented to minimize the downtime during the product change on the production line. Furthermore, organizational changes or technical improvements could be introduced. However, some of these improvements may raise additional investment costs.

4. Discussion

As described above, the concepts of overall equipment effectiveness for improving manufacturing performance are under constant development. By evolution of new produc-

tion management strategies, along with the "bottom-up" OEE approach expansion, the OEE principles are becoming more and more accepted in the industry. Not only in semiconductor or electronic equipment industry, but in many other branches like pharmaceutical or food industry. It can be proved by several successful implementations that continuous monitoring of the OEE metrics; in relation with clear target values can have a strong impact on productivity. In spite of this fact, more than 60% OEE implementation failed or did not bring expected results to the production company /9/. As the OEE implementation is a complex engineering task, several reasons for implementation failures can be outlined and discussed.

It is often a case, that management business strategy does not drive OEE implementation. If managers are not involved in OEE project, they are not familiar with the OEE results interpretation and do not accept it as a support for systematic analysis of equipment utilisation, efficiency and quality.

Further on, pre-implementation preparation activities (system analysis and downtime modelling) are often poorly planned. First, understanding OEE concept and customised it suitable for the industry sector is important precondition for success. The second thing to be aware of is that incomplete knowledge about production process and equipment under OEE study leads to unreliable downtime models and therefore, do not correspond to the real process behaviour.

Several early OEE implementations were not successful because of using traditional approach to OEE based on manual data entry of downtime events by operators. The main reason can be found in incomplete and untrustworthy input data. Consequently, the OEE results can be misunderstood or does not give complete information about production. Another problem of this approach is flexibility. In every production environment, the changes of technology and equipment are frequent. If implemented OEE solution is not flexible enough to incorporate these changes on a fast and easy way, the upgrading can be very complicated, time consuming and also quite expensive.

And at the end, it is very important to finish OEE implementation in planed time period and budget. Often, the OEE implementation took much longer than expected and users were not well-prepared to accept and operate with the OEE solution. Such projects are often not successful.

5. Conclusions

The strength of the OEE approach is systematic analysis of equipment utilisation, efficiency and quality. Continuous real-time monitoring of the OEE metrics in relation with clear target values can have a strong impact on productivity and makes it possible to establish a relationship between performance measures and business objectives. In particular, it enables the reduction of downtime and rate losses by increasing equipment utilization. The main benefits are in optimizing equipment utilization, better working transparency, increasing quality by reducing scrap and reworks. These benefits have important impact to overall production costs optimization, especially in the maintenance segment.

6. References

/1/ Ahmad, M.M. and N. Dhar. Establishing and improving manufacturing performance measures. Robotics and Computer Integrated manufacturing, 2002, vol. 18, p. 171-176.

/2/ Chan F.T.S. et. al. Implementation of total productive maintenance: A case study. International Journal of Production Economics, 2005, vol. 95, p. 71-94.

/3/ Dal; B. et. al. Overall equipment effectivness as a measure of operational improvement, a practical analysis. International Journal of Operations and Production Management,2000.

/4/ Hansen, C.R. Overall equipment effectivness, Industrial Press, 2001.

/5/ Högfeldt; D. Plant Efficiency: A value stream mapping and overall equipment effectivness study, Master of science programme, Lulei University of Technology, 2005.

/6/ Huang S., Dismukes J, Su S., Razzak M.,Bodhale R., Robinson E.: Manufactjuring productivity improvement using effectiveness metrics and simulation analysis, International Journal fo Production Research, Vol. 41, No.3., 513-527, 2003

/7/ Leachman R.C. Closed-loop measurement of Equipment Efficiency and Equipment Capacity, University of California at Berkeley, 2002.

/8/ Lungberg, O. Measurement of overall equipment effectivness as a basic for TPM activities. International Journal of Operations and Production Management 18 (5), p.p. 495-507, 1998.

/9/ MESA International, Metrics that Matter: Uncovering KPIs that Justify Operational Improvements, White paper, October 2006.

/10/ SEMATECH and JEITA, The Equipment Engineering Capability (EEC) Guidebook, Version 2.5., July 2002, available at http://ismi.sematech.org/emanufacturing/eec.htm.

/11/ SEMI E10-0304E - Specification for Definition and Measurement of Equipment Reliability, Availability, and Maintainability (RAM), available at http://www.semi.org.

/12/ Sokolić, S. and R. Ferko, Obvladovanje učinkovitosti proizvodnega procesa v Droga d.d., Chapter in a book: A. Kovačič and V.Bosilj Vukšić, Management poslovnih procesov, GV Založba, 2005.

/13/ Vollmann et al.. Manufacturing Planning and Control for Supply Chain Management (Fifth Edition). McGraw-Hill International Edition, 2005.

/14/ Wireman, T. Total Productive maintenance, Industrial Press, 2004.

Mag. Robert Ferko, Droga Kolinska d.d., Kolinska ulica 1, 1544 Ljubljana, Slovenija
Tel.: 01 47 21 500, Faks: 01 47 21 553, E-mail: robert.ferko@drogakolinska.si,

Dr. Alenka Žnidaršič, univ. dipl.inž.rač.,Metronik d.o.o., Stegne 9a, 1117 Ljubljana
Tel: 01 514 08 80, Fax: 01 514 09 07, E-mail: alenka.znidarsic@metronik.si

Prispelo (Arrived): 11.12.2006 *Sprejeto (Accepted):* 15.06.2007

UDK621.3:(53+54+621+66), ISSN0352-9045 Informacije MIDEM 37(2007)2, Ljubljana

Odsek za računalniške sisteme Instituta "Jožef Stefan" in raziskave na problematiki preizkušanja elektronskih vezij in sistemov

Franc Novak

Z naraščajočo kompleksnostjo integriranih vezij in sistemov postaja problem njihovega preizkušanja vedno težji in tudi vedno bolj aktualen. Sodobni sistemi-v-čipu in prihajajoča omrežja-v-čipu predstavljajo nove načrtovalske izzive, po drugi strani pa odpirajo nove probleme njihovega preizkušanja. Obvladanje razpoložljivih rešitev ter poznavanje standardov in bodočih trendov je ključnega pomena za uspešno proizvodnjo sodobnih elektronskih proizvodov visoke tehnologije.

V Odseku za računalniške sisteme Instituta "Jožef Stefan" se že vrsto let ukvarjamo s problematiko preizkušanja elektronskih vezij in sistemov. Spremljali smo nastanek standarda IEEE 1149.1, ki je uvedel pojem preizkusne robne linije (angl. boundary-scan) in se je v praksi izredno uveljavil. Sodelovali smo v delovnih skupinah za pripravo standarda IEEE 1149.4 (Mixed-Signal Test Bus) ter IEEE 1500 (Standard for Embedded Core Test).

Za lastne potrebe smo razvili preprost laboratorijski preizkusni sistem za IEEE 1149.x združljiva vezja in o njem med drugim tudi poročali v Informacijah MIDEM v letu 2003. V okviru tega sistema je bil realiziran tudi splošen prevajalnik za jezik SVF (ang. Serial Vector Format), ki sodi med standardne formate opisa preizkusnih postopkov na osnovi preizkusne robne linije.

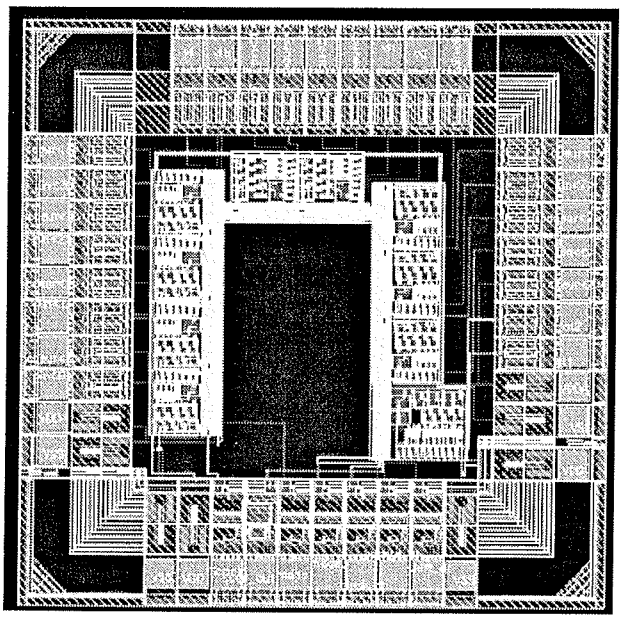

Slika 1: Eno prvih integriranih vezij po standardu IEEE 1149.4

V sodelovanju z LIRMM, Francija, smo razvili eno prvih integriranih vezij z vgrajeno preizkusno infrastrukturo skladno s standardom IEEE 1149.4. Vezje služi za razvoj preizkusnih metod in izvedbo različnih eksperimentalnih izvedbenih študij po standardu IEEE 1149.4. Predlagali smo tudi nekatere izboljšave standarda in jih v praksi realizirali v okviru omenjenega integriranega vezja.

Sodobni sistemi-v-čipu so osnovani na načrtovalskih pristopih, ki omogočajo integracijo velikih že uporabljenih in v praksi preizkušenih logičnih blokov (jeder). Ta pristop pa hkrati prinaša tudi nove probleme pri preizkušanju načrtovanega produkta, saj razvijalec običajno ne pozna do podrobnosti zgradbe uporabljenih jeder. Problemi nastanejo tudi pri prenosljivosti preizkusnih postopkov med dobavitelji jeder, načrtovalci sistemov-v-čipu in končnimi uporabniki. Standard IEEE 1500 do določene mere rešuje navedene probleme, vendar je v trenutni obliki namenjen le digitalnim jedrom. Razširitev funkcionalnosti preizkusne ovojnice, kot jo definira IEEE 1500, na mešana analogno/digitalna jedra je aktualna raziskovalna tema, ki se ji posvečamo tudi mi.

V okviru evropskega IST projekta 5. okvirnega programa EuNICEtest (European Network for Initial and Continuing Education in VLSI/SOC Testing using remote ATE facilities) smo zgradili okolje, ki omogoča lokalni razvoj preizkusnih postopkov ter njihovo daljinsko izvajanje na napravi za preizkušanje VLSI vezij Agilent 83000-F330t v centru CRTC v Montpellieru. Okolje je namenjeno šolanju novih inženirjev na problematiki preizkušanja elektronskih vezij.

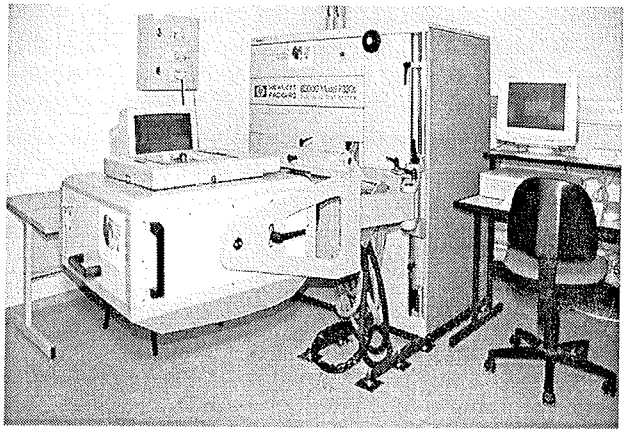

Slika 2: Preizkusni sistem Agilent 83000-F330t

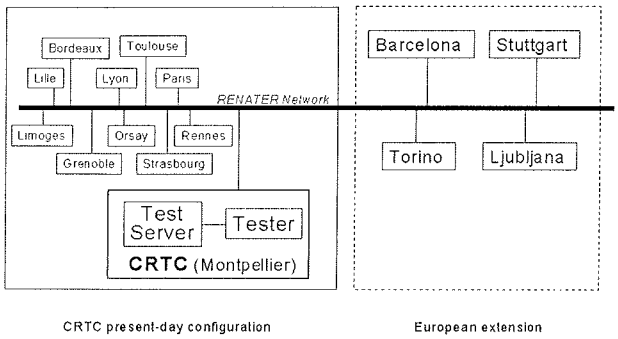

Slika 3: EuNICEtest - povezave s centrom CRTC Montpellier

Sodelujemo v ETTTC (European Test Technology Technical Council), ki na delovnih sestankih v okviru pomembnejših evropskih in svetovnih konferenc analizira aktualne raziskovalne trende in daje iniciativo za skupno raziskovalno delo na izbranih tematskih področjih.

V okviru 43. mednarodne konference MIDEM 2007 smo organizirali mednarodno delavnico Workshop on Electronic Testing, ki so se je udeležili ugledni tuji in domači strokovnjaki. Delavnica je dobro uspela, kar daje spodbudo za nadaljnje delo tudi pri povezovanju strokovne javnosti in organizaciji strokovnih srečanj.

Informacije MIDEM
Strokovna revija za mikroelektroniko, elektronske sestavine dele in materiale

NAVODILA AVTORJEM

Informacije MIDEM je znanstveno-strokovno-društvena publikacija Strokovnega društva za mikroelektroniko, elektronske sestavne dele in materiale - MIDEM. Revija objavlja prispevke s področja mikroelektronike, elektronskih sestavnih delov in materialov. Ob oddaji člankov morajo avtorji predlagati uredništvu razvrstitev dela v skladu s tipologijo za vodenje bibliografij v okviru sistema COBISS.
Znanstveni in strokovni prispevki bodo recenzirani.

Znanstveno-strokovni prispevki morajo biti pripravljeni na naslednji način:

1. Naslov dela, imena in priimki avtorjev brez titul, imena institucij in firm
2. Ključne besede in povzetek (največ 250 besed).
3. Naslov dela v angleščini.
4. Ključne besede v angleščini (Key words) in podaljšani povzetek (Extended Abstract) v angleščini, če je članek napisan v slovenščini
5. Uvod, glavni del, zaključek, zahvale, dodatki in literatura v skladu z IMRAD shemo (Introduction, Methods, Results And Discsussion).
6. Polna imena in priimki avtorjev s titulami, naslovi institucij in firm, v katerih so zaposleni ter tel./Fax/Email podatki.
7. Prispevki naj bodo oblikovani enostransko na A4 straneh v enem stolpcu z dvojnim razmikom, velikost črk namanj 12pt. Priporočena dolžina članka je 12-15 strani brez slik.

Ostali prispevki, kot so poljudni cčlanki, aplikacijski članki, novice iz stroke, vesti iz delovnih organizacij, inštitutov in fakultet, obvestila o akcijah društva MIDEM in njegovih članov ter drugi prispevki so dobrodošli.

Ostala splošna navodila

1. V članku je potrebno uporabljati SI sistem enot oz. v oklepaju navesti alternativne enote.
2. Risbe je potrebno izdelati ali iztiskati na belem papirju. Širina risb naj bo do 7.5 oz.15 cm. Vsaka risba, tabela ali fotografija naj ima številko in podnapis, ki označuje njeno vsebino. Risb, tabel in fotografij ni potrebno lepiti med tekst, ampak jih je potrebno ločeno priložiti članku. V tekstu je treba označiti mesto, kjer jih je potrebno vstaviti.
3. Delo je lahko napisano in bo objavljeno v slovenščini ali v angleščini.
4. Uredniški odbor ne bo sprejel strokovnih prispevkov, ki ne bodo poslani v dveh izvodih skupaj z elektronsko verzijo prispevka na disketi ali zgoščenki v formatih ASCII ali Word for Windows. Grafične datoteke naj bodo priložene ločeno in so lahko v formatu TIFF, EPS, JPEG, VMF ali GIF.
5. Avtorji so v celoti odgovorni za vsebino objavljenega sestavka.

Rokopisov ne vračamo. Rokopise pošljite na spodnji naslov.

Uredništvo Informacije MIDEM
MIDEM pri MIKROIKS
Stegne 11, 1521 Ljubljana, Slovenia
Email: Iztok.Sorli@guest.arnes.si
tel. (01) 5133 768, fax. (01) 5133 771

Informacije MIDEM
Journal of Microelectronics, Electronic Components and Materials

INSTRUCTIONS FOR AUTHORS

Informacije MIDEM is a scientific-professional-social publication of Professional Society for Microelectronics, Electronic Components and Materials - MIDEM. In the Journal, scientific and professional contributions are published covering the field of microelectronics, electronic components and materials.
Authors should suggest to the Editorial board the classification of their contribution such as : original scientific paper, review scientific paper, professional paper...
Scientific and professional papers are subject to review.

Each scientific contribution should include the following:

1. Title of the paper, authors' names, name of the institution/company.
2. Key Words (5-10 words) and Abstract (200-250 words), stating how the work advances state of the art in the field.
3. Introduction, main text, conclusion, acknowledgements, appendix and references following the IMRAD scheme (Introduction, Methods, Results And Discsussion).
4. Full authors' names, titles and complete company/institution address, including Tel./Fax/Email.
5. Manuscripts should be typed double-spaced on one side of A4 page format in font size 12pt. Recommended length of manuscript (figures not included) is 12-15 pages
6. Slovene authors writing in English language must submit title, key words and abstract also in Slovene language.
7. Authors writing in Slovene language must submit title, key words and extended abstract (500-700 words) also in English language.

Other types of contributions such as popular papers, application papers, scientific news, news from companies, institutes and universities, reports on actions of MIDEM Society and its members as well as other relevant contributions, of appropriate length , are also welcome.

General informations

1. Authors should use SI units and provide alternative units in parentheses wherever necessary.
2. Illustrations should be in black on-white paper. Their width should be up to 7.5 or 15 cm. Each illustration, table or photograph should be numbered and with legend added. Illustrations, tables and photographs must not be included in the text but added separately. However, their position in the text should be clearly marked.
3. Contributions may be written and will be published in Slovene or English language.
4. Authors must send two hard copies of the complete contributon, together with all files on diskette or CD, in ASCII or Word for Windows format. Graphic files must be added separately and may be in TIFF, EPS, JPEG, VMF or GIF format.
5. Authors are fully responsible for the content of the paper.

Contributions are to be sent to the address below.

Uredništvo Informacije MIDEM
MIDEM pri MIKROIKS
Stegne 11, 1521 Ljubljana, Slovenia
Email: Iztok.Sorli@guest.arnes.si
tel.+386 1 5133 768, fax.+386 1 5133 771